Title

Identification, Development, and Evaluation of Brain-Penetrant Small-Molecule Inhibitors of Epidermal Growth Factor Receptor in Glioblastoma

Author

Tsang, Jonathan

Publication Date

2021

Peer reviewed|Thesis/dissertation

UNIVERSITY OF CALIFORNIA

Los Angeles

Identification, Development, and Evaluation of Brain-Penetrant Small-Molecule Inhibitors of Epidermal Growth Factor Receptor in Glioblastoma

A dissertation submitted in partial satisfaction of the

requirements for the degree Doctor of Philosophy

in Molecular and Medical Pharmacology

by

Jonathan Edward Tsang

2021

ABSTRACT OF THE DISSERTATION

Identification, Development, and Evaluation of Brain-Penetrant Small-Molecule Inhibitors of Epidermal Growth Factor Receptor in Glioblastoma

by

Jonathan Edward Tsang

Doctor of Philosophy in Molecular and Medical Pharmacology

University of California, Los Angeles, 2021

Professor David A. Nathanson, Chair

The epidermal growth factor receptor (EGFR) is genetically altered in nearly 60% of glioblastoma (GBM) tumors; however, tyrosine kinase inhibitors (TKIs) against EGFR have failed to show efficacy for patients with these lethal brain tumors. This failure has been attributed to the inability of clinically tested EGFR TKIs (e.g. erlotinib, gefitinib, lapatinib, afatinib) to effectively penetrate the blood-brain barrier (BBB) and achieve adequate pharmacological levels to inhibit the oncogenic forms of EGFR that drive GBM to induce a tumor response. Hence, there is a highly unmet medical need for effective therapeutics for GBM. In these studies, we detail the identification, development, and evaluation of brain-penetrant, small molecule inhibitors of EGFR to a clinical compound. This dissertation begins with a structure-activity relationship (SAR) to develop JCN037 as an early pre-clinical lead molecule. JCN037 was developed from a 4-anilinoquinazoline scaffold by ring fusion of the 6,7-dialkoxy groups to

reduce the number of rotatable bonds and polar surface area, and by introduction of an ortho-fluorine and meta-bromine on the aniline ring for improved potency and BBB penetration. Relative to the conventional EGFR TKIs erlotinib and lapatinib, JCN037 displayed potent activity against EGFR amplified/mutant patient-derived cell cultures, significant BBB penetration (2:1 brain-to-plasma ratio), and superior efficacy in an EGFR-driven orthotopic glioblastoma xenograft model. However, JCN037 was limited by a poor *in vivo* half life and a quick metabolism. Further SAR analysis lead to the development of JCN068, an EGFR TKI that potently inhibits oncogenic forms of EGFR with improved BBB penetration (>3:1 brain-to-plasma ratio). Compared to clinically tested EGFR TKIs, JCN068 demonstrates improved potency activity against EGFR amplified/mutant patient-derived cell cultures, significantly higher BBB, ideal clinical candidate *in vivo* pharmacology, and superior efficacy in multiple EGFR-driven orthotopic glioblastoma xenograft models. Additionally, rapid changes in tumor ^{18}F-fluorodeoxyglucose (^{18}F-FDG) uptake using non-invasive positron emission tomography (PET) was utilized as an effective predictive biomarker of response to JCN068 therapy *in vivo*. JCN068 is currently advancing in IND-enabling studies as a new potential therapeutic for EGFR-driven GBM.

This dissertation of Jonathan Edward Tsang is approved.

Thomas G. Graeber

Steven J. Bensinger

Peter M. Clark

Kym F. Faull

David A. Nathanson, Committee Chair

University of California, Los Angeles

2021

TABLE OF CONTENTS

ABSTRACT OF THE DISSERTATION ii

COMMITTEE PAGE.……..……iv

TABLE OF CONTENTS v

ACKNOWLEDGEMENTS ix

VITA..... xi

CHAPTER 1: Development of JCN037, a Potent Brain-Penetrant EGFR Tyrosine Kinase Inhibitor Against Malignant Brain Tumors……..…….1

INTRODUCTION.....2

RESULTS.....3

DISCUSSION 14

FIGURES AND TABLES 16

Chapter 1 – Table 1.....16

Chapter 1 – Table 2.....17

Chapter 1 – Table 3.....18

Chapter 1 – Table 4.....19

Chapter 1 – Table 5.....20

Chapter 1 – Figure 1 21

Chapter 1 – Figure 2 22

Chapter 1 – Figure 3 24

Chapter 1 – Scheme 1 25

SUPPLEMENTARY FIGURES AND TABLES 26

Chapter 1 – Figure S1 27
Chapter 1 – Table S1.....29
Chapter 1 – Figure S2 30
Chapter 1 – Table S2.....31
Chapter 1 – Figure S3 31
Chapter 1 – Table S3.....32
Chapter 1 – Figure S4 33
Chapter 1 - Table S4 33
Chapter 1 – Figure S5 34
Chapter 1 – Figure S6 37
Chapter 1 – Figure S7 38
Chapter 1 – Figure S8 39
Chapter 1 – Figure S9 39
Chapter 1 – Figure S10 40
Chapter 1 – Table S5.....40
Chapter 1 – Figure S11 41
Chapter 1 – Figure S12 42
Chapter 1 – Figure S13 44
Chapter 1 – Table S6.....45
Chapter 1 – Figure S14 46
Chapter 1 – Figure S15 47
Chapter 1 – Table S7.....48
Chapter 1 – Figure S16 49

Chapter 1 – Figure S17 50
SYNTHESIS SCHEMES 51
Chapter 1 – Scheme S1 51
Chapter 1 – Scheme S2 52
Chapter 1 – Scheme S3 53
EXPERIMENTAL METHODS 54
REFERENCES 101

CHAPTER 2: Development and Evaluation of JCN068, a Novel Highly Brain-Penetrant EGFR Tyrosine Kinase Inhibitor for Glioblastoma 106
INTRODUCTION 107
RESULTS 110
DISCUSSION 116
FIGURES AND TABLES 118
Chapter 2 – Figure 1. 118
Chapter 2 – Figure 2 120
Chapter 2 – Figure 3. 121
Chapter 2 – Figure 4. 122
Chapter 2 – Table 1. 123
Chapter 2 – Figure 5 124
Chapter 2 – Figure 6 126
Chapter 2 – Figure 7 127
Chapter 2- Figure 8 129
Chapter 2 – Figure 9 131

Chapter 2 – Figure 10 132
Chapter 2 – Figure 11 134
SUPPLEMENTARY FIGURES AND TABLES 135
Chapter 2 – Table S1.....135
Chapter 2 – Figure S1 137
Chapter 2 – Figure S2 138
EXPERIMENTAL METHODS.....139
REFERENCES.....146

ACKNOWLEDGEMENTS

First, I would like thank Professor David Nathanson for his guidance, support, and inspiration throughout my time as a graduate student in his laboratory. Dr. Nathanson has been an excellent mentor broadening my knowledge and guiding me to be become a skilled and independent researcher. I have grown tremendously both scientifically and personally throughout my graduate career and attribute a tremendous amount of this growth to Dr. Nathanson's dedication as a mentor and his lead by example. Furthermore, I would like to thank the members of my committee, Professors Thomas Graeber, Steven Bensinger, Peter Clark, and Kym Faull for their helpful scientific discussion and constant support for my project.

I would also like to express my gratitude to numerous current and past members of the Nathanson Laboratory for their support and assistance over the years. From teaching me how to perform various techniques to their intellectual contributions to their emotional support, my fellow lab members have contributed greatly to my development as a scientist. Lorenz Urner and Gyudong Kim synthesized compounds and taught me about medicinal chemistry. Christopher Tse, Jennifer Salinas, and Lynn Baufeld aided in intracranial injections through the years. Wilson Mai, Danielle Morrow, Elizabeth Fernandez, Nicholas Bayley, Henan Zhu, Jenna Minami, Quincy Okobi, and Robert Chong provided thoughtful scientific feedback. Kingsley Chow, Sam Clark, Andrew Tum, and Eva Zhao helped with *in vitro* and *in vivo* experiments.

Finally, I would like to thank many people who have supported me in my personal life. First and foremost, to my fiancé, Tran Hue Do, who has been there for me participating scientific discussion and caring for my well-being. More importantly, she not only put up with all the times I had to go to lab in the middle of the night to check on mice but also drove and waited for me. I

would also thank my family, Thomas, Pearl, and Kimberly Tsang for their support and encouragement. I would also like to thank all the friends I have made and grown closer to at UCLA for making my time outside of lab enjoyable.

Chapter 1 is a version of JE Tsang, LM Urner, G Kim, K Chow, L Baufeld, K Faull, TF Cloughesy, PM Clark, ME Jung, and DA Nathanson. Development of a Potent Brain-Penetrant EGFR Tyrosine Kinase Inhibitor against Malignant Brain Tumors. ACS Medicinal Chemistry Letters. (2020) 11.10 (2020): 1799-1809. doi: 10.1021/acsmedchemlett.9b00599.

My research was supported by the Uncle Kory Foundation.

VITA

EDUCATION

2016-2021 Ph.D. Candidate, Molecular and Medical Pharmacology
University of California, Los Angeles
Department of Molecular and Medical Pharmacology
Los Angeles, CA

2010-2014 B. S., Chemical Biology with Honors
University of California, Berkeley
Department of Chemistry
Berkeley, CA

EMPLOYMENT

2014-2015 Scientist 1
Roche Molecular Systems. Pleasanton, CA

2014 Summer Research Intern
Roche Molecular Systems. Pleasanton, CA

2013 Summer Research Intern
Roche Molecular Systems. Pleasanton, CA

2011 Summer Research Intern
University of North Texas Health Science Center. Fort Worth, TX

AWARDS AND HONORS

2019 Molecular and Medical Pharmacology Retreat Presentation Award

2019 UCLA Bioscience Innovation Day Pearl Cohen Award

2018 Molecular and Medical Pharmacology Seminar Award

2017 Molecular and Medical Pharmacology Retreat Poster Award

2016 Addressing Childhood Obesity Proposal Challenge Winner
Los Angeles County Medical Association

2015 Shamrock Scholarship

2014 Roche Molecular Systems Intern Poster Symposium

2014 College of Chemistry Senior Undergraduate Research Award

2010-2014 Brookhaven Science Associates Scholarship

2012 Chevron Summer Research Award

PUBLICATIONS

JE Tsang, LM Urner, G Kim, K Chow, L Baufeld, K Faull, TF Cloughesy, PM Clark, ME Jung, and DA Nathanson. “Development of a Potent Brain-Penetrant EGFR Tyrosine Kinase Inhibitor against Malignant Brain Tumors.” *ACS Medicinal Chemistry Letters* 11.10 (2020): 1799-1809.

M Saki,K Bhat, F Cheng, L He, L Zhang, A Ioannidis, D Nathanson, J Tsang, P Leia Nghiemphu, TF Cloughesy, LM Liau, HI Kornblum, F Pajonk. “Dopamine receptor antagonists, radiation and cholesterol biosynthesis in mouse models of glioblastoma.” Journal of the National Cancer Institute (2021) (In press).

PY Wen, M Weller, EQ Lee, BA Alexander, JS Barnholtz-Sloan, FP Barthel, TT Batchelor, RS Bindra, SM Chang, EA Chiocca, TF Cloughesy, JF DeGroot, E Galanis, MR Gilbert, ME Hegi, C Horbinski, RY Huang, AB Lassman, EL Rhun, M Lim, MP Mehta, IK Mellinghoff, G Minniti, D Nathanson, M Platten, M Preusser, P Roth, M Sanson, D Schiff, SC Short, MJB Taphoorn, JC Tonn, J Tsang, RGW Verhaak, A von Deimling, W Wick, G Zadeh, DA Reardon, KD Aldape, MJ van den Bent. “Glioblastoma in Adults: A Society for Neuro-Oncology (SNO) and European Society of Neuro-Oncology (EANO) Consensus Review on Current Management and Future Directions.” *Neuro-oncology* 22.8 (2020): 1073-1113.

Z Li, H Cheng, S Shao, X Lu, L Mo, J Tsang, P Zeng, Z Guo, S Wang, DA Nathanson, JR Heath, W Wei, M Xue. "Surface Immobilization of Redox-Labile Fluorescent Probes: Enabling Single-Cell Co-Profiling of Aerobic Glycolysis and Oncogenic Protein Signaling Activities." Angewandte Chemie International Edition 57.36 (2018): 11554-11558.

WX Mai, L Gosa, VW Daniels, L Ta, JE Tsang, B Higgins, WB Gilmore, NA Bayley, MD Harati, JT Lee, WH Yong, HI Kornblum, SJ Bensinger, PS Mischel, PN Rao, PM Clark, TF Cloughesy, A Letai, DA Nathanson. "Cytoplasmic p53 couples oncogene-driven glucose metabolism to apoptosis and is a therapeutic target in glioblastoma." Nature medicine 23.11 (2017): 1342.

CW Meadows, JE Tsang, JP Klinman. “Picosecond-Resolved Fluorescence Studies of Substrate and Cofactor-Binding Domain Mutants in a Thermophilic Alcohol Dehydrogenase Uncovers an Extended Network of Communication.” J Am Chem Soc. (2014). 136(42): 14821-33.

CHAPTER 1: Development of JCN037, a Potent Brain-Penetrant EGFR Tyrosine Kinase Inhibitor Against Malignant Brain Tumors

INTRODUCTION

Malignant gliomas, including the universally lethal glioblastoma (GBM), are the most common and the deadliest primary brain tumors. The epidermal growth factor receptor (EGFR) is mutated and/or amplified in ~60% of GBM tumors.[1] Of these tumors with genetically-altered EGFR, approximately 50% consist of amplified wild-type EGFR (wtEGFR) with no mutations, while the remaining tumors in this cohort have an amplification with an activating extracellular domain mutation. The most prominent activating mutation is a deletion of exons 2–7 in EGFR [EGFRvIII].[1] Both amplified wtEGFR and EGFRvIII play important roles in tumor growth, proliferation, and survival.[2] Moreover, in EGFRvIII expressing tumors, wtEGFR is diffusely expressed and cooperates with EGFRvIII to promote tumorigenesis.[2,3] Given the importance of both mutant and wtEGFR as drivers of malignant glioma, numerous clinical trials using 1st generation EGFR tyrosine kinase inhibitors (TKIs) (i.e., erlotinib, lapatinib, and gefitinib) have been evaluated in GBM patients. However, all studies using these EGFR TKIs failed to improve the outcomes of patients with GBM.[4,5]

Significant evidence suggests that all the 1st generation EGFR TKIs do not cross the blood-brain barrier (BBB) in concentrations sufficient to achieve therapeutic consequences in GBM tumors.[4-6] Although next-generation EGFR inhibitors, such as afatinib, dacomitinib, and neratinib, are still under clinical investigation for GBM, early data suggest minimal clinical activity for those EGFR TKIs in which patient outcomes are available.[7,8] The limited efficacy observed in GBM patients with these next-generation EGFR inhibitors may also be due to their inadequate brain exposure.[9,10] While the EGFR TKI osimertinib – developed for EGFR-mutated lung cancer – has reported high brain penetration,[9] it has yet to be thoroughly evaluated either preclinically or clinically for GBM. Moreover, osimertinib does not effectively inhibit wtEGFR,[11] which is

presumably required to effectively target EGFR-driven GBMs.[2] Thus, obtaining pharmacological levels of EGFR TKIs within GBM tumors, while also having potent activity against both wtEGFR and EGFRvIII, remains a major obstacle for their effective treatment.

A potential contributor to the low brain exposures of currently used clinical EGFR TKIs (and for the FDA-approved kinase inhibitors lacking brain-penetration) is that they do not conform to the physicochemical properties that are associated with BBB penetration (Table 1).[12] Specifically, for clinically available EGFR TKIs, the molecular weight (MW), the number of hydrogen bond donors (HBD) and acceptors (HBA), the polar surface area (TPSA), and the number of rotatable bonds (NRB) fall outside the desired ranges recommended by Ghose et al.[13] and Wager et al.[14] (Table 1). Finally, these physicochemical properties have also been shown to influence the ability of the P-glycoprotein (P-gp) – a prominent drug efflux transporter found in brain capillary endothelial cells – to recognize drugs that include currently clinically used EGFR TKIs, and thus limit drug exposure in the brain.[15]

RESULTS

To address this problem of low brain penetration of EGFR TKIs, we modified the 4-anilinoquinazoline scaffold of 1st generation EGFR TKIs with the goal of obtaining an EGFR TKI with the desired physicochemical properties for BBB penetration, while having activity against both wtEGFR and EGFRvIII. We report the synthesis and characterization of **5** (JCN037), a non-covalent EGFR TKI that demonstrated both nanomolar potency against both mutant EGFRvIII and wtEGFR in cellular assays and greater than 2:1 brain to plasma levels. Moreover, **5** was effective at inhibiting the growth of EGFR-driven primary GBM cells, both in cell culture and in

orthotopic xenografts. Importantly, the outcomes of *in vivo* treatment of xenografted malignant glioma with **5** were superior to that of both erlotinib and lapatinib.

Like other type I EGFR TKIs (e.g., gefitinib), erlotinib can potently target both the active confirmation of wtEGFR and has the capacity to bind, although with less affinity, to mutant EGFRvIII.[6] Conversely, type II EGFR TKIs (e.g., lapatinib, neratinib) – which favor the inactive form of EGFR - can have high affinity for EGFRvIII, yet are extremely ineffective at targeting activated wtEGFR.[6] Our goal was to have a compound that could potently inhibit both wtEGFR and EGFRvIII; for this reason we selected erlotinib as our starting point to initiate our structure actvity relationship (SAR) studies.

Erlotinib penetrates the brain at a very low level of 7%.[16] Physicochemical features of erlotinib that could make it a poor brain-penetrating drug include a large NRB (10), several HBA (7), and a high TPSA (75 Å) and many of these liabilities derive from the flexible alkyl ether tails. We hypothesized that improving these physicochemical properties linked to brain penetration might be achievable by modifying positions that may not be essential for binding to the EGFR kinase domain.

From the extensive SAR work performed on the 4-anilinoquinazoline pharmacophore, as well as from the wealth of available structural information on the EGFR kinase domain, the essential binding interactions of this TKI scaffold are well known.[11,17,18] An overview of the type I binding mode of erlotinib and, for comparison, the non-hydrolyzable ATP-analogue AMP-PNP are depicted in Figure S1.

Based on these considerations, we hypothesized that closing the flexible alkoxy chains at C6 and C7 to form a 1,4-dioxane ring fused onto the quinazoline scaffold – a modification that has been investigated previously as a means to increase the solubility of these compounds[19] – may

increase BBB penetrance without affecting binding of the molecule to EGFR. This modification yielded **1**, which contains a reduced NRB (10 to 2), HBA (7 to 5), and TPSA (75 Å to 56 Å) relative to erlotinib (Table 2). Importantly, the more optimal physicochemical properties of **1** were associated with, perhaps unpredictably, a nearly ten times increase in BBB penetration relative to erlotinib. Following a single oral dose of **1** (10 mg/kg) in healthy CD-1 mice, the brain/plasma ratio was 0.71; in contrast, and in line with previous reports,[16] the brain/plasma ratio of erlotinib was 0.085 (Table 2).

To determine how the fusion of the dioxane ring impacts activity against wild-type and EGFRvIII, **1** was tested in enzymatic and cellular biochemical assays (Table 2). Despite our prediction that this modification would not affect activity, **1** was significantly less potent than erlotinib against both wild-type and mutant EGFRvIII. The reduced potency of **1** relative to erlotinib was also reflected in a lower activity against two EGFRvIII mutant patient derived GBM cells, HK301 and GBM39; the half maximal growth inhibitory concentration (GI_{50}) for **1** was 10-fold worse than erlotinib against these GBM cell lines. Thus, the surprisingly remarkable brain penetration achieved by fusing the alkyl ether tails of erlotinib came at an unexpected loss of inhibitor potency.

To improve upon potency, we considered modifications of the aniline ring through the introduction of a second substituent. As the binding pocket of the aniline ring—the apolar hole—only permits small, lipophilic substituents, we considered the strategic placement of a halide next to the alkyne. For several known EGFR TKIs, halogenated aniline rings are common with, in particular, fluorine or chlorine substituents. Moreover, a 2'-fluorine with a -3'-substituent on the aniline ring has been shown to increase activity against EGFR.[20,21] As such, we hypothesized that the addition of a 2'-fluorine substituent to **1** would improve its affinity for EGFR. Indeed, cell-free

enzymatic activity assays and cellular wtEGFR and EGFRvIII phosphorylation studies revealed an increased potency from **1** against EGFR kinase activity for **2** (Table 2). Additional *in vitro* profiling of cellular growth and proliferation showed a marked improvement in the GI_{50} of **2** on HK301 and GBM39 patient-derived GBM lines, suggesting the *ortho*-fluorine improved the protein-ligand interaction with EGFR.

Fluorine substituents are known to affect biological activity and absorption, distribution, metabolism, and excretion (ADME) properties of a drug by modulating lipophilicity while preserving hydrogen bonds and total polar surface area.[22] Specifically, an *ortho*-fluorine on an aniline ring has been observed in various reports to mitigate the strength of an adjacent HBD and can potentially improve brain penetration and membrane permeability by reducing the strength of hydrogen bond interactions.[21,22] To determine the influence of an *ortho*-fluorine on the aniline ring on brain penetration, we profiled **2** *in vivo* in healthy CD-1 mice (Table 2). Although the exposure and maximum concentration of **2** was considerably improved relative to **1**, the increase in BBB permeability was modest, with a change in brain/plasma $AUC_{0–7h}$ from 0.65 (**1**) to 0.85 (**2**).

Closure of the alkoxy chains and adding a fluorine to the 2'-position on the aniline ring led to a compound that was more brain penetrant and potent than **1**, yet still less active than clinically available EGFR inhibitors (such as erlotinib). Constrained by the environment of the apolar hole as explained before, we focused our efforts on the SAR analysis of halogen as well as similar bioisosteric substituents on the aniline ring. In particular, we carried out a fluorine scan (**S1–S8** in Table S1) on the aniline ring to identify the optimal substitution pattern for EGFR inhibition (while retaining the 2'-fluorine).[23] We observed that the 2', 3'-difluoro substitution pattern (**S3**) was the most potent in cellular wtEGFR and EGFRvIII phosphorylation studies of these compounds and, consistent with these biochemical assays, was the most potent of the multi-fluoro substituted

compounds at inhibiting both HK301 and GBM39 patient-derived GBM lines. Collectively, these results suggest a 2', 3'-disubstitution pattern on the aniline ring is the most active of fluoro-substituted derivatives against both wtEGFR and EGFRvIII biochemically and in cellular proliferation assays. One potential rationale is the favorable dipolar and lipophilic character created on the aniline by this substitution pattern, which fits well with the possible lipophilic and electrostatic environment of the apolar hole (Figure S2).

Next, we proceeded to test additional isostere substituents to improve potency against EGFR (Table 3). We focused on substituents that were not expected to interfere with the properties that we had previously optimized to obtain significant brain penetrance, including NRB, TPSA, and HBA. To mimic the 3'-ethynyl substituent of **2**, a related isostere consisting of a 3'-cyano group was also synthesized (**3**). However, efficacy of TKI activity was reduced by the introduction of the 3'-cyano group, suggesting that the anisotropic electron-density distribution of the apolar ethynyl group with a partially positive charged region (hydrogen atom) is more favorable at this position than partially negatively charged region of the more polar cyano group (the lone electron pair on the nitrogen). Therefore, we decided to test all additional halide substituents at this 3'-position on the aniline ring, as they should provide a better isosteric replacement for the ethynyl group.[24]

Surprisingly, the affinity towards EGFR increased with the size of the 3'-halogen substituent on the aniline ring up to a maximum with a 3'-bromine (**S3, 4, 5, 6**) (cell-free IC_{50} of 18.9 nM, 3.91 nM, 2.49 nM, and 10.4 nM, respectively) (Table S2). This result may imply unspecific lipophilic interactions and a possible size limitation of the 3' position on the aniline ring.[22] In biochemical cellular phosphorylation and cell proliferation assays, the same trend in potency was also observed with the most potent among them being **5**. Together, exploration of 3'-

substituents on the aniline ring revealed a bias towards a 2'-fluorine and 3'-halide as the most potent inhibitors of EGFR, with the Cl or Br substitution in the 3'-position having the most activity.

To further test the importance of the 2'-fluorine, derivatives of **3–5** lacking the 2'-fluorine were evaluated (Table 3). Although **8** was similar in potency as **3** against EGFR, it was inferior to the 3'-halide substituted compounds (**S3**, **4**, **5**, **6)**. Moreover, compounds **9** and **10**,[25] had reduced efficacy against EGFR compared to their 2'-fluorinated counterparts. The significance of the 2'-fluorine in protein-ligand binding was further accentuated by the substitution with a polar 2'-hydroxy group for the fluorine (**11**), which greatly reduced EGFR affinity. These results suggest a limitation of size and polarity of the 2' substituent which is in line with previous studies.[17]

We next investigated trisubstituted anilines as they can be potent inhibitors of EGFR.[26] Retaining the 2'-fluorine and 3'-bromine on the aniline ring, we examined the effect of an additional halide in either the 4'- or 5'-position (**12–17**). In particular, the tri-substituted aniline ring of **15** resulted in a potent EGFR inhibitor in both biochemical and cell-based proliferation assays (Table 4). Since an *ortho*-fluorine was identified as important to improve potency, we also asked if a 6'- instead of a 2'-fluorine, or two *ortho*-fluorines would influence potency against EGFR (**18** and **19**). Although anti-proliferative effects against patient-derived GBM lines were on par with those of **5**, the ability to inhibit EGFR in cell-free and cell-based assays was reduced, suggesting potential off-target effects of **18** and **19**.

To further differentiate our lead EGFR inhibitors, we next examined their selectivity as well as BBB penetrance. First, to examine potential off-target activity, compounds were screened against endogenous cells of the brain, normal human astrocytes (NHA); which, in contrast to EGFR-altered GBM cells, lack a dependency on EGFR for growth (Figure S3). As predicted, compounds **15** and **18**, as well as **19** had a low NHA/GBM GI_{50} ratio supporting their potential for

off-target effects (Table S3). Conversely, **1**, **2**, **S3**, **4–6**, displayed high potency against primary GBM cells relative to NHAs (Table S3). Next, we sought to ascertain the brain penetrance of those compounds with a high NHA/GBM GI_{50} ratio. Pharmacokinetic analysis of brain/plasma ratios in healthy CD-1 mice revealed an improved brain penetrance with a 3'-halide over a 3'-alkyne substituent, with the most penetrant unexpectedly containing a bromine substitution (Table 5). Brain penetration of the most potent compounds, **4** and **5**, achieved brain/plasma ratios of 1.064 and 2.118 and $K_{p,uu}$ of 1.04 and 1.30, respectively (Figure S4).

Given the relatively high BBB penetration of our dioxane-containing EGFR TKIs, we explored the potential molecular rationale for this observation. Reducing the MW, HBD, HBA, TPSA, and NRB can increase brain penetration through circumventing recognition by the P-gp or breast cancer resistance protein (BCRP) drug efflux pumps on brain capillary endothelial cells.[15,27] We hypothesized that the fused dioxane ring of our EGFR TKIs may limit substrate identification by P-gp or BCRP. Evaluation of compounds **1**, **2**, **S3**, **4–6** by transwell culture with MDCK-MDR1 cells revealed that our compounds are highly permeable ($>10 \cdot 10^{-6}$ cm/s), with a low efflux ratio, indicating that these new EGFR TKIs are not strong substrates of P-gp or BCRP. (Table 5, Table S4). Together, these data suggest that replacement of the alkoxy tails by the fused dioxane ring reduces P-gp and BCRP substrate identification—potentially by the disruption of a recognized pattern of HBA. This reduced substrate affinity may contribute to the enhanced BBB penetration observed with our EGFR TKIs. Based on the high potency against both wtEGFR and EGFRvIII in cell-based biochemical assays, the strong anti-proliferative effects against multiple EGFR-driven patient-derived lines, the low activity against the NHA cell line, and the high brain penetrance, **5** was chosen as the lead candidate for additional *in vitro* and *in vivo* evaluations.

To determine the specificity of **5**, kinome profiling was performed at 1 μM across 485 wild-type and mutant kinases (Thermofisher). **5** strongly (>90%) inhibited EGFR and most EGFR kinase domain mutants with few off-target kinases (Figure S5). Only 14 kinases were inhibited by greater than 50%; of which, eight were EGFR and EGFR mutant kinases. Moreover, IC_{50} values of all wild-type kinases with greater than 50% inhibition at 1 μM of **5** revealed nearly 400x selectivity for EGFR (0.6 nM) relative to the next closest kinase (RIPK3: 226 nM) (Figure S5).

To further evaluate **5**, we biochemically profiled it against both erlotinib and lapatinib in two EGFR-altered patient-derived gliomaspheres: GBM39 (EGFRvIII mutant) and GS025 (amplified EGFR). In GBM39, all three TKIs potently inhibited EGFRvIII activation as well as the RAS-MAPK (via p-ERK) and PI3K-AKT-mTOR (via pS6) signaling pathways downstream of EGFR in a dose-dependent manner (Figure 1A). Modulation of these pathways with the various EGFR TKIs occurred to a similar degree, albeit lapatinib and **5** demonstrated slightly more signaling inhibition in the 100–333 nM concentrations relative to erlotinib. Consistent with these signaling results, we observed all three TKIs inhibited growth of EGFRvIII mutant GBM39 cells, with lapatinib and **5** showing more robust growth inhibition than erlotinib at 100–300 nM (Figure 1D). For GS025, we observed that erlotinib and **5** had nearly identical effects on wtEGFR signaling and, consequently, growth inhibition (Figure 1B and D). Conversely, we observed a notable loss in biochemical and functional efficacy for lapatinib in GS025 compared to the other two TKIs (Figure 1B and D). These data are consistent with lapatinib having lower activity against active wtEGFR.[6] Together, these results indicate that **5** can potently inhibit the signaling and growth of EGFRvIII mutant and EGFR amplified primary GBM cells at levels on par with or better than that of both erlotinib and lapatinib.

We next carried out a similar evaluation in an orthotopic GBM xenograft model. To do this comparison in the most clinically relevant manner, we first established the clinically relevant dose of erlotinib and lapatinib in which the plasma exposures in mice matches that of human plasma levels at the standard clinical dose.[29,30] Erlotinib and lapatinib administered at 10 mg/kg and 80 mg/kg in non-tumor bearing mice reached plasma exposures of 51,689 nM·hr and 44,807 nM·hr over 24 hours, respectively; which, mirrors the 24-hour human clinical plasma exposures for both drugs.[31,32] However, due to the low bioavailability of **5** of approximately 4.7% (Figure S4), we dosed at 300 mg/kg BID to achieve plasma exposures of **5** similar to that of the clinically relevant doses of both erlotinib and lapatinib in non-tumor bearing mice (Figure 2A).

With the relevant doses established, we next implanted EGFRvIII mutant GBM39 into the brains of NOD-SCID Gamma mice. Once tumors reached exponential growth, as determined by secreted *gaussia* luciferase,[33] tumors were analyzed by immunoblotting for activation of EGFRvIII and its downstream signaling effectors. In comparison to vehicle treated tumors, erlotinib and lapatinib treatment showed no significant difference in EGFRvIII activation (Figure 2B). Similarly, erlotinib and lapatinib did not significantly inhibit signaling pathways downstream of EGFR, including RAS-MAPK (via p-ERK) or PI3K-AKT-mTOR (via pAKT and pS6) signaling (Figure 2B and C). These observations are in agreement with clinical data suggesting that erlotinib and lapatinib do not reach sufficient levels in glioblastoma tumors to consistently inhibit EGFR signaling.[4,6,34] Conversely, tumors from **5**-treated mice showed a significant decrease in EGFRvIII activity that was associated with reduced RAS-MAPK and PI3K-AKT-mTOR signaling (Figure 2B and C). These data support the hypothesis that the heightened BBB penetration of **5** would result in a greater capacity to inhibit EGFR signaling in an orthotopic GBM xenograft model.

Next, to compare the anti-tumor efficacy of **5** against erlotinib and lapatinib, a second cohort of orthotopic GBM39 tumor-bearing mice was established with the same doses and schedules as the above pharmacodynamic studies with the various EGFR TKIs. We observed no significant differences in tumor growth nor survival with erlotinib or lapatinib treatment (Figure 2D and E). In contrast, a notable reduction in tumor proliferation was identified in **5**-treated mice (Figure 2F), with no significant loss in body weight (Figure S6). Moreover, **5** treatment provided a significant survival benefit, whereby median survival increased by 47% from 37.5 days to 55 days with **5** treatment (Figure 2G). Taken together, these data show that, in contrast to clinically relevant doses of erlotinib and lapatinib, **5** robustly inhibits EGFR signaling and tumor growth, and prolongs the survival of mice bearing EGFR mutant, orthotopic GBM xenografts.

To gain greater insight into the low bioavailability and potential metabolic liabilities of **5**, we investigated its *in vitro* clearance using liver microsomes. We observed a rapid hydroxylation of the fused 1,4-dioxane ring, suggesting first pass metabolism contributed to low oral bioavailability (Figure S7). Our hypothesis was confirmed by the co-administration of the cytochrome p450 inhibitor, 1-aminobenzotriazole; which resulted in a 3-fold increase in exposure of **5** (Figure S8). To explore this issue, we made modifications at the metabolic labile site of the fused 1,4-dioxane ring moiety by perdeuteration, as well as adding vicinal methyl groups on the 1,4-dioxane ring (Figure S9). Perdeuteration was unable to alter the bioavailability in mice compared to **5**. Conversely, the addition of vicinal methyl groups on the 1,4-dioxane ring significantly improved plasma exposures and bioavailability in mice suggesting a potential location for future modifications on this scaffold.

Recent evidence suggests that Type I EGFR TKIs inhibitors – which favor the active confirmation of EGFR – have less affinity for mutant EGFRvIII relative to Type II EGFR TKIs,

which prefer the inactive form of the receptor.[6] Given that compound **5** can potently inhibit both wtEGFR and EGFRvIII, we performed a molecular docking study to elucidate on a molecular level how this dual specificity of **5** is achieved. The docking results of **5,** displayed in Figure 3 (and Figure S10), suggest the typical type I TKI binding mode occurs as is also observed for e.g. erlotinib (cf. Figure S1), through hydrogen bond interactions with hinge residues and gatekeeper residues mediated through crystallographic water molecule(s). According to our docking results, no clear difference in the binding to the active and inactive EGFR conformations can be discerned, except for a slightly closer fit of the dioxane and aniline part of **5** into the binding pocket of the inactive conformation. The gain in efficacy and selectivity upon introduction of the 2'-fluorine might be attributed to several orthogonal multipolar interactions of this fluorine to nearby apolar residues including a hypothesized C–F···C=O contact with Ala719/743 (active/inactive).[23] Collectively, although the conformation selectivity for EGFR TKIs is an intriguing effect that is not yet fully understood,[35] we observed **5** may have the ability to bind both the active and inactive conformations of EGFR, which may contribute to its potency for both wtEGFR and EGFRvIII, respectively.

The synthesis of the analogues **1**–**19** is summarized in Scheme 1. The quinazoline core was made according to the Niementowski quinazoline synthesis from methyl 3,4-dimethoxyanthranilate (**20**). The dimethoxy groups of quinazolinone **21** were replaced with pivaloyl groups to obtain **22**. Chlorination with $POCl_3$, followed by deprotection gave intermediate **23**, which was alkylated with 1-bromo-2-chloroethane to obtain the 1,4-dioxane-fused 4-chloroquinazoline **24**.

Preparation of the final analogues was accomplished by S_NAr of **24** with the respective anilines (see also Scheme S1), or by transition-metal catalyzed transformations of **4** or **5**. To

prepare sufficient material of our lead compound **5** for all in vivo testing, we devised the shorter route of Scheme S2, which comprises five steps and is based on a Dimroth cyclization.

DISCUSSION

In summary, herein we have described the synthesis of a novel, brain-penetrant EGFR TKI with high activity against EGFR altered primary GBM cells both in culture and in orthotopic xenografts. Compound **5** was developed by first modifying erlotinib via ring fusion of the 6,7-alkoxy groups. Similar dioxane-containing anilinoquinazoline compounds have been described before for the purpose of improved solubility;[25,37] yet, here we determined that this modification also leads to unforeseen BBB penetration, potentially as a result of the more optimal physicochemical properties and impaired P-gp and BCRP substrate identification. Moreover, **5** contains both a 2'-fluorine and 3'-bromine on the aniline ring; these substitutions further improved brain penetration, while providing nearly equipotent activity against both oncogenic activated wtEGFR and mutant EGFRvIII. While the EGFR TKIs developed specifically for EGFR-mutated lung cancer, osimertinib and AZD3759, both have reported high brain penetration (Table S5),[9,19] osimertinib lacks the ability to effectively inhibit wtEGFR that is prevalent across GBM[3] (Figure S11), and AZD3759 has reduced activity against EGFRvIII relative to **5** (Figure S12). These differences may explain the improved potency of **5** against EGFR altered primary GBM cells compared to either osimertinib or AZD3759 (Figures S11, S12).

In contrast to the observation that some EGFR TKIs may promote paradoxical induction of cell growth,[38] compound **5** – nor any other EGFR TKI tested – did not (Figure S13). Rather, despite the low bioavailability of **5** (4.7%), it significantly suppressed *in vivo* tumor growth via oral administration. As we have shown (Figure S7), the main liability of compound **5** is fast clearance through first-pass metabolism. Therefore, future work will be aimed at identifying drug

candidates with improved bioavailability and other ADME properties to obtain an optimal clinical EGFR TKI for GBM tumors with EGFR alterations.

FIGURES AND TABLES

Chapter 1 – Table 1. Comparison of physicochemical properties for CNS drugs, FDA-approved kinase inhibitors, and EGFR kinase inhibitors.

Physicochemical property	CNS drugs (preferred range, n = 317)[a]	CNS drugs (median, n = 119)[b]	FDA-approved protein kinase inhibitors (median, n = 49)[c]	Clinical EGFR kinase inhibitors (median, n = 25)[c,d]
MW	250–355	305	486	491
clogP	2.1–4.4	2.8	4.2	4.5
clogD$_{7.4}$	1.2–3.1	1.7	3.3	3.9
HBD	0–1	1	2	2
HBA	2–3	N/A	7	7
TPSA (Å^2)	25–60	45	94	89
NRB	1–4	N/A	6	8
Most basic center (pK_a)	7.9–10.7	8.4	7.1	7.7

[a]Preferred ranges for physicochemical properties from [13]. [b]Median values from [14]. [c]For at least 7 out of 49 FDA-approved kinase inhibitors, brain-penetration data has been reported.[12] [d]EGFR kinase inhibitors approved by any agency or in clinical development (non-comprehensive). N/A, no data provided.

Chapter 1 – Table 2. Compared to erlotinib, a fused dioxane ring improves brain penetration, but reduces potency; while the addition of an *ortho*-fluorine on the aniline ring improves potency while retaining BBB penetration.

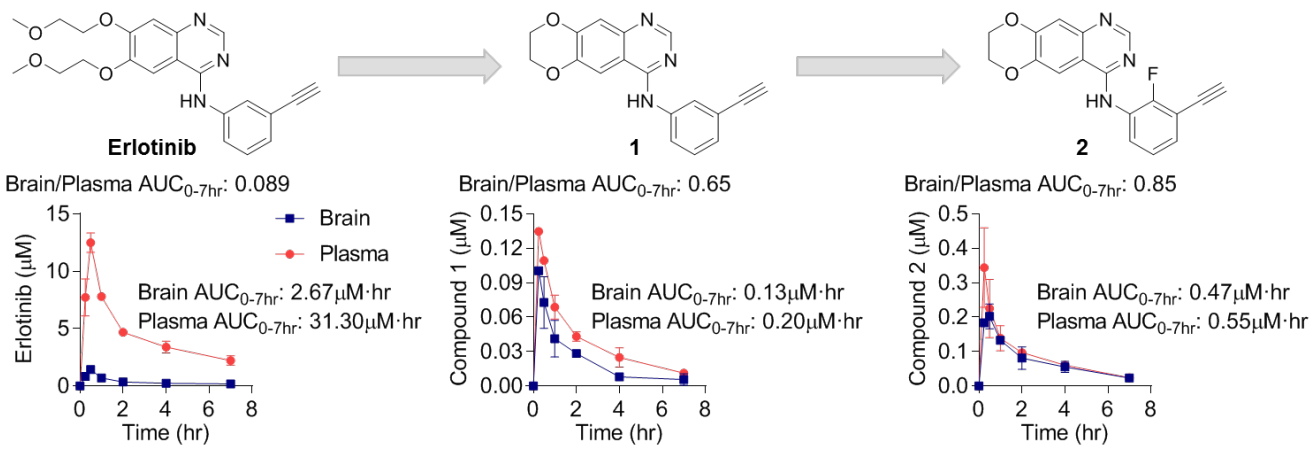

Compound	MW	clogP	HBA	TPSA (Å)	NRB	EGFR IC_{50} (nM)	p-wtEGFR IC_{50} (nM)	p-EGFRvIII IC_{50} (nM)	HK301 GI_{50} (nM)	GBM39 GI_{50} (nM)
Erlotinib	393	2.39	7	75	10	2.17 ±0.58	3.90 ±0.24	12.5 ±1.1	700.2 ±76.8	2788 ±179
1	303	2.98	5	56	2	48.7 ±7.8	59.8 ±1.6	188.4 ±26.9	8824 ±1109	20536 ±1212
2	321	3.71	5	56	2	19.7 ±3.7	20.5 ±0.1	32.2 ±1.2	791.1 ±108.1	2946 ±353

All EGFR inhibition data are represented as mean ± SEM from *n*=2 or more independent replicates. All growth inhibition data are represented as mean ± SEM from *n*=3 or more independent replicates.

Chapter 1 – Table 3. Comparison of the 2'- and 3'-position of 4-anilinoquinazolines.

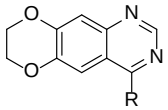

3–11

Compound	R	EGFR IC_{50} (nM)	p-wtEGFR IC_{50} (nM)	p-EGFRvIII IC_{50} (nM)	HK301 GI_{50} (nM)	GBM39 GI_{50} (nM)
3	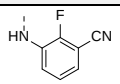	22.0 ±3.9	28.2 ±3.8	54.8 ±4.8	3262 ±538	7266 ±925
4	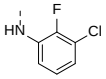	3.91 ±0.80	4.70 ±0.32	6.21 ±0.01	780.5 ±148.3	2594 ±299
5	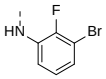	2.49 ±0.65	3.95 ±0.24	4.48 ±0.22	329.3 ±31.0	1116 ±114.9
6	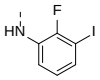	10.4 ±2.0	13.1 ±0.8	44.8 ±1.3	2042 ±341	4521 ±574
7	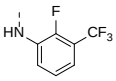	41.4 ±8.6	55.0 ±2.2	75.4 ±7.5	3614 ±385	7820 ±1087
8	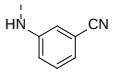	24.0 ±4.8	45.3 ±3.7	83.5 ±3.7	3940 ±77	10939 ±1079
9	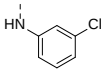	6.41 ±0.95	8.80 ±0.82	22.0 ±1.8	1167 ±203	2968 ±14
10	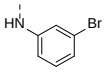	13.6 ±3.3	15.5 ±0.7	43.1 ±1.1	2055 ±173	6073 ±189
11	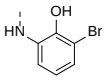	505.1 ±102.2	729.1 ±172.9	2312.0 ±260.4	17697 ±482	51536 ±3980
Erlotinib		2.17 ±0.58	3.90 ±0.24	12.5 ±1.1	700.2 ±76.8	2788 ±179

All EGFR inhibition data are represented as mean ± SEM from *n*=2 or more independent replicates. All growth inhibition data are represented as mean ± SEM from *n*=3 or more independent replicates.

Chapter 1 – Table 4. Modifications of the 4', 5', and 6'-positions of 3'-bromo-2'-fluoro-substituted 4-anilinoquinazolines.

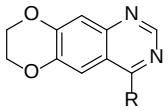

12–19

Compound	R	EGFR IC_{50} (nM)	p-wtEGFR IC_{50} (nM)	p-EGFRvIII IC_{50} (nM)	HK301 GI_{50} (nM)	GBM39 GI_{50} (nM)
12	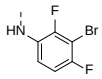	15.6 ±2.3	21.9 ±1.7	57.8 ±6.6	1383 ±165	10300 ±1138
13	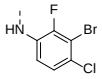	16.2 ±2.5	25.3 ±1.2	30.8 ±3.9	2778 ±184	5277 ±523
14	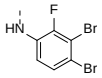	21.0 ±3.5	32.6 ±4.9	36.1 ±5.8	5723 ±314	7697 ±1346
15	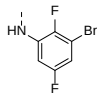	6.16 ±1.14	6.80 ±0.50	16.2 ±2.4	1132 ±64	1727 ±244
16	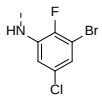	782.8 ±164.1	2186.0 ±152.0	3846.0 ±259.5	1853 ±239	12741 ±342
17	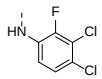	25.0 ±3.2	36.7 ±0.1	40.1 ±7.4	3681 ±738	4226 ±371
18	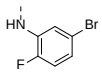	7.63 ±1.62	11.1 ±0.5	10.8 ±0.2	290.1 ±32.7	966.4 ±163.4
19	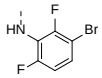	10.0 ±2.29	15.8 ±0.7	27.6 ±2.7	418.7 ±62.7	1356 ±196.3
5	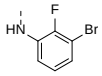	2.49 ±0.65	3.95 ±0.24	4.48 ±0.22	329.3 ±31.0	1116 ±114.9
Erlotinib		2.17 ±0.58	3.90 ±0.24	12.5 ±1.1	700.2 ±76.8	2788 ±179

All EGFR inhibition data are represented as mean ± SEM from *n*=2 or more independent replicates. All growth inhibition data are represented as mean ± SEM from *n*=3 or more independent replicates.

Chapter 1 – Table 5. Brain penetration and in vivo parameters of select compounds.[a]

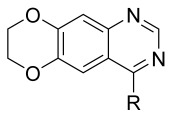

Compound	R	Brain $AUC_{0–7\ h}$ (μM·hr)	Plasma $AUC_{0–7\ h}$ (μM·hr)	Brain/Plasma Ratio [b]	$K_{p,uu,brain}$ [c]	P_{app} [d] (10^{-6} cm/s)	Efflux Ratio[e]
1	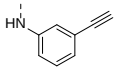	0.128	0.199	0.648	0.491	16.9	0.601
2	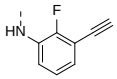	0.466	0.553	0.843	0.575	21.5	0.387
S3	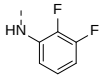	0.344	0.324	1.062	1.04	20.0	0.238
4	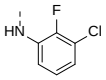	0.403	0.378	1.064	1.04	28.5	0.611
5	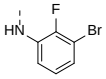	0.470	0.221	2.118	1.30	15.0	0.577
6	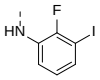	1.676	0.752	1.676	1.03	14.4	0.484
Erlotinib		2.670	31.3	0.085	0.051	34[28]	4.63[9]

[a]All brain and plasma AUC_{0-7h} determined after oral administration of 10 mg/kg in male CD-1 mice. [b]Brain/Plasma ratios determined over 0–7 h. [c]Ratio of the unbound concentration in the brain to that of plasma. [d]Permeability determined using MDCK-MDR1 cells. [e]Ratio of P_{app} B-A / P_{app} A-B.

Chapter 1 – Figure 1

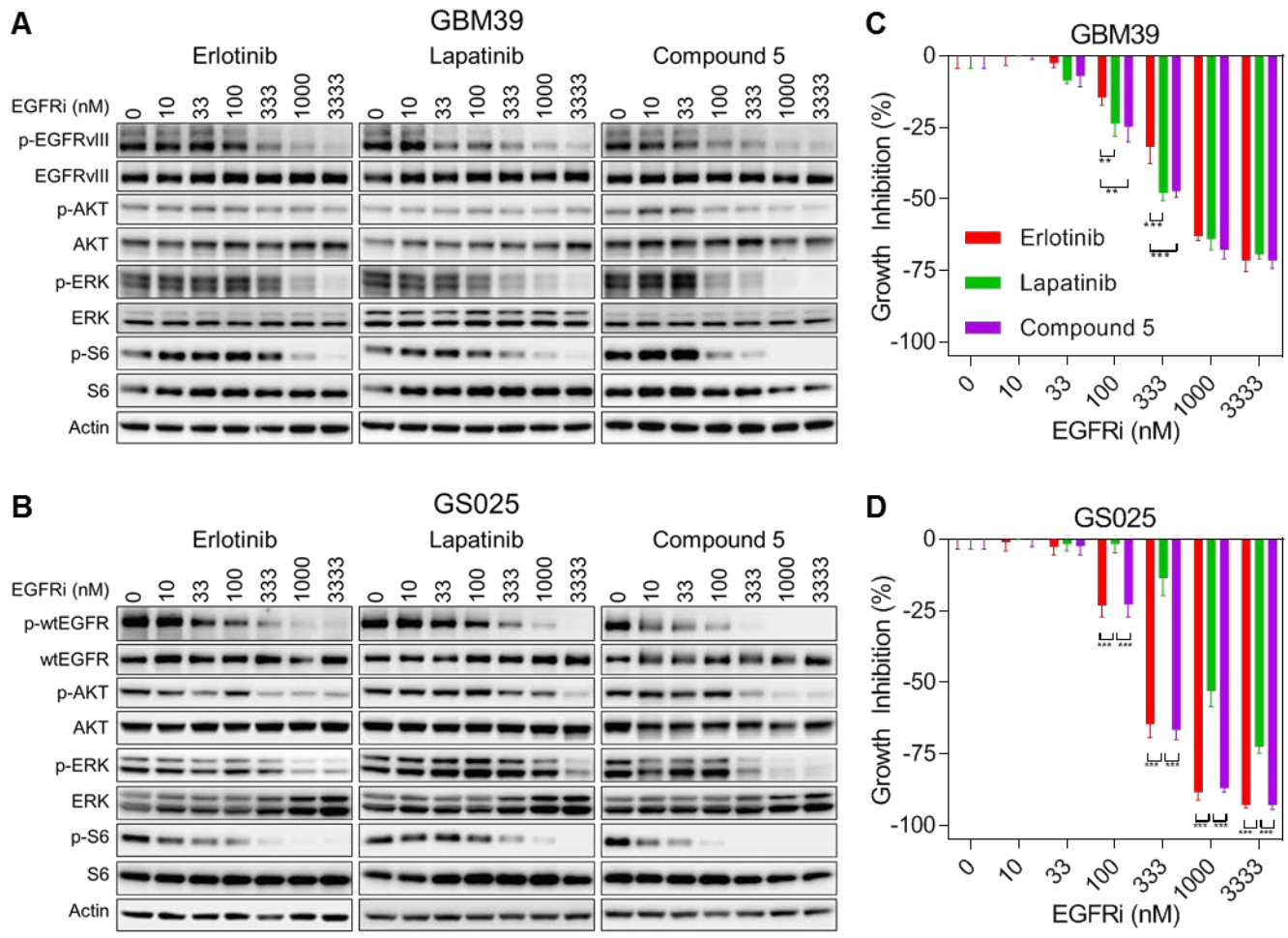

Figure 1. Biochemical and functional activity of **5**, lapatinib, and erlotinib on EGFRvIII mutant and EGFR amplified patient-derived GBM cells. Immunoblot of EGFR signaling components in (A) EGFRvIII mutant patient-derived GBM39 cells and (B) amplified EGFR patient-derived GS025 cells. Growth inhibition of (C) GBM39 and (D) GS025 cells relative to vehicle. All growth inhibition data are represented as mean ± SEM from *n*=3 independent replicates. * $p<0.05$, ** $p<0.01$, ***$p<0.001$.

Chapter 1 – Figure 2

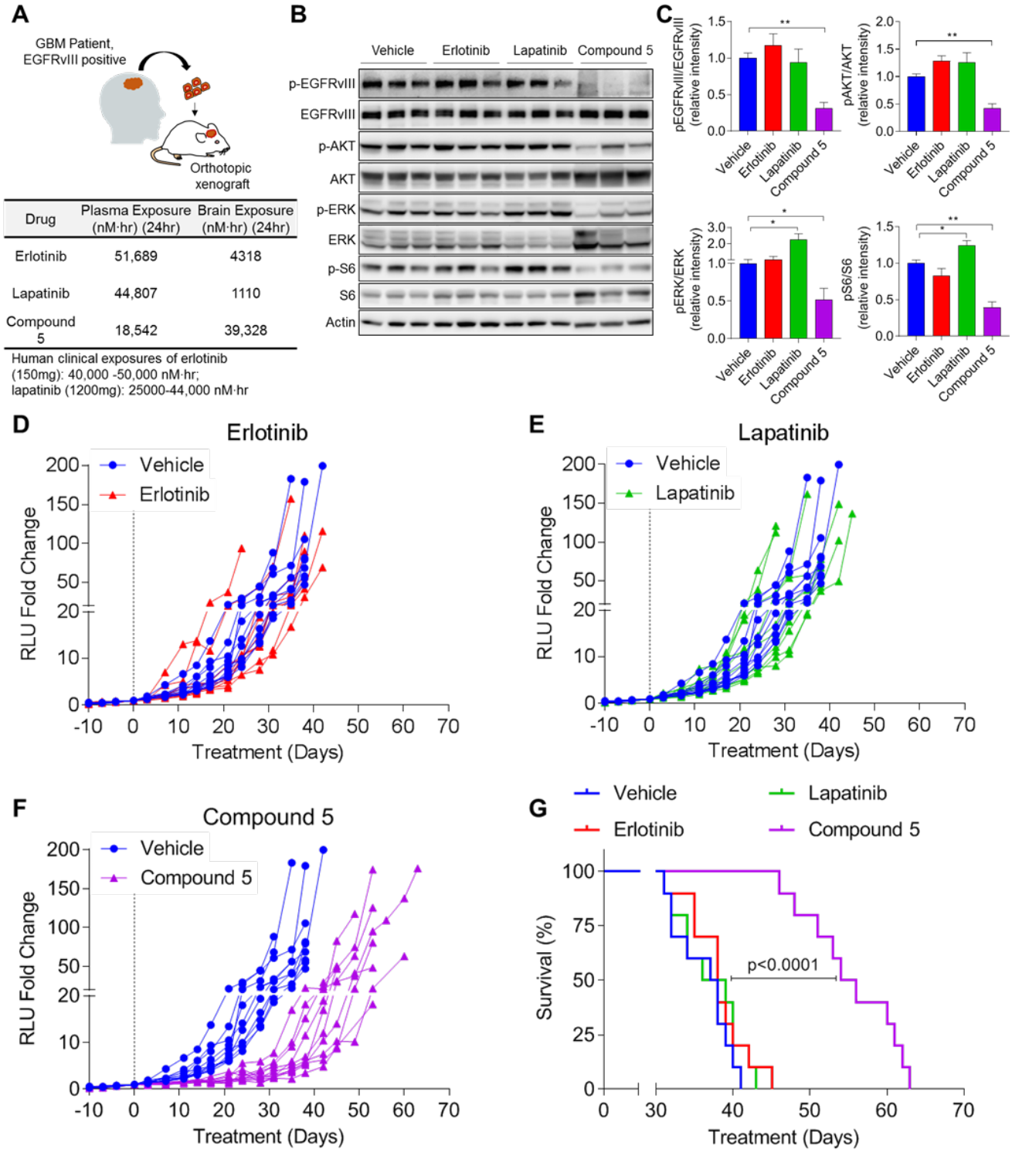

Drug	Plasma Exposure (nM·hr) (24hr)	Brain Exposure (nM·hr) (24hr)
Erlotinib	51,689	4318
Lapatinib	44,807	1110
Compound 5	18,542	39,328

Human clinical exposures of erlotinib (150mg): 40,000 -50,000 nM·hr; lapatinib (1200mg): 25000-44,000 nM·hr

Figure 2. *In vivo* pharmacodynamics and efficacy of erlotinib, lapatinib, and **5** against EGFRvIII mutant patient-derived orthotopic GBM39 xenografts. (A) Plasma and brain exposures of erlotinib (10 mg/kg), lapatinib (80 mg/kg) and **5** (300 mg/kg) in mice. Below are the published human 24-hour plasma exposures of erlotinib and lapatinib at clinical doses. (B) Immunoblot of EGFR signaling components of orthotopic GBM39 xenografts following 3 days of oral administration of the indicated drugs or vehicle. (C) Quantification of immunoblot in (B). All quantified immunoblot data are represented as mean ± SEM of n=3 independent replicates. * $p<0.05$, ** $p<0.01$, ***$p<0.001$. Intracranial GBM39 growth of daily (D) erlotinib, (E) lapatinib, or (F) twice daily treatment of **5**. (G) Survival of mice from (D)–(F).

Chapter 1 – Figure 3

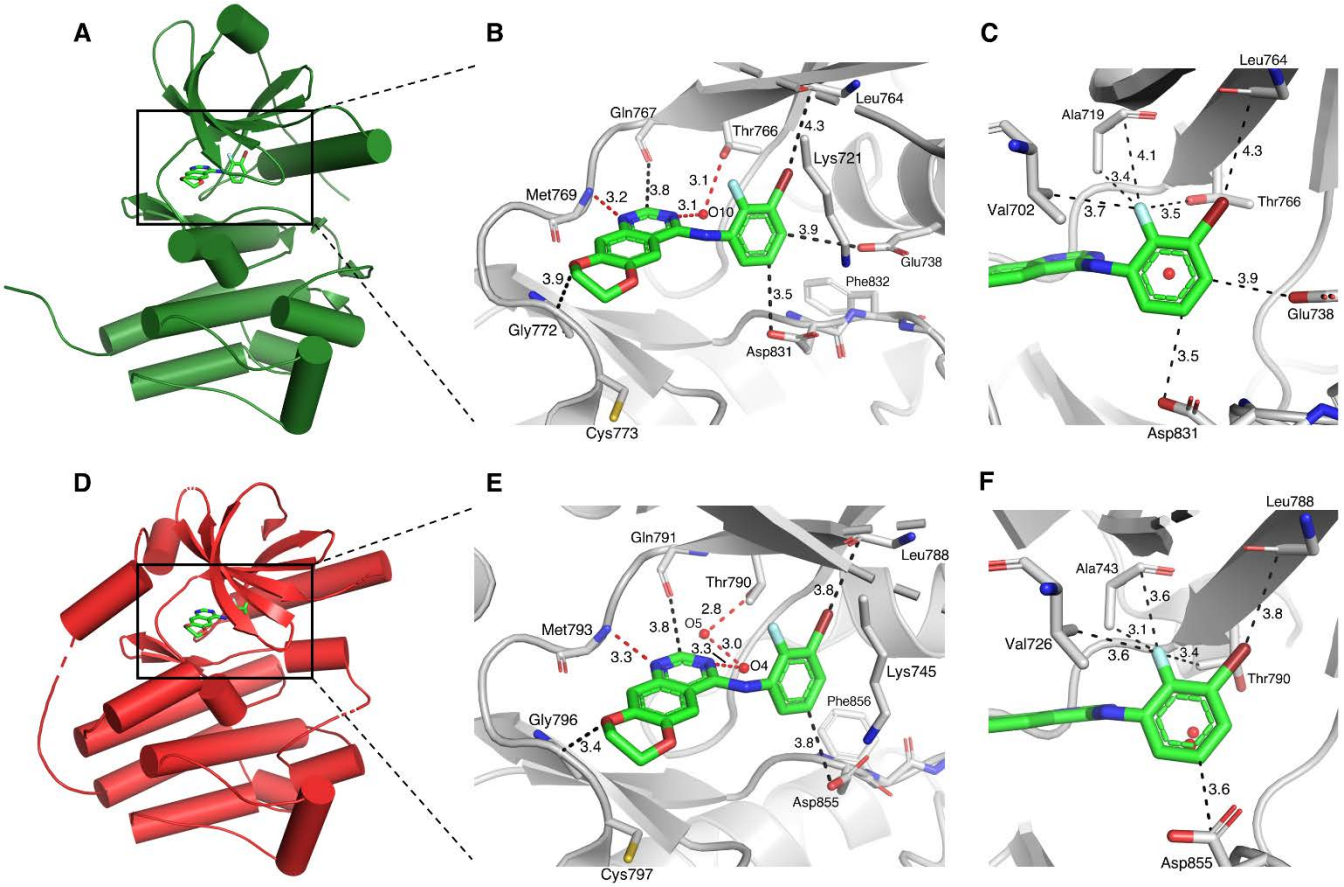

Figure 3. Predicted binding mode of **5** to active and inactive wtEGFR kinase domain. **5** was docked with AutoDock Vina to active EGFR (PDB 1M17)[18] as shown in (A), (B), and (C), and to inactive EGFR (PDB 1XKK),[36] as shown in (D), (E), and (F). Color code: C_{enzyme} gray, O red, N blue, C_{ligand} green, F light blue, Br dark red.

Chapter 1 – Scheme 1

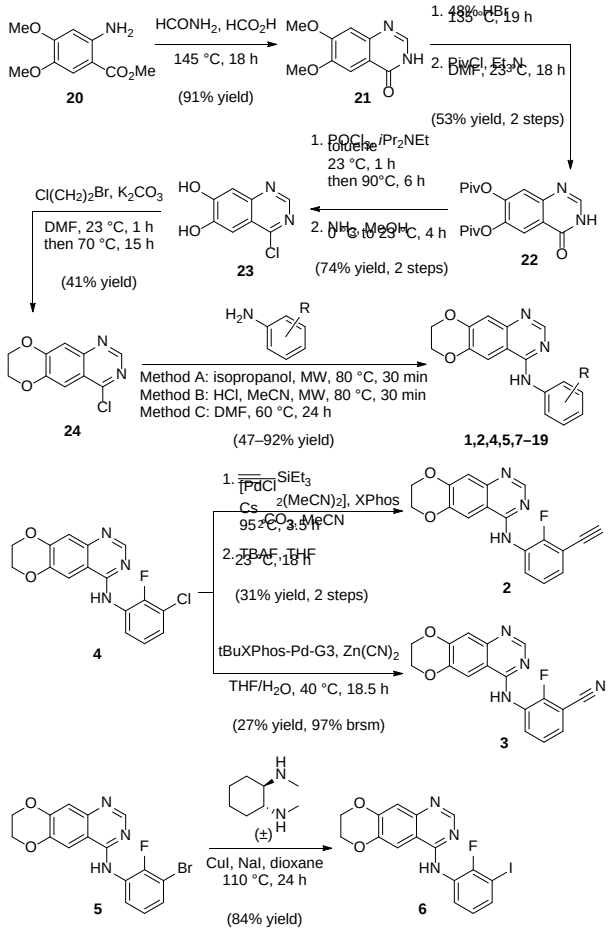

Scheme 1. Synthesis of 7,8-dihydro[1,4]dioxino[2,3-*g*]quinazolin-4-amines **1**–**19**.

SUPPLEMENTARY FIGURES AND TABLES

As an illustration of the characteristic protein interactions of the type I scaffold, Figure S1 shows the binding mode of erlotinib to the ATP-binding pocket of EGFR and, for comparison, the binding mode of its natural substrate ATP.[18,35,39] The "classical" binding interactions comprise two hydrogen bonds formed between N1 and N3 of the quinazoline with hinge residue Met769 and "gatekeeper" residue Thr766 (mediated through a water molecule (O10)) (Figure S1C), which mimic those of the adenine ring of ATP[39] (Figure S1D), and the filling of the apolar hole at the back of the binding site by the aniline ring with the 3'-alkyne substituent pointing into the hydrophobic "chimney" (as termed by Bridges[40]) at the end of the apolar hole. The substituents at C6 and C7 of the quinazoline protrude from the binding cleft into the solvent channel (Figure S1B), making minimal interactions with the protein environment, but are important for pharmacological properties.[11,17] These positions (C6 and C7) are known to be tolerant of substitution as opposed to C2, C5, and C8, and substituents are preferably attached via electron donating groups to the quinazoline.[17,41] The compounds of Table S1, **S1**–**S8**, were prepared according to all other anilinoquinazoline compounds as outlined in Scheme 1.

Chapter 1 – Figure S1

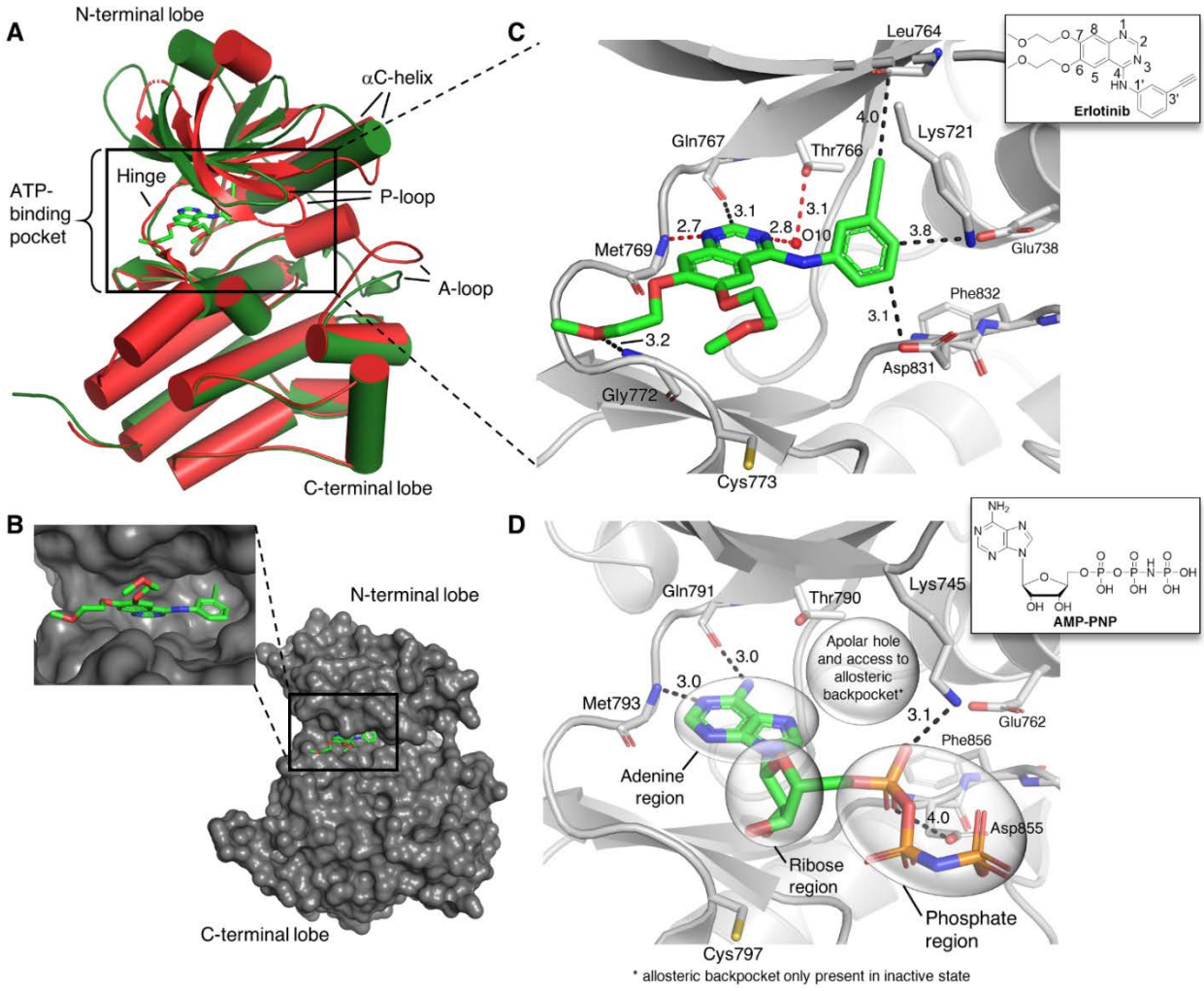

Figure S1. Structure of the EGFR kinase domain and binding mode at the ATP-binding pocket. (A) Active (green, PDB 1M17)[18] and inactive (red, PDB 4HJO)[35] EGFR kinase domains superimposed on their C-terminal lobes. The ATP-binding site is occupied by erlotinib (sticks). The main structural elements are labelled, but more detailed descriptions can be found in the relevant biophysical publications. (B) Surface representation of the active EGFR kinase domain in complex with erlotinib (PDB 1M17). The expanded view shows erlotinib in the narrow binding cleft with the apolar hole at the back filled by the aniline ring. (C) Binding mode of erlotinib at the ATP-binding pocket (PDB 1M17). "Classical" hydrogen bonds are indicated as dashed, red lines, and additional close contact interactions are shown as dashed, black lines. (D) Binding mode of the non-hydrolyzable ATP-analogue AMP-PNP at the ATP-binding pocket (PDB 3VJO).[39] The apolar hole is not occupied by ATP. The P-loops have been removed for clarity in (C) and (D). Color code: C_{enzyme} gray, O red, N blue, P orange, C_{ligand} green. Distances are in Å.

Chapter 1 – Table S1. SAR of placing fluorine(s) on the aniline ring of the 4-anilinoquinazolines.

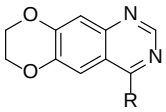

S1–S8

Compound	R	EGFR IC_{50} (nM)	p-wtEGFR IC_{50} (nM)	p-EGFRvIII IC_{50} (nM)	HK301 GI_{50} (nM)	GBM39 GI_{50} (nM)
S1		57.3 ±22.6	64.1 ±4.8	169.4 ±10.4	4040 ±553	9998 ±1529
S2	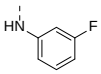	107.3 ±18.6	86.5 ±4.0	379.0 ±54.3	3238 ±124	10221 ±1320
S3	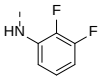	18.9 ±3.6	28.9 ±1.4	109.6 ±4.4	1688 ±188	5572 ±371
S4		363.0 ±49.7	435.1 ±50.9	851.9 ±68.4	10659 ±1487	27706 ±5589
S5		115.0 ±15.9	92.7 ±0.8	304.4 ±17.0	6124 ±1041	16525 ±1817
S6		50.0 ±10.5	40.0 ±3.9	211.1 ±54.4	5807 ±675	11837 ±2197
S7		427.9 ±41.1	362.4 ±106.5	1319.6 ±136.4	24395 ±1333	33970 ±5345
S8		1243.0 ±142.0	4785.5 ±385.7	10935 ±641.4	>100000	>100000

All EGFR inhibition data are represented as mean ± SEM from *n*=2 or more independent replicates. All growth inhibition data are represented as mean ± SEM from *n*=3 or more independent replicates.

Chapter 1 – Figure S2

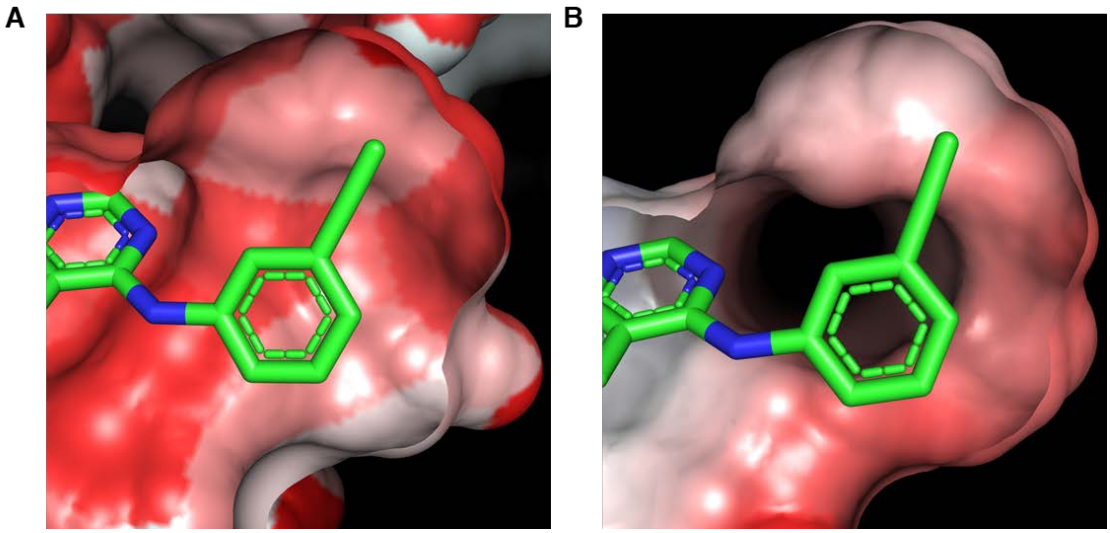

Figure S2. Surface representations of the apolar hole of the wtEGFR kinase domain (PDB 1M17) with bound erlotinib. A) Lipophilic surface according to the Eisenberg hydrophobicity scale, generated with the PyMOL color_h script; color code: red = lipophilic, white = hydrophilic surface area. B) Electrostatic surface, generated with the PyMOL APBS plugin; color code: red = increasing negative potential, blue = increasing positive surface potential.

Chapter 1 – Table S2. Calculated physicochemical properties of compound **5** and related 3'-halide substituted compounds.

Compound	clogD at pH 7.4[a]	IC_{50} (nM)
S3	3.26	18.9
4	3.72	3.91
5	3.88	2.49
6	4.04	10.4

[a] Calculated with Chemicalize, ChemAxon.

Chapter 1 – Figure S3

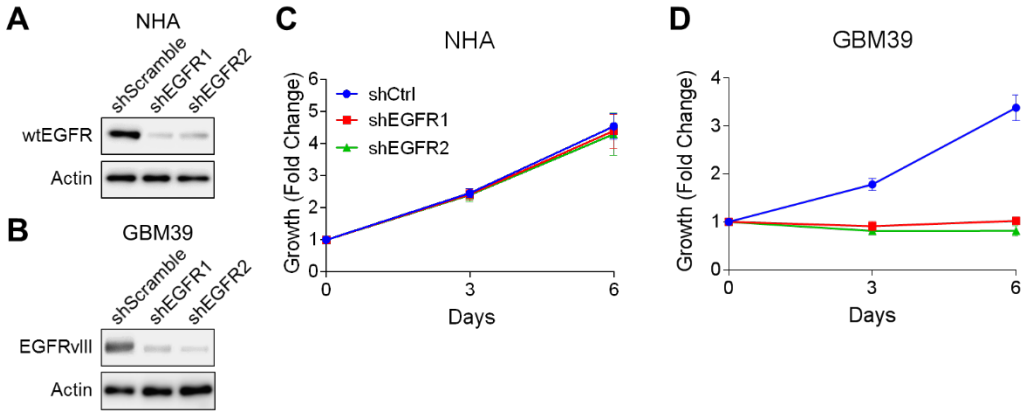

Figure S3. NHAs are not dependent on EGFR for growth. (A) Immunoblot of EGFR and actin in NHA cells transduced with shRNA against a scramble control and EGFR. (B) Same as (A) but with EGFRvIII and actin in GBM39. (C) Proliferation of NHA cells from (A).

Chapter 1 – Table S3. GI50 of NHAs and primary GBM lines of potent compounds.

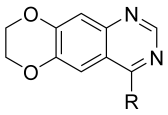

Compound	R	HK301 GI_{50}[a] (nM)	GBM39 GI_{50}[b] (nM)	NHA GI_{50}[c] (nM)	Ratio of NHA/HK301 GI_{50}	Ratio of NHA/GBM39 GI_{50}
Erlotinib		700.2 ±76.8	2788 ±179	43312 ±3837	62.1	15.6
Lapatinib		1290 ±144	2101 ±370	16186 ±2321	12.5	7.7
1	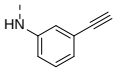	8824 ±1109	20536 ±1212	>100000	11.3	4.9
2	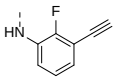	791.1 ±108.1	2946 ±353	6647 ±597	7.7	2.1
S3	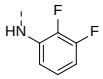	1688 ±188	5572 ±371	23905 ±2063	14.6	4.4
4	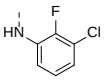	780.5 ±148.3	2594 ±299	7616 ±328	9.8	2.9
5	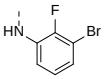	329.3 ±31.0	1116 ±114.9	8168 ±346	24.7	7.3
6	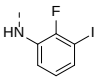	2042 ±341	4521 ±574	9336 ±609	4.6	2.1
15	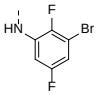	3681 ±738	4226 ±371	670 ±185	0.6	0.4
18	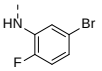	290.1 ±32.7	966.4 ±163.4	1430 ±259	4.9	1.5
19	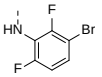	418.7 ±62.7	1356 ±196.3	1167 ±175	2.8	0.9

[a]3 day growth inhibition in patient-derived GBM line, HK301. [b]3 day growth inhibition in patient-derived GBM line, GBM39. [c]3 day growth inhibition in NHA. All growth inhibition data are represented as mean ± SEM from *n*=3 or more independent replicates.

Chapter 1 – Figure S4

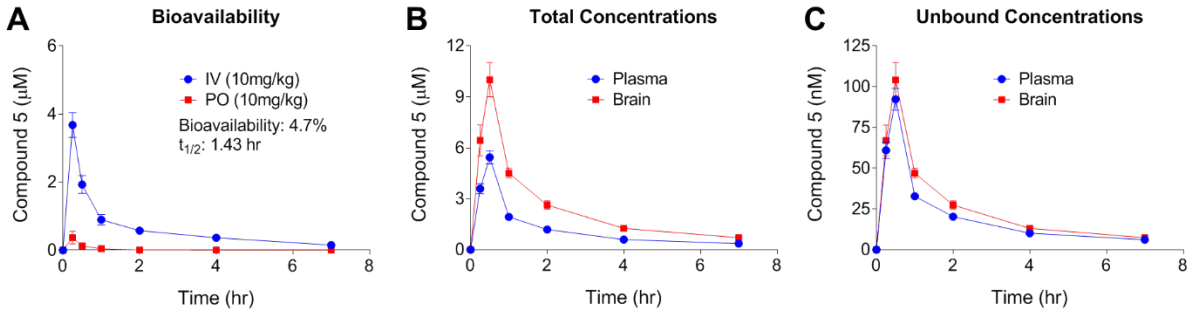

D

Drug	Bioavailability (%)	Plasma Exposure (nM·hr) (24hr)	Brain Exposure (nM·hr) (24hr)	Brain Penetration (%)	Kp,uu	$t_{1/2}$ (hr)
Compound 5	4.7	18,542	39,328	212.11%	1.30	1.43

E

Drug	AUC (total, plasma) (nM·hr) (24hr)	AUC (total, brain) (nM·hr) (24hr)	AUC (unbound, plasma) (nM·hr) (24hr)	AUC (unbound, brain) (nM·hr) (24hr)
Erlotinib	51,689	4,318	2519.8	126.5
Lapatinib	44,807	1,110	448.1	16.0
Compound 5	18,542	39,328	315.2	409.0

Figure S4. Pharmacokinetics of compound **5**. (A) Oral bioavailability of compound **5**. (B) Total plasma and brain concentrations of compound **5** in healthy CD-1 mice. (C) Unbound plasma and brain concentrations of compound **5** in healthy CD-1 mice. (D) Pharmacokinetics parameters of compound **5**. (E) Exposures of erlotinib (10mg/kg), lapatinib (80mg/kg), and compound **5** (300mg/kg) in plasma and brain for total and unbound.

Chapter 1 - Table S4. Permeability of **5** in MDCK-BCRP transwell cells.

Compound	Concentration (μM)	P_{app} (10^{-6} cm/s)	Efflux Ratio[e]
5	10	18.59	0.303

Chapter 1 – Figure S5

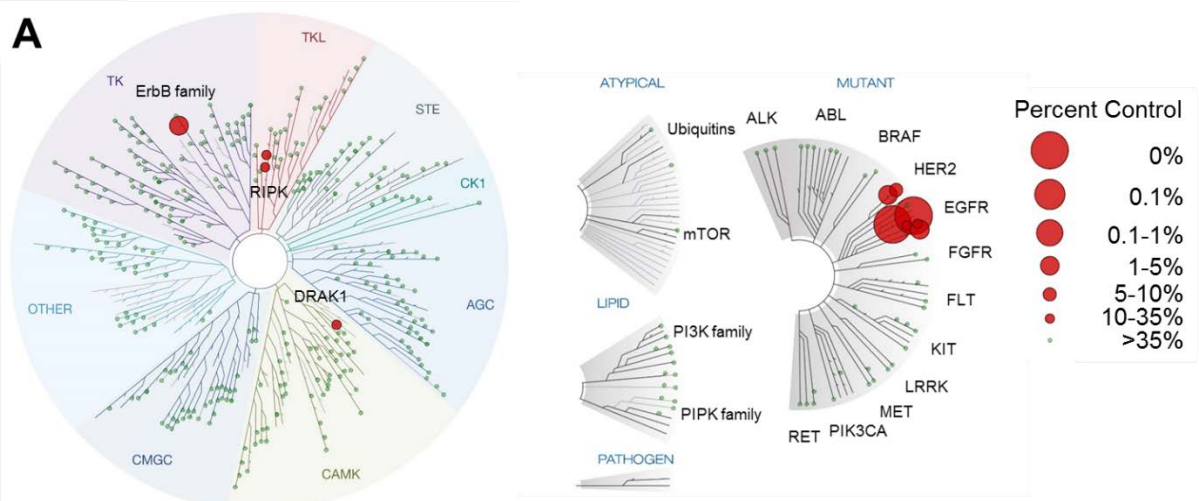

B

#	Kinase	Compound 5 % Kinase Inhibition (1µM)
1	AAK1	1
2	ABL1	4
3	ABL2 (Arg)	2
4	ACVR1 (ALK2)	6
5	ACVR1B (ALK4)	-1
6	ACVR2A	-7
7	ACVR2B	-8
8	ACVRL1 (ALK1)	-2
9	ADCK3	9
10	ADRBK1 (GRK2)	-3
11	ADRBK2 (GRK3)	-1
12	AKT1 (PKB alpha)	3
13	AKT2 (PKB beta)	4
14	AKT3 (PKB gamma)	6
15	ALK	9
16	AMPK (A1/B1/G2)	-6
17	AMPK (A1/B1/G3)	-6
18	AMPK (A1/B2/G1)	1
19	AMPK (A1/B2/G2)	0
20	AMPK (A1/B2/G3)	0
21	AMPK (A2/B1/G2)	1
22	AMPK (A2/B1/G3)	-2
23	AMPK (A2/B2/G1)	-4
24	AMPK (A2/B2/G2)	-1
25	AMPK (A2/B2/G3)	-1
26	AMPK A1/B1/G1	-5
27	AMPK A2/B1/G1	5
28	ANKK1	-5
29	AURKA (Aurora A)	0
30	AURKB (Aurora B)	6
31	AURKC (Aurora C)	11
32	AXL	-1
33	BLK	6
34	BMPR1A (ALK3)	-6
35	BMPR1B (ALK6)	-2
36	BMPR2	1
37	BMX	0
38	BRAF	3
39	BRAF	-3
40	BRSK1 (SAD1)	1
41	BRSK2	-5
42	BTK	0
43	CAMK1 (CaMK1)	-2
44	CAMK1D (CaMKI delta)	-1
45	CAMK1G (CAMKI gamma)	-4
46	CAMK2A (CaMKII alpha)	6
47	CAMK2B (CaMKII beta)	5
48	CAMK2D (CaMKII delta)	3
49	CAMK2G (CaMKII gamma)	-5
50	CAMK4 (CaMKIV)	12
51	CAMKK1 (CAMKKA)	-5
52	CAMKK2 (CaMKK beta)	-3
53	CASK	-8
54	CDC42 BPA (MRCKA)	1
55	CDC42 BPB (MRCKB)	-1
56	CDC42 BPG (MRCKG)	-3
57	CDC7/DBF4	3
58	CDK1/cyclin B	2
59	CDK11 (Inactive)	-13
60	CDK11/cyclin C	6
61	CDK13/cyclin K	-4
62	CDK14 (PFTK1)/cyclin Y	-3
63	CDK16 (PCTK1)/cyclin Y	-4
64	CDK17/cyclin Y	4
65	CDK18/cyclin Y	3
66	CDK2/cyclin A	2
67	CDK2/cyclin A1	-1
68	CDK2/cyclin E1	-5
69	CDK2/cyclin O	-4
70	CDK3/cyclin E1	-7
71	CDK4/cyclin D1	22
72	CDK4/cyclin D3	-10
73	CDK5 (Inactive)	-4
74	CDK5/p25	2
75	CDK5/p35	1
76	CDK6/cyclin D1	3
77	CDK7/cyclin H/MNAT1	3
78	CDK8/cyclin C	0
79	CDK9 (Inactive)	-4
80	CDK9/cyclin K	2
81	CDK9/cyclin T1	-1
82	CDKL5	-1
83	CHEK1 (CHK1)	-2
84	CHEK2 (CHK2)	0
85	CHUK (IKK alpha)	-3
86	CLK1	2
87	CLK2	5
88	CLK3	1
89	CLK4	20
90	CSF1R (FMS)	6
91	CSK	-1
92	CSNK1A1 (CK1 alpha 1)	2
93	CSNK1A1L	2
94	CSNK1D (CK1 delta)	3
95	CSNK1E (CK1 epsilon)	2
96	CSNK1G1 (CK1 gamma 1)	-1
97	CSNK1G2 (CK1 gamma 2)	2
98	CSNK1G3 (CK1 gamma 3)	1
99	CSNK2A1 (CK2 alpha 1)	2
100	CSNK2A2 (CK2 alpha 2)	1
101	DAPK1	-1
102	DAPK2	4
103	DAPK3 (ZIPK)	1
104	DCAMKL1 (DCLK1)	-3
105	DCAMKL2 (DCK2)	-2
106	DDR1	37
107	DDR2	7
108	DMPK	0
109	DNA-PK	4
110	DYRK1A	2
111	DYRK1B	2
112	DYRK2	3
113	DYRK3	3
114	DYRK4	-3
115	EEF2K	1
116	EGFR (ErbB1)	96
117	EIF2AK2 (PKR)	20
118	EPHA1	14
119	EPHA2	4
120	EPHA3	1
121	EPHA4	5
122	EPHA5	4
123	EPHA6	54
124	EPHA7	20
125	EPHA8	8
126	EPHB1	5
127	EPHB2	29
128	EPHB3	0
129	EPHB4	26
130	ERBB2 (HER2)	40
131	ERBB4 (HER4)	27
132	ERN1	-1
133	ERN2	-7
134	FER	2
135	FES (FPS)	4
136	FGFR1	2
137	FGFR2	4
138	FGFR3	-4
139	FGFR4	6
140	FGR	15
141	FLT1 (VEGFR1)	22
142	FLT3	24
143	FLT3 ITD	-2
144	FLT4 (VEGFR3)	-1
145	FRAP1 (mTOR)	1
146	FRK (PTK5)	2
147	FYN	1
148	FYN A	-2
149	GAK	50
150	GRK1	-2
151	GRK4	0
152	GRK5	-7
153	GRK6	0
154	GRK7	3
155	GSG2 (Haspin)	6
156	GSK3A (GSK3 alpha)	1
157	GSK3B (GSK3 beta)	0
158	HCK	5
159	HIPK1 (Myak)	2
160	HIPK2	6
161	HIPK3 (YAK1)	3
162	HIPK4	-2
163	HUNK	-3
164	ICK	2
165	IGF1R	2

#	Kinase	Compound 5 % Kinase Inhibition (1μM)
166	IKBKB (IKK beta)	2
167	IKBKE (IKK epsilon)	1
168	INSR	-7
169	INSRR (IRR)	4
170	IRAK1	-4
171	IRAK3	11
172	IRAK4	-1
173	ITK	10
174	JAK1	-2
175	JAK2	0
176	JAK2 JH1 JH2	-4
177	JAK3	1
178	KDR (VEGFR2)	9
179	KIT	3
180	KSR2	1
181	LATS2	-7
182	LCK	9
183	LIMK1	0
184	LIMK2	-2
185	LRRK2	-3
186	LRRK2 FL	-4
187	LTK (TYK1)	1
188	LYN A	29
189	LYN B	45
190	MAP2K1 (MEK1)	3
191	MAP2K1 (MEK1)	3
192	MAP2K2 (MEK2)	7
193	MAP2K2 (MEK2)	-1
194	MAP2K4 (MEK4)	-2
195	MAP2K5 (MEK5)	0
196	MAP2K6 (MKK6)	-4
197	MAP2K6 (MKK6)	-5
198	MAP3K10 (MLK2)	-1
199	MAP3K11 (MLK3)	-3
200	MAP3K14 (NIK)	-2
201	MAP3K19 (YSK4)	1
202	MAP3K2 (MEKK2)	-5
203	MAP3K3 (MEKK3)	-2
204	MAP3K5 (ASK1)	-4
205	MAP3K7/MAP3K7IP1 (TAK1-TAB1)	-5
206	MAP3K8 (COT)	6
207	MAP3K9 (MLK1)	-3
208	MAP4K1 (HPK1)	3
209	MAP4K2 (GCK)	3
210	MAP4K3 (GLK)	-5
211	MAP4K4 (HGK)	9
212	MAP4K5 (KHS1)	7
213	MAPK1 (ERK2)	2
214	MAPK10 (JNK3)	6
215	MAPK10 (JNK3)	5
216	MAPK11 (p38 beta)	5
217	MAPK12 (p38 gamma)	3
218	MAPK13 (p38 delta)	1
219	MAPK14 (p38 alpha)	6
220	MAPK14 (p38 alpha) Direct	5
221	MAPK15 (ERK7)	0
222	MAPK3 (ERK1)	-1
223	MAPK7 (ERK5)	1
224	MAPK8 (JNK1)	13
225	MAPK8 (JNK1)	2
226	MAPK9 (JNK2)	8
227	MAPK9 (JNK2)	2
228	MAPKAPK2	2
229	MAPKAPK3	-2
230	MAPKAPK5 (PRAK)	0
231	MARK1 (MARK)	1
232	MARK2	0
233	MARK3	3
234	MARK4	-2
235	MASTL	-1
236	MATK (HYL)	1
237	MELK	2
238	MERTK (cMER)	-4
239	MET (cMet)	1
240	MINK1	9
241	MKNK1 (MNK1)	-4
242	MKNK2 (MNK2)	10
243	MLCK (MLCK2)	1
244	MLK4	-1
245	MST1R (RON)	-4
246	MST4	2
247	MUSK	-10
248	MYLK (MLCK)	-1
249	MYLK2 (skMLCK)	-2
250	MYLK4	4
251	MYO3A (MYO3 alpha)	-2
252	MYO3B (MYO3 beta)	-2

#	Kinase	Compound 5 % Kinase Inhibition (1μM)
253	NEK1	-1
254	NEK2	2
255	NEK4	0
256	NEK6	1
257	NEK8	-6
258	NEK9	-2
259	NIM1K	2
260	NLK	0
261	NTRK1 (TRKA)	14
262	NTRK2 (TRKB)	7
263	NTRK3 (TRKC)	11
264	NUAK1 (ARK5)	-7
265	NUAK2	-9
266	PAK1	-2
267	PAK2 (PAK65)	2
268	PAK3	-3
269	PAK4	0
270	PAK6	8
271	PAK7 (KIAA1264)	3
272	PASK	-1
273	PDGFRA (PDGFR alpha)	0
274	PDGFRB (PDGFR beta)	-2
275	PDK1	3
276	PDK1 Direct	-2
277	PEAK1	7
278	PHKG1	8
279	PHKG2	3
280	PI4K2A (PI4K2 alpha)	5
281	PI4K2B (PI4K2 beta)	2
282	PI4KA (PI4K alpha)	1
283	PI4KB (PI4K beta)	8
284	PIK3C2A (PI3K-C2 alpha)	7
285	PIK3C2B (PI3K-C2 beta)	5
286	PIK3C2G (PI3K-C2 gamma)	22
287	PIK3C3 (hVPS34)	-3
288	PIK3CA/PIK3R1 (p110 alpha/p85 alpha)	34
289	PIK3CA/PIK3R3 (p110 alpha/p55 gamma)	10
290	PIK3CB/PIK3R1 (p110 beta/p85 alpha)	-3
291	PIK3CB/PIK3R2 (p110 beta/p85 beta)	-2
292	PIK3CD/PIK3R1 (p110 delta/p85 alpha)	4
293	PIK3CG (p110 gamma)	40
294	PIM1	2
295	PIM2	2
296	PIM3	-1
297	PIP4K2A	-18
298	PIP5K1A	-2
299	PIP5K1B	-6
300	PIP5K1C	-1
301	PKMYT1	2
302	PKN1 (PRK1)	1
303	PKN2 (PRK2)	2
304	PLK1	0
305	PLK2	2
306	PLK3	-7
307	PLK4	-3
308	PRKACA (PKA)	-1
309	PRKACB (PRKAC beta)	-8
310	PRKACG (PRKAC gamma)	-1
311	PRKCA (PKC alpha)	-8
312	PRKCB1 (PKC beta I)	5
313	PRKCB2 (PKC beta II)	21
314	PRKCD (PKC delta)	-3
315	PRKCE (PKC epsilon)	11
316	PRKCG (PKC gamma)	12
317	PRKCH (PKC eta)	-2
318	PRKCI (PKC iota)	15
319	PRKCN (PKD3)	6
320	PRKCQ (PKC theta)	14
321	PRKCZ (PKC zeta)	8
322	PRKD1 (PKC mu)	5
323	PRKD2 (PKD2)	0
324	PRKG1	0
325	PRKG2 (PKG2)	-3
326	PRKX	9
327	PTK2 (FAK)	0
328	PTK2B (FAK2)	3
329	PTK6 (Brk)	9
330	RET	8
331	RIPK2	67
332	RIPK3	75
333	ROCK1	1
334	ROCK2	0
335	ROS1	7

#	Kinase	Compound 5 % Kinase Inhibition (1μM)
336	RPS6KA1 (RSK1)	3
337	RPS6KA2 (RSK3)	1
338	RPS6KA3 (RSK2)	1
339	RPS6KA4 (MSK2)	-2
340	RPS6KA5 (MSK1)	-3
341	RPS6KA6 (RSK4)	-2
342	RPS6KB1 (p70S6K)	6
343	RPS6KB2 (p70S6Kb)	3
344	SBK1	12
345	SGK (SGK1)	2
346	SGK2	3
347	SGKL (SGK3)	4
348	SIK1	0
349	SIK3	2
350	SLK	4
351	SNF1LK2	5
352	SPHK1	-3
353	SPHK2	-8
354	SRC	6
355	SRC N1	4
356	SRMS (Srm)	6
357	SRPK1	-2
358	SRPK2	3
359	STK16 (PKL12)	-2
360	STK17A (DRAK1)	65
361	STK17B (DRAK2)	12
362	STK22B (TSSK2)	3
363	STK22D (TSSK1)	0
364	STK23 (MSSK1)	-2
365	STK24 (MST3)	2
366	STK25 (YSK1)	-1
367	STK3 (MST2)	-1
368	STK32B (YANK2)	0
369	STK32C (YANK3)	-2
370	STK33	1
371	STK38 (NDR)	-2
372	STK38L (NDR2)	12
373	STK39 (STLK3)	5
374	STK4 (MST1)	-1
375	SYK	-2
376	TAOK1	-3
377	TAOK2 (TAO1)	-3
378	TAOK3 (JIK)	-1
379	TBK1	0
380	TEC	-3
381	TEK (Tie2)	-8
382	TESK1	3
383	TESK2	-3
384	TGFBR1 (ALK5)	-3
385	TGFBR2	28
386	TLK1	-11
387	TLK2	-6
388	TNIK	6
389	TNK1	4
390	TNK2 (ACK)	0
391	TTK	-4
392	TXK	5
393	TYK2	5
394	TYRO3 (RSE)	1
395	ULK1	0
396	ULK2	-3
397	ULK3	0
398	VRK2	5
399	WEE1	3
400	WNK1	-3
401	WNK2	1
402	WNK3	-2
403	YES1	10
404	ZAK	-2
405	ZAP70	1
406	EGFR (ErbB1) C797S	88
407	EGFR (ErbB1) d746-750	100
408	EGFR (ErbB1) d747-749 A750P	103
409	EGFR (ErbB1) G719C	88
410	EGFR (ErbB1) G719S	89
411	EGFR (ErbB1) L858R	93
412	EGFR (ErbB1) L861Q	96
413	EGFR (ErbB1) T790M	11
414	EGFR (ErbB1) T790M C797S L858R	8
415	EGFR (ErbB1) T790M L858R	8

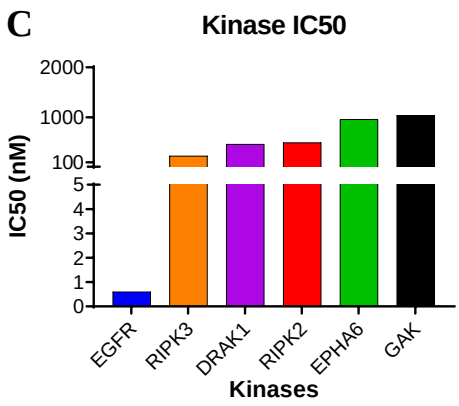

Figure S5. Kinome profiling of compound **5**. (A) TREEspot™ kinome profile of wild-type kinases (left) and mutant kinases (right) of compound **5**. The size of the circle refers to the percent of control of kinase activity remaining at a drug concentration of 1µM. Image generated using TREEspot™ Software Tool and reprinted with permission from KINOMEscan®, a division of DiscoveRx Corporation, © DISCOVERX CORPORATION 2010. (B) Tabular list of kinases tested and their percent kinase inhibition (Thermofisher). (C) IC_{50} determinations of the top wild-type kinase hits from the primary screen.

Chapter 1 – Figure S6

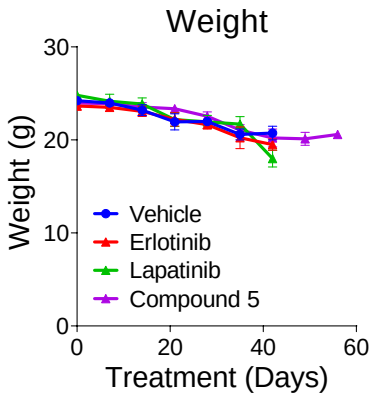

Figure S6. Mouse weights in orthotopic GBM39 xenograft mice treated with indicated EGFR inhibitors from survival study in Figure 2.

Chapter 1 – Figure S7

A

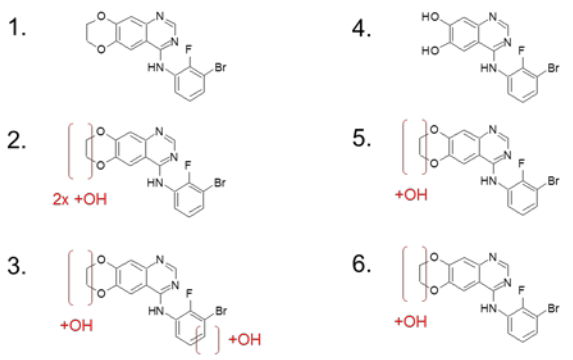

Modification	Mass	% of Total (mouse)	% of Total (human)
1. Parent	376	9.0%	33.0%
2. di-hydroxylation	408	8.7%	n.d.
3. di-hydroxylation	408	4.1%	3.2%
4. O-dealkylation	350	4.7%	n.d.
5. Hydroxylation	392	38.6%	43.3%
6. Hydroxylation	392	34.9%	19.8%

B

Property	Mouse Liver Microsome (mL/min/g)	Human Liver Microsome (mL/min/g)
in vitro clearance	37.5	30.9

Figure S7. Metabolism of compound **5** in mouse and human liver microsomes. (A) Compound **5** was incubated for 30 minutes with liver microsomes and profiled by LC-MS to determine metabolites. n.d., not detected. (B) in vitro clearance from mouse and human liver microsomes.

Chapter 1 – Figure S8

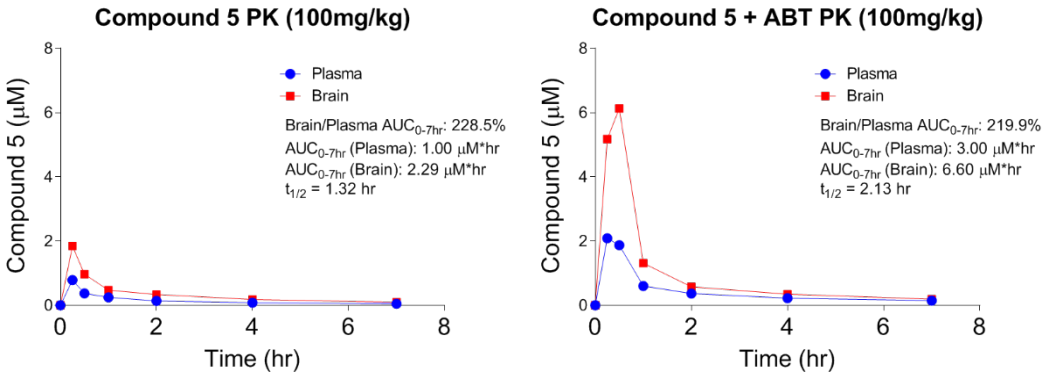

Figure S8. Oral pharmacokinetics of plasma and brain tissue from healthy CD-1 mice of compound **5** alone (A) and compound **5** combined with 1-aminobenzotriazole (ABT) (B).

Chapter 1 – Figure S9

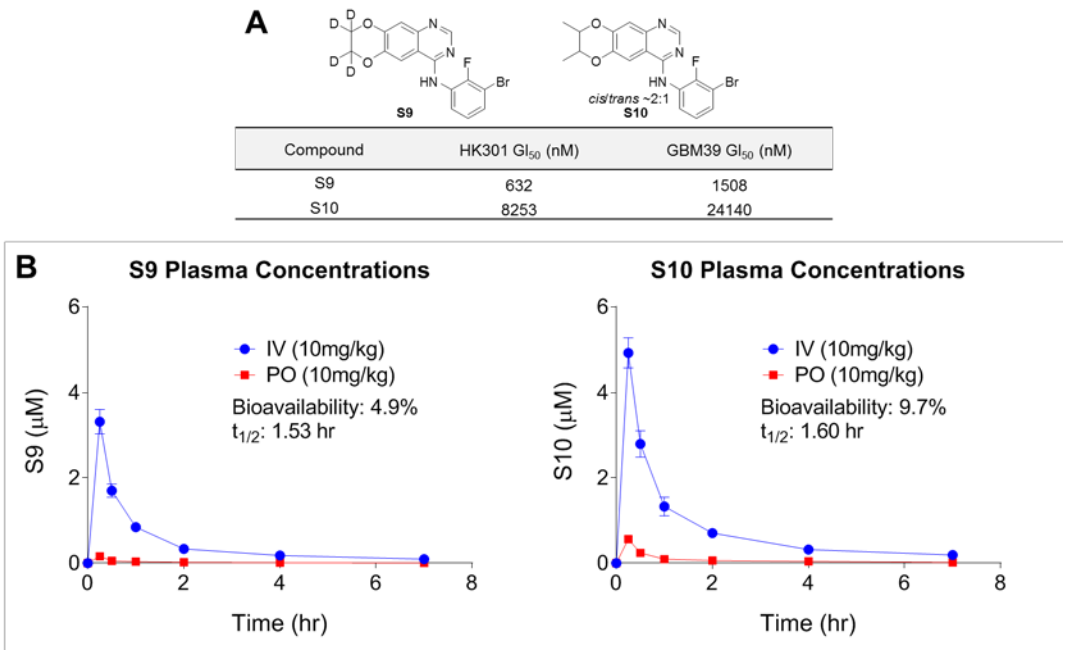

Compound	HK301 GI_{50} (nM)	GBM39 GI_{50} (nM)
S9	632	1508
S10	8253	24140

Figure S9. Analogues with modified fused 1,4-dioxane ring for mitigating metabolic labile sites. (A) Structures and *in vitro* potency of **S9** and **S10**. (B) Bioavailability of **S9** and **S10**.

Chapter 1 – Figure S10

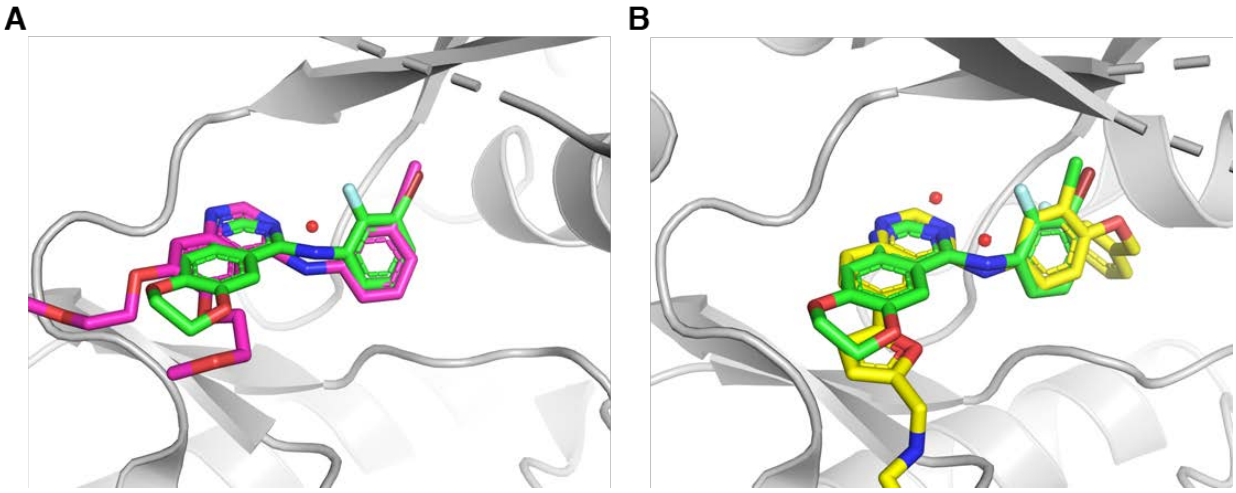

Figure S10. Overlays of compound **5** docked into the active site of wtEGFR together with the original ligand of the crystal structure: (A) erlotinib (PDB 1M17), (B) lapatinib (PDB 1XKK).[36] For both docking results, the quinazoline ring system is slightly tilted, and the aniline ring is slightly displaced compared to the ligand in the crystal structure. However, the observed close contact interactions with the protein are in line with the binding mode of the type I TKI scaffold. The P-loops have been removed for clarity. Color code: C_{enzyme} gray, C_5 green, $C_{erlotinib}$ purple, $C_{lapatinib}$ yellow, O red, N blue, F light blue, Cl green, Br dark red.

Chapter 1 – Table S5. Efflux ratios and K_{puu} of AZD3759, osimertinib, and compound **5**.

Compound	Concentration (µM)	Efflux Ratio (P-gp)	Efflux Ratio (BCRP)	$K_{p,uu,brain}$ (Mouse)
AZD3759	1	0.41[21]	0.64[21]	1.30[21]
AZD9291	1	13.4[9]	5.4[9]	0.39[9]
Compound **5**	10	0.58	0.30	1.30

Chapter 1 – Figure S11

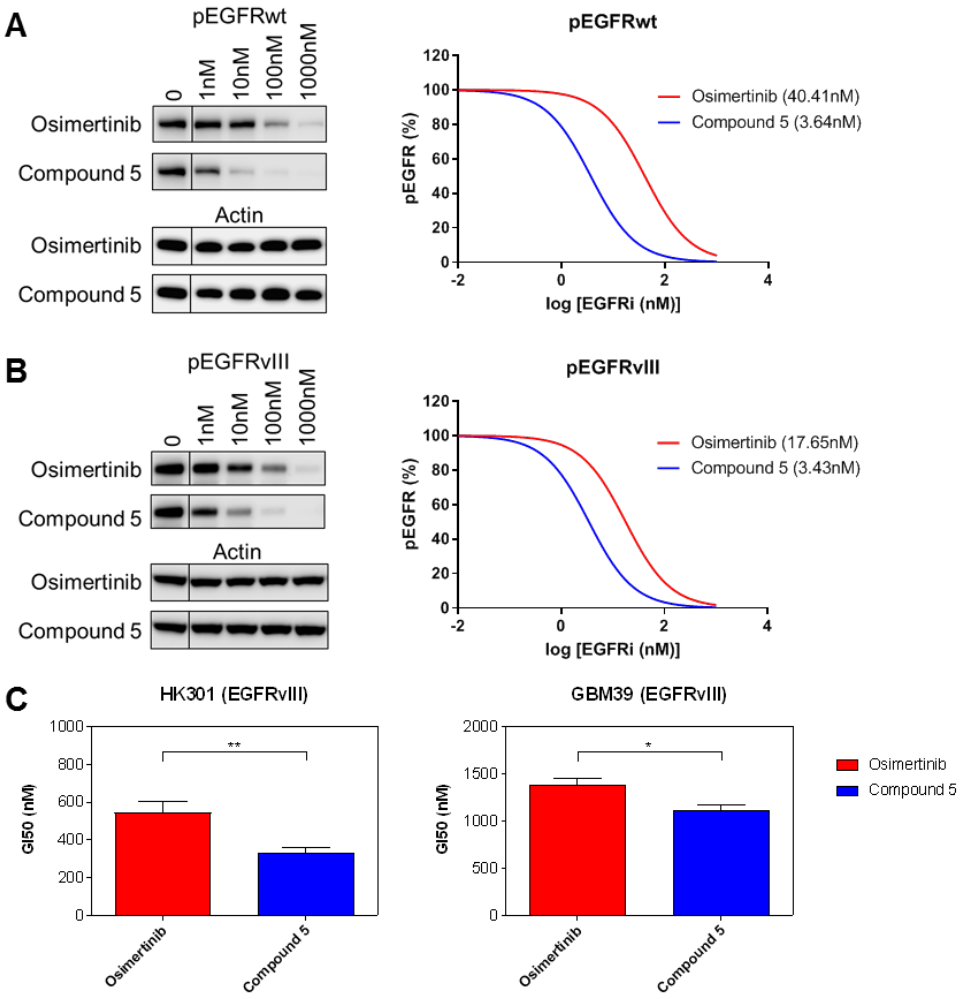

Figure S11. Potency comparisons of osimertinib and compound **5**. Compound **5** is more potent at inhibiting (A) EGF-stimulated wtEGFR and (B) EGFRvIII than osimertinib (C) Osimertinb and compound **5** GI_{50} show compound **5** more potently inhibits growth of EGFRvIII mutant HK301 and GBM39 patient-derived lines. * $p<0.05$, ** $p<0.01$, *** $p<0.001$.

Chapter 1 – Figure S12

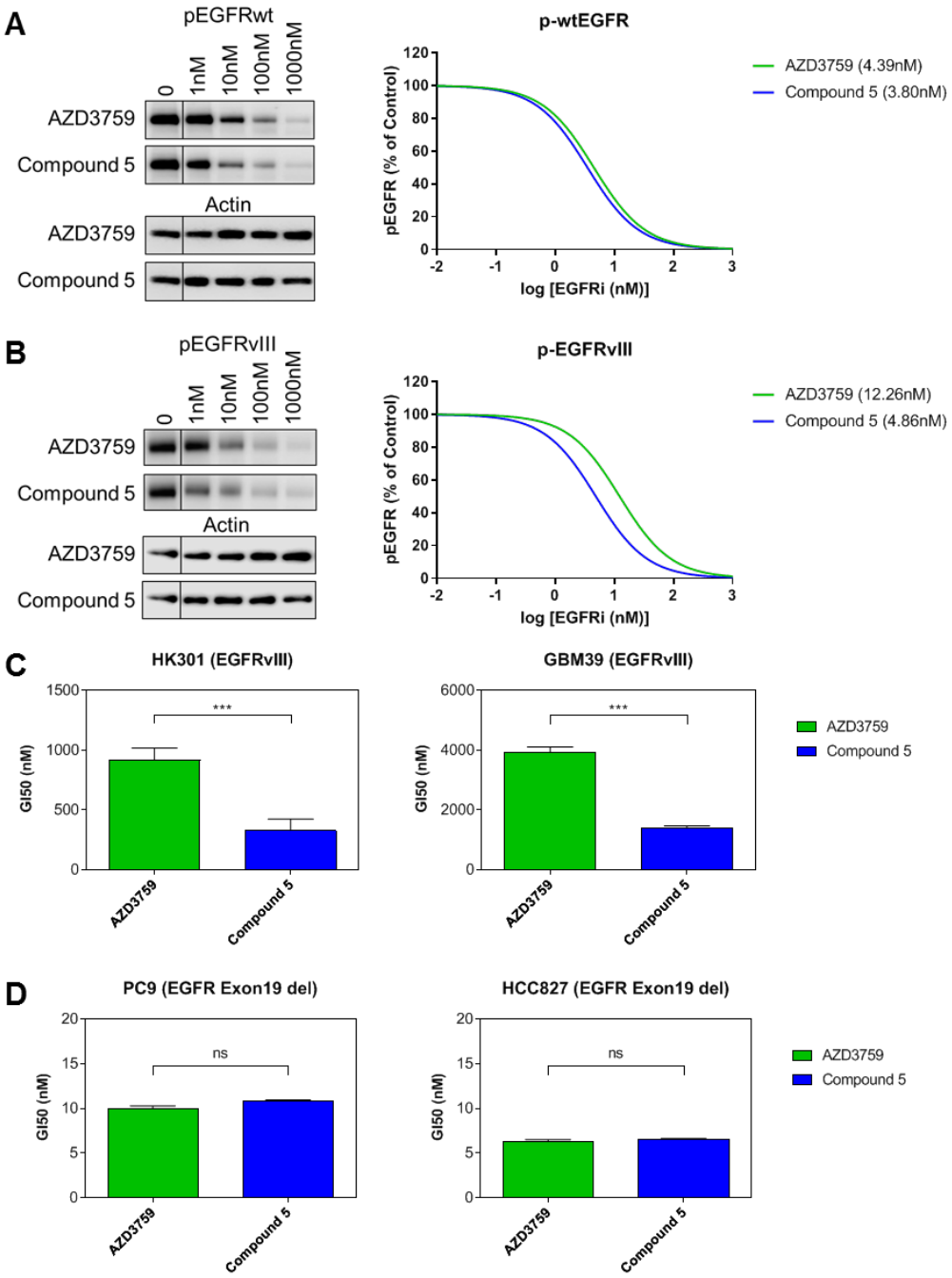

Figure S12. Potency comparisons of AZD3759 and compound **5**. Compound **5** is equally potent at inhibiting EGF-stimulated wtEGFR (A) but is more potent at inhibiting EGFRvIII (B) compared with AZD3759. (C) AZD3759 and compound **5** GI_{50} show compound **5** more potently inhibits growth of EGFRvIII mutant HK301 and GBM39 patient-derived cell lines. (D) AZD3759 and compound **5** equally inhibit growth of Exon 19 EGFR-mutant PC9 and HCC827 lung cancer lines. * $p<0.05$, ** $p<0.01$, *** $p<0.001$.

Chapter 1 – Figure S13

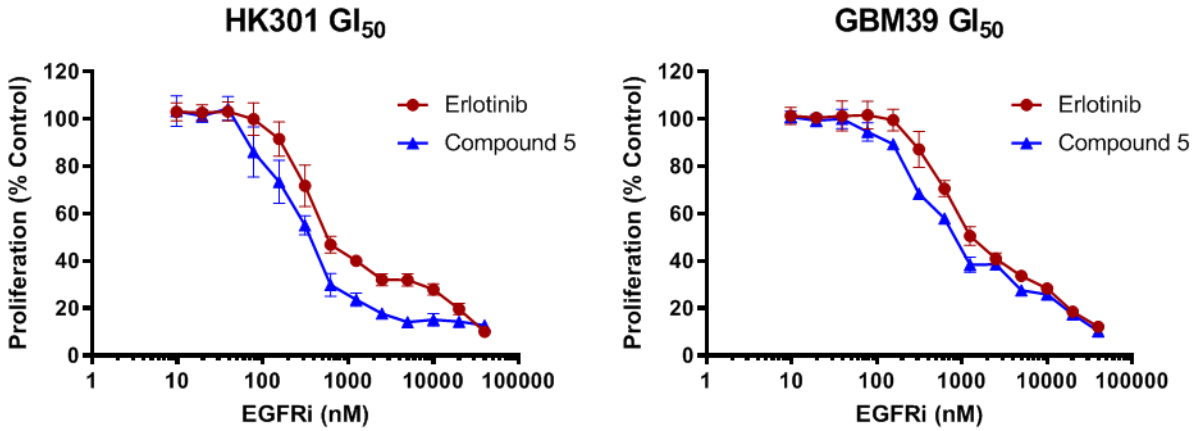

Figure S13. GI50s of erlotinib and Compound **5** against patient-derived EGFRvIII mutant GBM cell lines indicate no paradoxical increase in growth was observed at any concentration of the tested EGFR TKI.

Chapter 1 – Table S6. Crystal data, data collection, and structure refinement for 4 (CCDC-1913486).

Crystal data	
Empirical formula	$C_{16}H_{11}ClFN_3O_2$
Formula weight (M_r)	331.73
Crystal system, space group	Orthorhombic, *Pna*2$_1$
Temperature	100(2) K
Unit cell dimensions	a = 12.4287 (19) Å
	b = 16.933 (3) Å
	c = 6.578 (1) Å
Volume	1384.3 (4) Å^3
Z	4
Radiation type	Cu$K\alpha$ radiation, λ = 1.54178 Å
Crystal size (mm)	0.20 × 0.10 × 0.04 mm^3
Density (calculated)	1.592 mg mm^{-3}
Absorption coefficient μ	2.690 mm^{-1}
F(000)	680
Data collection	
Diffractometer	Bruker APEX-II CCD
Theta range for data collection	4.4 to 69.9°
Index ranges	$-15 \le h \le 14$, $-20 \le k \le 20$, $-7 \le l \le 7$
Reflections collected	8518
Independent reflections	2385 (R_{int} = 0.041)
Absorption correction	multi-scan
Max. and min. transmission	0.75 and 0.63
Refinement	
Refinement method	Full-matrix least-squares on F^2
Data / restraints / parameters	2385 / 1 / 211
Goodness-of-fit on F^2	1.100
Final R indices [$I > 2\sigma(I)$]	R_1 = 0.0254, wR_2 = 0.0619
R indices (all data)	R_1 = 0.0263, wR_2 = 0.0625
Largest diff. peak and hole	0.19 and –0.24 eÅ^{-3}

Chapter 1 – Figure S14

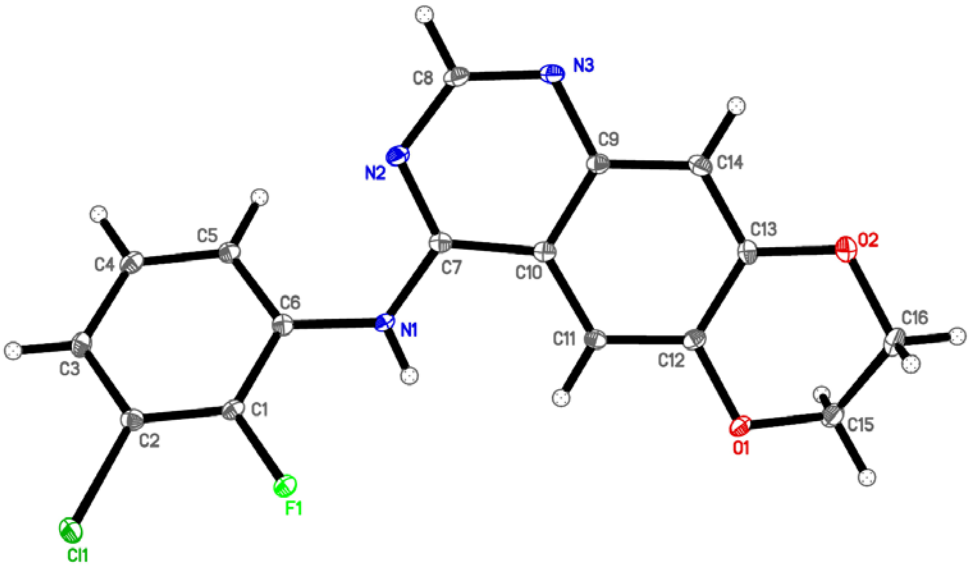

Figure S14. ORTEP representation of 4, arbitrary numbering. Atomic displacement parameters at 100 K are drawn at 50% probability level. Color code: grey = C, white = H, blue = N, red = O, pale green = F, dark green = Cl. Selected bond lengths (Å), and torsional angles (°): F1–C1 1.355(2), Cl1–C2 1.733(2), N1–C6 1.415(3), N1–C7 1.358(3), O1–C12 1.376(3), O2–C13 1.363(3), N2–C7–N1–C6 1.0(3), C5–C6–N1–C7 30.3(3).

Chapter 1 – Figure S15

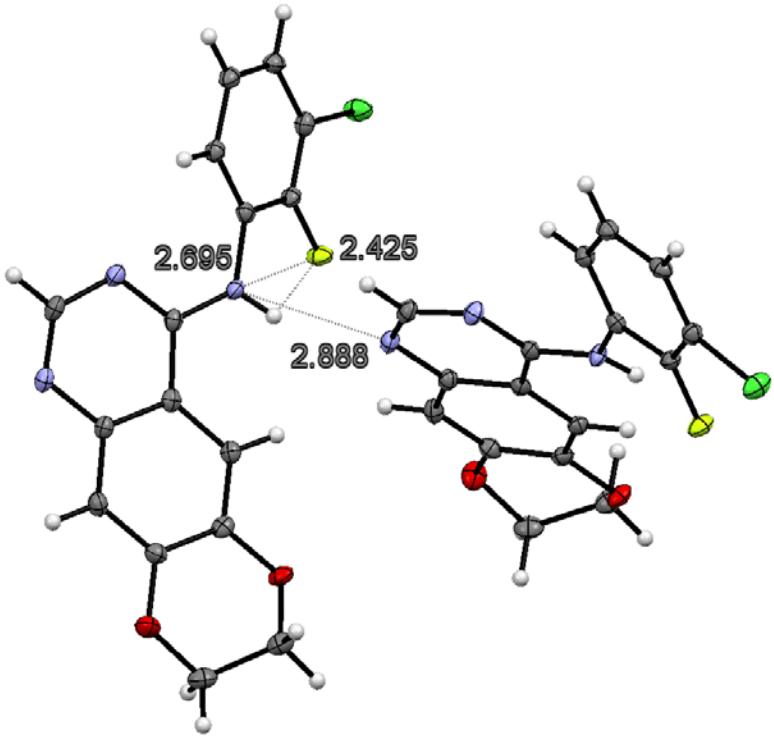

Figure S15. Distances of inter- and intramolecular hydrogen bonding interactions involving the N-H proton in the crystal packing of **4**. Distances (in Å) are shown as dashed grey lines.

Chapter 1 – Table S7. Crystal data, data collection, and structure refinement for 5 (CCDC-1913485).

Crystal data	
Empirical formula	$C_{16}H_{11}BrFN_3O_2$
Formula weight (M_r)	376.19
Crystal system, space group	Orthorhombic, $Pna2_1$
Temperature	100(2) K
Unit cell dimensions	a = 12.4531 (10) Å
	b = 17.0793 (13) Å
	c = 6.6267 (5) Å
Volume	1409.43 (19) Å^3
Z	4
Radiation type	Mo$K\alpha$ radiation, λ = 0.71073 Å
Crystal size (mm)	0.30 × 0.25 × 0.10 mm^3
Density (calculated)	1.773 mg mm^{-3}
Absorption coefficient μ	2.942 mm^{-1}
F(000)	752
Data collection	
Diffractometer	Bruker APEX-II CCD
Theta range for data collection	2.0 to 31.0°
Index ranges	$-17 \leq h \leq 17$, $-24 \leq k \leq 23$, $-9 \leq l \leq 9$
Reflections collected	17842
Independent reflections	4154
Absorption correction	multi-scan
Max. and min. transmission	0.74 and 0.57
Refinement	
Refinement method	Full-matrix least-squares on F^2
Data / restraints / parameters	4154 / 1 / 211
Goodness-of-fit on F^2	1.034
Final R indices [$I > 2\sigma(I)$]	R_1 = 0.0217, wR_2 = 0.0530
R indices (all data)	R_1 = 0.0239, wR_2 = 0.0537
Largest diff. peak and hole	0.41 and –0.42 eÅ^{-3}

Chapter 1 – Figure S16

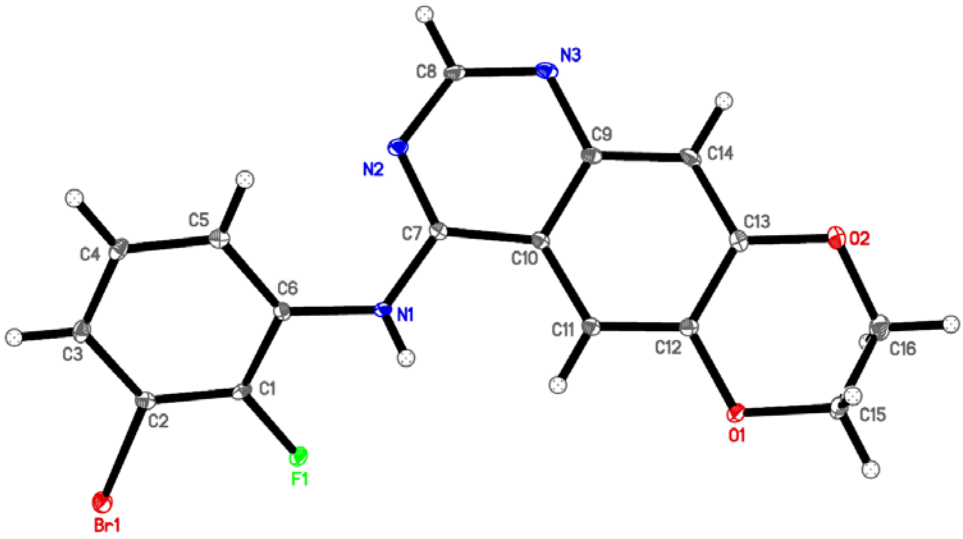

Figure S16. ORTEP representation of 5, arbitrary numbering. Atomic displacement parameters at 100 K are drawn at 50% probability level. Color code: grey = C, white = H, blue = N, red = O, pale green = F, dark green = Cl. Selected bond lengths (Å), and torsional angles (°): F1–C1 1.351(2), Br1–C2 1.883(2), N1–C6 1.409(3), N1–C7 1.362(3), O1–C12 1.371(2), O2–C13 1.371(3), N2–C7–N1–C6 –0.7(3), C5–C6–N1–C7 –30.9(3).

Chapter 1 – Figure S17

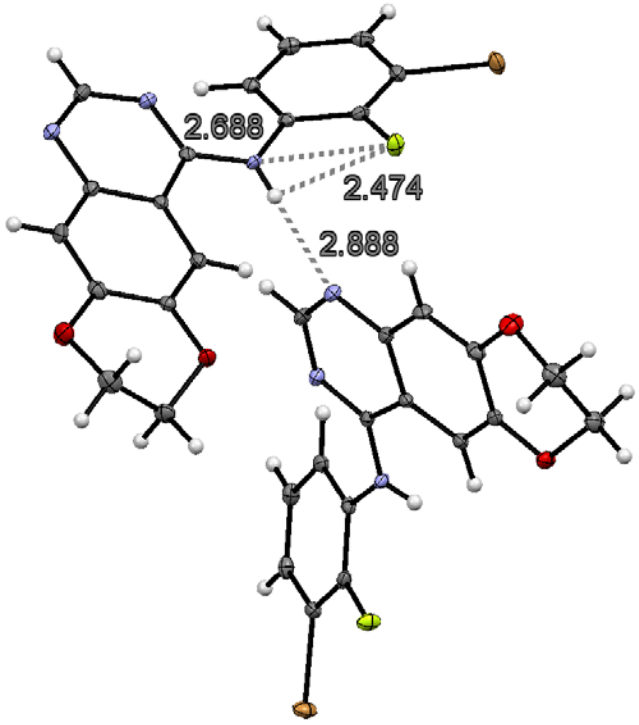

Figure S17. Distances of inter- and intramolecular hydrogen bonding interactions involving the N-H proton in the crystal packing of **5**. Distances (in Å) are shown as dashed grey lines.

SYNTHESIS SCHEMES

Chapter 1 – Scheme S1

Synthesis of halogenated anilines:

Scheme S1 shows the preparation of the halogenated anilines **S11–S15**, which were used in the reaction with the chloroquinazoline **24** for the synthesis of the final compounds **2**, and **13**–**16**. 2-Amino-6-bromophenol was prepared as described in [42].

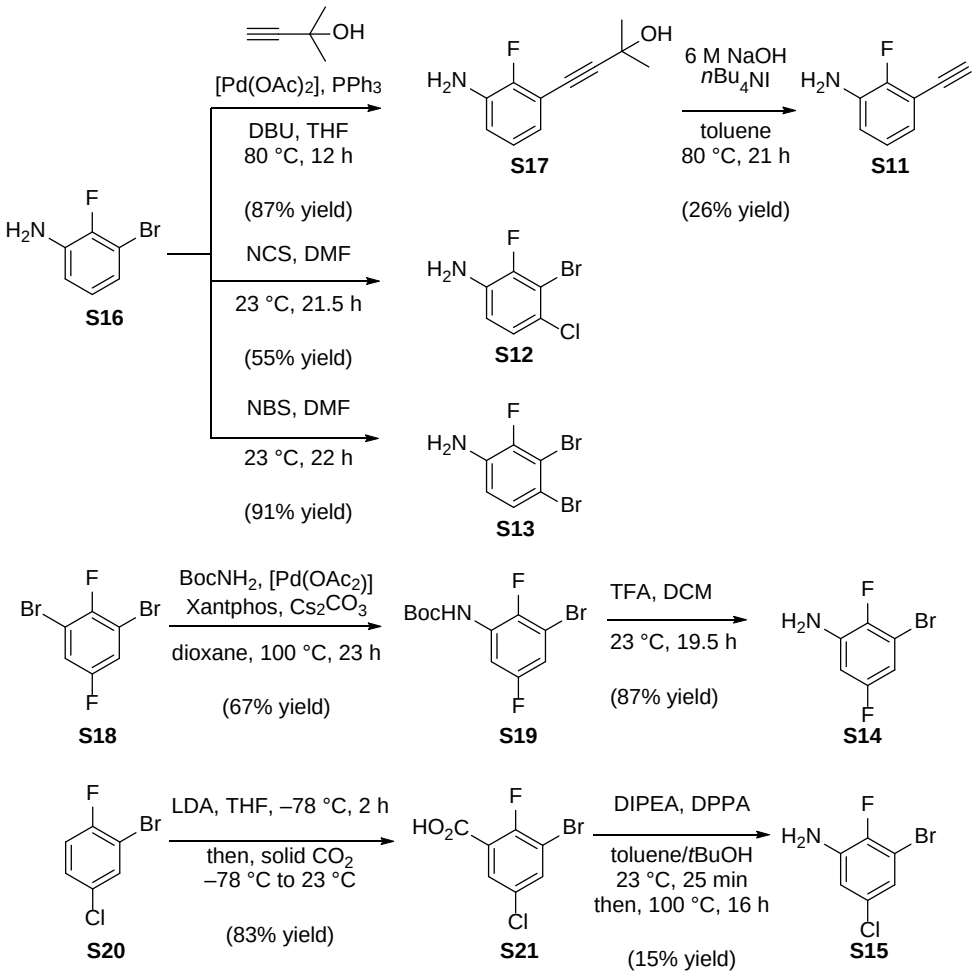

Scheme S1. Synthesis of the halogenated anilines S11–S15.

Chapter 1 – Scheme S2

Short route to compound **5**:

Alkylation of 3,4-dihydroxybenzonitrile (**S22)** with 1-bromo-2-chloroethane gave benzodioxanecarbonitrile **S23** in good yield and sufficient purity to directly continue with its nitration to **S24**, which was purified by recrystallization. Hydrogenation of **S24** afforded the anthranilonitrile **S25**, which was subjected to the usual conditions for the quinazoline synthesis by the Dimroth rearrangement to obtain **5**.

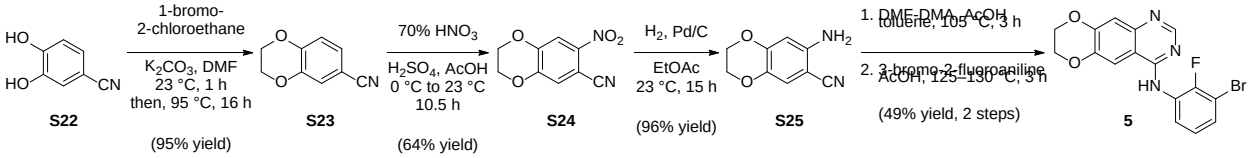

Scheme S2. Short synthetic route to compound **5**.

Chapter 1 – Scheme S3

Synthesis of perdeuterated (**S9**) and vic-dimethyl (**S10**) substituted analogues of compound **5**:

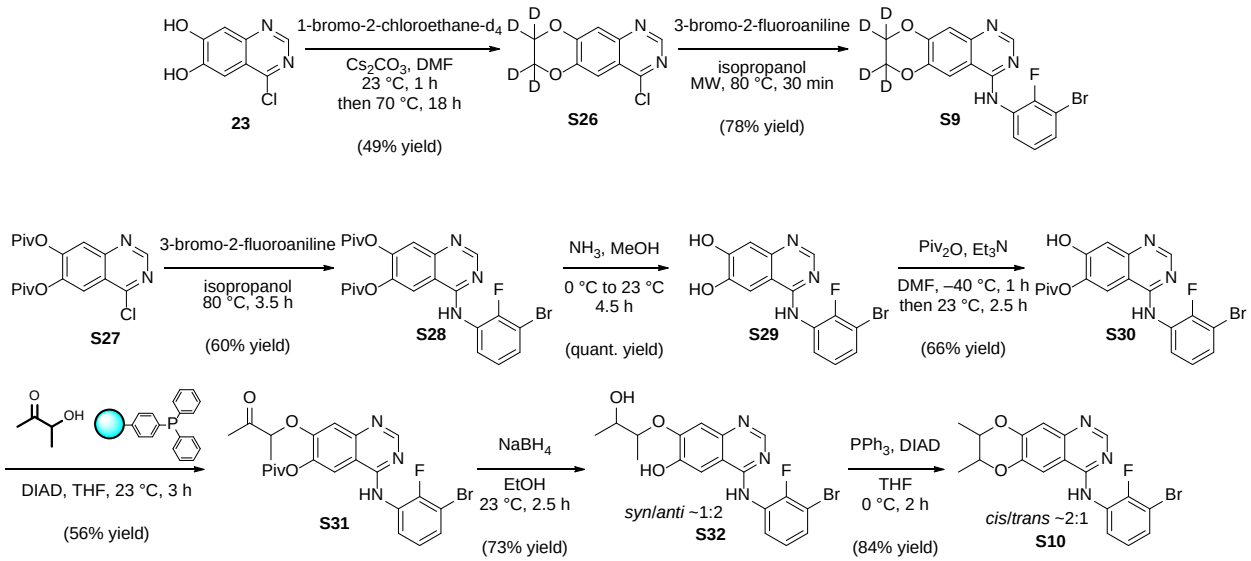

Scheme S3. Synthesis of analogues **S9** and **S10** with a modified fused-1,4-dioxane ring for improved metabolic stability.

EXPERIMENTAL METHODS

Cell culture conditions. Patient-derived GBM cells were cultured in serum-free gliomasphere conditions consisting of DMEM/F12 (Thermofisher), B27 (Thermofisher), Penicillin-Streptomycin (100U/mL penicillin, 100mg/mL streptomycin, Thermofisher), and Glutamax (Thermofisher) supplemented with Heparin (5μg/mL, Sigma), Human EGF (50ng/mL, Thermofisher), and Human FGF-β (20ng/mL, Thermofisher). U87 cells were cultured in DMEM (Thermofisher), FBS (10%, Gemini Bio-Products), Penicillin-Streptomycin, and Glutamax. Cells were dissociated to single cell suspensions with TrypLE (Thermofisher) and resuspended in its respective media. Cell lines were regularly tested for mycoplasma infection using Myco Alert™ Mycoplasma Detection Kit according to the manufacturer's protocol (Lonza).

Reagents and antibodies. The following chemical inhibitors were dissolved in DMSO for all in vitro studies: Erlotinib (Chemietek), Lapatinib (MedChemExpress). The following antibodies for immunoblotting were obtained from the listed sources: p-EGFR Y1086 (Thermofisher, 36-9700), t-EGFR (Millipore, 06-847), p-AKT T308 (Cell Signaling, 13038), p-AKT S473 (Cell Signaling, 4060), t-AKT (Cell Signaling, 4685), p-ERK T202/Y204 (Cell Signaling, 4370), t-ERK (Cell Signaling, 4695), p-S6 S235/236 (Cell Signaling, 4858), t-S6 (Cell Signaling, 2217), β-Actin (Cell Signaling, 3700).

Cell-free kinase assays. Cell-free EGFR kinase assays were performed using the EGFR Kinase Enzyme System (Promega, V9261). Briefly, 25 ng of recombinant EGFR kinase domain was incubated at RT with 10 μM ATP, 1 μg/μL poly (4:1 Glu, Tyr) peptide substrate, and an EGFR inhibitor in a 384-well plate for 40 min. Equal volume of ADP-Glo™ Reagent was then added and

incubated for 40 min followed by the addition of the Kinase Detection Reagent and a final 30 min incubation. Luminescence (integration time 1 sec) was recorded on a CLARIOstar microplate reader (BMG Labtech). A 10-point titration curve of each EGFR inhibitor was performed in duplicate.

Cell based IC_{50}. U87-wtEGFR and U87-EGFRvIII cells were acclimated overnight in standard cell culture conditions. Cells were washed with PBS and cultured overnight in serum-free DMEM (Thermofisher), Penicillin-Streptomycin, and Glutamax. U87-wtEGFR cells were stimulated with Heparin (5µg/mL, Sigma), Human EGF (50ng/mL, Thermofisher) for 1 hr followed by EGFR TKI treatment for 1 hr before being collected. U87-EGFRvIII cells were treated with EGFR TKI for 1 hr before being collected.

Immunoblotting. Cells were collected and lysed in RIPA buffer (Boston BioProducts) containing Halt™ Protease and Phosphatase Inhibitor (Thermofisher). Lysates were centrifuged at 14,000g for 15min at 4°C. Protein samples were then boiled in NuPAGE LDS Sample Buffer (Thermofisher) and NuPAGE Sample Reducing Agent (Thermofisher), separated using SDS-PAGE on 12% Bis-Tris gels (Thermofisher), and transferred to nitrocellulose membrane (GE Healthcare). Immunoblotting was performed per antibody's manufacturer's specifications. Membranes were developed using the SuperSignal™ system (Thermofisher) and imaged using the Odyssey Fc Imaging System (LI-COR). Signal quantification was performed using the Image Studio™ software (LI-COR).

Growth inhibition assays. Growth inhibition assays were performed by incubating 1500 cells per well in 384-well plates for 72 hours with EGFR inhibitor. A 14-point titration curve of each EGFR inhibitor was performed in quadruplicate. All growth inhibition assays were independently repeated at least 3 times. Cell Titer Glo Luminescent Cell Viability Assay (Promega) was used to measure growth inhibition from control of each EGFR inhibitor. Luminescence (integration time 1 sec) was recorded on a CLARIOstar microplate reader (BMG Labtech).

Proliferation assays. Cells were plated at 50,000 cells/mL with EGFR inhibitors and were dissociated to single cell suspensions every 3 days. Cells were replated and EGFR inhibitors were refreshed. At day 9, cell numbers were recorded and compared to vehicle treated cells. Proliferation assays were independently repeated 3 times.

Permeability assays. Permeability assays were performed by Charles River using a confluent monolayer of Madin Darby Canine Kidney (MDCK) epithelial cells stably transfected with the human *MDR1* gene (gene encoding P-gp). For the apical to basolateral (A→B) permeability, the EGFR inhibitors in the presence or absence of 50 μM verapamil (a P-gp inhibitor) was added to the apical side and permeation was measured from the basolateral side after a 2 hr incubation; the converse was applied for the basolateral to apical (B→A) permeability. The EGFR inhibitors in the supernatant of the apical and basolateral sides were analyzed by LC-MS/MS to determine permeability and efflux ratios.

Pharmacokinetic studies. Male CD-1 mice were treated by oral gavage with 10 mg/kg of EGFR inhibitor. Mice were euthanized and whole blood and brain tissue were collected at 0, 0.25, 0.5, 1,

2, 4, and 7 hrs post treatment (n=2 mice per time point). Whole blood from mice was centrifuged to isolate plasma. EGFR inhibitors were isolated by liquid-liquid extraction from plasma: 50 µL plasma was added to 150 µL acetonitrile and 5 pmol gefitinib internal standard. Mouse brain tissue was washed with 2 mL cold PBS and homogenized using a tissue homogenizer in 2 mL cold water. EGFR inhibitors were then isolated and reconstituted in a similar manner by liquid-liquid extraction: 100 µL brain homogenate was added to 5 pmol gefitinib internal standard and 300 µL acetonitrile. After vortex mixing, the samples were centrifuged. The supernatant was removed and evaporated by a rotary evaporator and reconstituted in 100 µL 50:50:0.1 water:acetonitrile:formic acid.

EGFR inhibitor detection. Chromatographic separations were performed on a 100 x 2.1 mm Phenomenex Kinetex C18 column (Kinetex) using the 1290 Infinity LC system (Agilent). The mobile phase was composed of solvent A: 0.1% formic acid in Milli-Q water, and B: 0.1% formic acid in acetonitrile. Analytes were eluted with a gradient of 5% B (0-4 min), 5-99% B (4-32 min), 99% B (32-36 min), and then returned to 5% B for 12 min to re-equilibrate between injections. Injections of 20 µL into the chromatographic system were used with a solvent flow rate of 0.10 mL/min. Mass spectrometry was performed on the 6460 triple quadrupole LC/MS system (Agilent). Ionization was achieved by using electrospray in the positive mode and data acquisition was made in multiple reactions monitoring (MRM) mode. Analyte signal was normalized to the internal standard and concentrations were determined by extrapolating on to the calibration curve (10, 100, 1000, 4000 nM). EGFR inhibitor brain concentrations were adjusted by 1.4% of the mouse brain weight for the residual blood in the brain vasculature as described previously.[43]

Genetic manipulation. Lentiviruses used for genetic manipulation were produced by transfecting 293-FT cells (ATCC) using lipofectamine 2000 (Thermofisher). Viruses were collected following 48 hr after transfection. Lentiviral vector backbones for the overexpression of wtEGFR and EGFRvIII in U87 cells contained a CMV promoter. U87-wEGFR and U87-EGFRvIII cells were generated by transfection with these overexpression vectors. Short hairpin RNAs (shRNAs) against EGFR were purchased from Sigma (shEGFR1: TRCN0000295969, shEGFR2: TRCN0000010329). For in vivo tumors, GBM gliomaspheres were infected with a lentiviral vector containing Gaussia luciferase (Gluc) reporter gene.

Intracranial Gaussia luciferase measurements. To measure the levels of Gluc, 6 µL of blood was collected from the tail vein of the mice and immediately mixed with 50mM EDTA to prevent coagulation. Gluc activity was obtained by measuring chemiluminescence following injection of 100 µL of 100uM coelenterazine (Nanolight) in a 96 well plate as described previously.[44]

Ex vivo immunoblot studies. GBM39 cells were injected (3×10^5 cells per injection) into the right basal ganglia of the brain (2mm lateral and 1mm anterior to bregma) of NSG mice (Radiation Oncology, UCLA). When the tumors were engrafted and began an exponential growth phase by gaussia luciferase measurement as described above, mice were randomized into treatments arms and were treated with either vehicle (5% DMSO, 10% Transcutol, 30% PEG400), erlotinib (10 mg/kg), lapatinib (80 mg/kg), or **13** (300 mg/kg, BID) for 3 consecutive days. Mice were then euthanized, and tumors were isolated by macro dissection with GFP fluorescence. Tumors were lysed by sonication in RIPA buffer (Boston BioProducts) containing Halt™ Protease and

Phosphatase Inhibitor (Thermofisher). The immunoblotting protocol above was then performed on lysates.

Intracranial mouse treatment studies. GBM39 cells were intracranially injected as described above NSG mice. When the tumors were engrafted and began an exponential growth phase by gaussia luciferase measurement as described above, mice were randomized into treatments arms and initiated treatment by oral gavage with either vehicle, erlotinib (10 mg/kg), lapatinib (80 mg/kg), or **13** (300 mg/kg, BID). Mice were treated for 5 days followed by 2 days of no treatment each week until endpoints were reached. Mice were euthanized when moribund or reached a 25% loss in body weight. All studies were in accordance with UCLA Animal Research Committee protocol guidelines.

Statistical Analyses. Unless otherwise specified, student's t-tests were performed for statistical analyses and p-values <0.05 were considered significant. All statistical analyses were calculated using GraphPad Prism.

Molecular Docking of Compound 5 into the EGFR Kinase Domain. The active and inactive wtEGFR protein structures used for the docking studies were retrieved from the RCSB Protein Data Bank (rcsb.org)[45] (PDB IDs: 1M17[18] (active) and 1XKK[36] (inactive)). The receptor protein structures were prepared as follows: 1) all crystallographic water molecules were removed, except for one water molecule making a direct hydrogen bonding interaction with N3 of the quinazoline; 2) hydrogen atoms were manually added to this water molecule with Schrödinger Maestro 2018-1; 3) in case of the protein structure derived from 1M17, Cys751 and Asp831 were manually

corrected with PyMOL 2.0.7 due to crystallographic disordering; 4) addition of polar hydrogen atoms, merging of non-polar hydrogen atoms and charges, and assignment of aromatic carbons were then carried out with AutoDockTools 4.2 (The Scripps Research Institute, La Jolla, California, USA).[46] The ligand coordinates were generated as follows: 1) for control docking experiments, the coordinates of erlotinib or lapatinib were retrieved from the protein crystal structure (PDB IDs 1M17 and 1XKK); 2) the coordinates of compound **5** were generated using a conformational search starting with the geometry of the X-ray crystal structure of **5**, performed with Schrödinger Maestro 2014-2 using MacroModel with the OPLS_2005 force field in water; these conformers were docked separately, and the results manually inspected; 3) all ligands were prepared for docking with AutoDockTools, which assigned Gasteiger charges and torsional angles to the ligand conformers. Docking was performed by AutoDock Vina 1.1.2 (The Scripps Research Institute)[47] with exhaustiveness set to 16; docking results were manually inspected, and the binding poses with the most favorable binding affinity and meaningful geometry were visualized with PyMOL.

Chemistry. *General.* Unless otherwise noted, all chemicals, reagents, and solvents were purchased from commercial sources when available and were used as received. When necessary, reagents and solvents were purified and dried by standard methods. Air- and moisture-sensitive reactions were carried out under an inert atmosphere of argon in oven-dried glassware. Microwave-irradiated reactions were carried out in a single mode reactor CEM Discover microwave synthesizer or with a Biotage Initiator+ system. Room temperature (RT) reactions were carried out at ambient temperature (approximately 23 °C). All reactions were monitored by thin layer chromatography (TLC) on precoated Merck 60 F_{254} silica gel plates with spots visualized by UV light (λ = 254, 365 nm), or colored by using a $KMnO_4$ solution. Flash column chromatography was carried out on SiO_2 60 (particle size 0.040–0.063 mm, 230–400 mesh). Preparative thin-layer chromatography (PTLC) was carried out with Merck 60 F_{254} silica gel plates (20 x 20 cm, 210–270 µm) or Analtech Silica Gel GF TLC plates (20 x 20 cm, 1000 µm). Concentration under reduced pressure (in vacuo) was performed by rotary evaporation typically at 25–35 °C. Purified compounds were further dried under high vacuum (HV) or in a desiccator. Yields correspond to purified compounds unless otherwise indicated, and were generally not further optimized. Proton nuclear magnetic resonance (^{1}H NMR) spectra were recorded on Bruker spectrometers (operating at 300, 400, or 500 MHz). Carbon NMR (^{13}C NMR) spectra were recorded on Bruker spectrometers (either at 400 or 500 MHz). NMR chemical shifts (δ ppm) were referenced to the residual solvent signals. ^{1}H NMR data are reported as follows: chemical shift in ppm; multiplicity (s = singlet, d = doublet, t = triplet, q = quartet, m = multiplet/complex pattern, dd = doublet of doublets, dt = doublet of triplets, td = triplet of doublets, ddd = doublet of doublet of doublets, tdd = triplet of doublet of doublets, br = broad signal); coupling constants (J) in Hz, integration. Data for ^{13}C NMR spectra are reported in terms of chemical shift, and if applicable coupling constants.

High resolution mass (HRMS) spectra were recorded on a Thermo Fisher Scientific Exactive Plus with IonSense ID-CUBE DART source mass spectrometer, or on a Waters LCT Premier mass spectrometer with ACQUITY UPLC with autosampler. All final compounds were purified to >95% purity as determined by HPLC (11 min). HPLC (11 min) methods used the following: Agilent 1260 Infinity LC system, Agilent Polaris C18-A 4.6 x 150 mm, 5 μm at 40 °C with a 0.8 mL/min flow rate; solvent A of 0.1% (v/v) formic acid in water, solvent B of 0.1% (v/v) in acetonitrile; 0.0–2.0 min, 5% B; 2.1–10.0 min, 5–95% B; 10.1–11 min, 95% B. Compounds were named according to the IUPAC nomenclature and numbering system following suggestions of ACD/ChemSketch from Advanced Chemistry Development, Inc.

General Procedures (GP). *GP-1: Nucleophilic Aromatic Substitution of 4-Chloroquinazoline with Anilines (Method A).* A mixture of the 4-chloroquinazoline **24** (1 equiv) in isopropanol (0.1–0.3 M) was treated with the aniline (1 equiv), and the mixture was heated at 80 °C under microwave irradiation for 15–20 min. The mixture was cooled to RT, treated with additional equiv of the aniline, and again subjected to microwave irradiation (80 °C, 15–20 min). (Alternatively, **24** (1 equiv) was treated with aniline (2 equiv) and heated in the microwave for 30 min under otherwise identical conditions). The mixture was either concentrated under reduced pressure, or the precipitated 4-anilinoquinazoline hydrochloride salt was isolated by filtration (washings with cold isopropanol). The residue was suspended in sat. aq. $NaHCO_3$, and extracted with CH_2Cl_2 (3x). The combined organic extracts were washed with water, brine, dried (Na_2SO_4), filtered, and concentrated. Purification by flash chromatography (elution with a gradient of CH_2Cl_2/EtOAc or hexanes/EtOAc) afforded the desired products typically as white to off-white, or pale-yellow solids.

GP-2: Nucleophilic Aromatic Substitution of 4-Chloroquinazoline with Anilines (Method B). A mixture of the 4-chloroquinazoline **24** (1 equiv) in acetonitrile (0.1–0.3 M) was treated with the aniline (2 equiv) and a 4 M solution of HCl in dioxane (1 equiv). The mixture was heated at 80 °C under microwave irradiation for 30 min. The mixture was either concentrated under reduced pressure, or the precipitated 4-anilinoquinazoline hydrochloride salt was isolated by filtration (washings with Et_2O). The residue was suspended in sat. aq. $NaHCO_3$, and extracted with CH_2Cl_2 (3x). The combined organic extracts were washed with water, brine, dried (Na_2SO_4), filtered, and concentrated. Purification by flash chromatography (elution with a gradient of CH_2Cl_2/EtOAc or hexanes/EtOAc) afforded the desired products typically as white to off-white, or pale-yellow solids.

GP-3: Nucleophilic Aromatic Substitution of 4-Chloroquinazoline with Anilines (Method C). A mixture of the 4-chloroquinazoline **24** (1 equiv) in anhydrous DMF (0.1 – 0.2 M) was treated with the aniline (2–3.5 equiv), and the mixture was stirred at 60 °C for 24 h. The mixture was cooled to RT, and diluted with water (30 mL) and EtOAc (30 mL). The organic layer was separated, and the aqueous layer was extracted with EtOAc (2 x 30 mL). The combined organic layers were washed successively with water and brine, dried ($MgSO_4$), filtered, and evaporated. Purification by flash chromatography (elution with a gradient of hexanes/EtOAc) afforded the desired products.

_N_-(3-Ethynylphenyl)-7,8-dihydro[1,4]dioxino[2,3-*g*]quinazolin-4-amine (1)

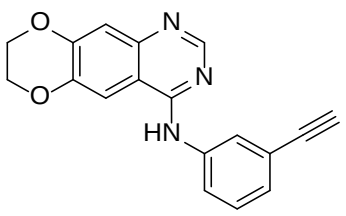

Following general procedure **GP-1**, compound **1** was prepared from the chloroquinazoline **24** (35 mg, 0.16 mmol) and 3-ethynylaniline (36 µL, 0.32 mmol) in isopropanol (1.5 mL). Flash chromatography (CH_2Cl_2/EtOAc 1:0 → 10:4) gave **1** (39 mg, 82%) as an off-white solid.

^{1}H NMR (500 MHz, DMSO-d_6): δ 9.49 (s, 1H), 8.47 (s, 1H), 8.11 – 8.06 (m, 1H), 8.08 (s, 1H), 7.95 – 7.90 (m, 1H), 7.38 (t, J = 7.9 Hz, 1H), 7.22 – 7.16 (m, 1H), 7.19 (s, 1H), 4.45 – 4.36 (m, 4H), 4.19 (s, 1H). ^{13}C NMR (126 MHz, DMSO-d_6): δ 156.39, 152.86, 149.13, 146.06, 143.65, 139.81, 128.87, 126.29, 124.46, 122.26, 121.70, 112.59, 109.99, 108.38, 83.57, 80.52, 64.50, 64.17. HRMS (DART): m/z $[M + H]^+$ calcd for $C_{18}H_{14}N_3O_2^+$, 304.1081; found, 304.1078.

***N*-(3-Ethynyl-2-fluorophenyl)-7,8-dihydro[1,4]dioxino[2,3-*g*]quinazolin-4-amine (2)**

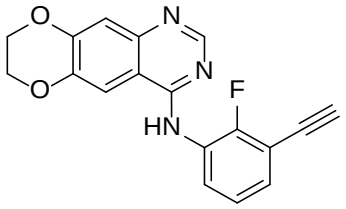

Preparation from the chloroquinazoline **24**: following general procedure **GP-1**, compound **2** was prepared from the chloroquinazoline **24** (35 mg, 0.16 mmol) and 3-ethynyl-2-fluoroaniline (**S11)** (42 mg, 0.31 mmol) in isopropanol (1.5 mL). After the reaction, the precipitated hydrochloride salt of **2** was converted into the free base by extraction of a sat. aq. $NaHCO_3$ solution to obtain pure **2** (34 mg, 67%) as an off-white solid.

Preparation from the quinazoline **4**: a 1 dram vial was charged with **4** (75 mg, 0.23 mmol), XPhos (19.7 mg, 0.041 mmol), Cs_2CO_3 (195 mg, 0.60 mmol), $[PdCl_2•(MeCN)_2]$ (3.6 mg, 0.014 mmol). The vial was evacuated and backfilled with argon (repeated at least twice). Dry acetonitrile (1 mL) was added, and the orange suspension was stirred at RT for 25 min, then ethynyltriethylsilane (150 µL, 0.84 mmol) was injected. The tube was sealed, and the reaction mixture stirred at 95 °C in a

preheated oil bath for 3.5 h. The suspension was allowed to reach 23 °C, diluted with EtOAc, filtered through a plug of SiO_2 (washings with EtOAc), and evaporated. Purification by flash chromatography (hexanes/EtOAc 8:2 → 4:6) afforded the triethylsilyl-protected compound **2** (48 mg, 49%) as a yellow foamy solid.

^{1}H NMR (500 MHz, $CDCl_3$): δ 8.681 (td, J = 8.1, 1.9 Hz, 1H), 8.678 (s, 1H), 7.382 (s, 1H), 7.376 (br, 1H), 7.28 (s, 1H), 7.21 – 7.12 (m, 2H), 4.44 – 4.38 (m, 4H), 1.07 (t, J = 7.9 Hz, 9H), 0.71 (q, J = 7.9 Hz, 6H). ^{13}C NMR (126 MHz, $CDCl_3$): δ 155.95, 153.81 (d, J_{CF} = 248.0 Hz), 153.44, 149.62, 146.66, 144.47, 127.68, 127.60, 124.15 (d, J_{CF} = 4.5 Hz), 122.79, 114.49, 111.77 (d, J_{CF} = 14.6 Hz), 110.61, 105.97, 98.65, 98.49 (d, J_{CF} = 3.7 Hz), 64.70, 64.51, 7.63, 4.50. HRMS (DART): m/z $[M + H]^+$ calcd for $C_{24}H_{27}FN_3O_2Si^+$, 436.1851; found, 436.1831.

A mixture of triethylsilyl-protected compound **2** (40 mg, 0.09 mmol) in wet THF (0.9 mL) was treated dropwise with a 1 M solution of TBAF in THF (450 µL, 0.45 mmol), and the mixture was stirred at RT for 18 h. Water (10 mL) was added, and the mixture was extracted with EtOAc (3 x 15 mL). The combined organics were washed with brine (20 mL), dried (Na_2SO_4), filtered, and evaporated. Purification by flash chromatography (hexanes/EtOAc 7:3 → 3:7), followed by a second flash chromatography (CH_2Cl_2/EtOAc 1:0 → 6:4) afforded **2** (19 mg, 64%) as an off-white solid.

^{1}H NMR (500 MHz, $CDCl_3$): δ 8.69 (td, J = 8.0, 1.9 Hz, 1H), 8.67 (s, 1H), 7.38 (s, 1H), 7.36 (br, 1H), 7.29 (s, 1H), 7.21 (ddd, J = 8.1, 6.3, 1.9 Hz, 1H), 7.17 (td, J = 7.8, 0.9 Hz, 1H), 4.44 – 4.37 (m, 4H), 3.34 (s, 1H). ^{13}C NMR (126 MHz, $CDCl_3$): δ 155.94, 154.04 (d, J_{CF} = 248.6 Hz), 153.39, 149.65, 146.69, 144.47, 127.81, 127.67 (d, J_{CF} = 9.2 Hz), 124.29 (d, J_{CF} = 4.7 Hz), 123.48, 114.48, 110.58, 110.50 (d, J_{CF} = 14.3 Hz), 105.99, 82.95 (d, J_{CF} = 3.6 Hz), 76.70 (d, J_{CF} = 1.7 Hz), 64.69, 64.50. HRMS (DART): m/z $[M + H]^+$ calcd for $C_{18}H_{13}FN_3O_2^+$, 322.0986; found, 322.0981.

3-[(7,8-Dihydro[1,4]dioxino[2,3-*g*]quinazolin-4-yl)amino]-2-fluorobenzonitrile (3)

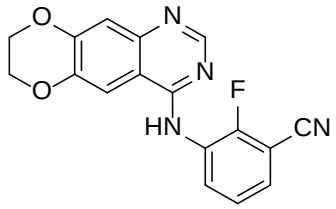

A 1 dram vial was charged with **4** (75 mg, 0.23 mmol), *t*BuXPhos-Pd-G3 (9 mg, 0.01 mmol), and $Zn(CN)_2$ (18 mg, 0.15 mmol). The vial was evacuated and backfilled with Ar (3x). THF (190 µL) and degassed water (940 µL) were added. The vial was sealed, and vigorously stirred at 40 °C for 18.5 h. Sat. aq. $NaHCO_3$ (20 mL) was added, and the mixture was extracted with EtOAc (3 x 13 mL). The combined organics were washed with water (13 mL), brine (13 mL), dried (Na_2SO_4), filtered, and concentrated in vacuo. Flash chromatography (CH_2Cl_2/EtOAc 1:0 → 1:1) gave **3** (20 mg, 27%) as a yellow solid together with recovered **4** (46 mg, 61%) as a white solid.

^{1}H NMR (500 MHz, $CDCl_3$): δ 9.06 – 8.98 (m, 1H), 8.69 (s, 1H), 7.41 (s, 1H), 7.39 (br, 1H), 7.35 – 7.31 (m, 2H), 7.30 (s, 1H), 4.45 – 4.37 (m, 4H). ^{13}C NMR (126 MHz, $CDCl_3$): δ 155.63, 153.63 (d, J_{CF} = 254.6 Hz), 153.04, 149.94, 146.80, 144.76, 128.60 (d, J_{CF} = 7.8 Hz), 127.48, 126.58, 125.31 (d, J_{CF} = 4.5 Hz), 114.56, 113.80, 110.45, 105.83, 101.30 (d, J_{CF} = 13.9 Hz), 64.70, 64.51. HRMS (ESI): *m*/*z* $[M + H]^+$ calcd for $C_{17}H_{12}FN_4O_2^+$, 323.0939; found, 323.0927.

***N*-(3-Chloro-2-fluorophenyl)-7,8-dihydro[1,4]dioxino[2,3-*g*]quinazolin-4-amine (4)**

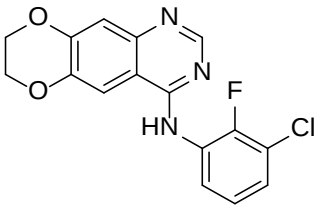

Following general procedure **GP-1**, compound **4** was prepared from the chloroquinazoline **24** (401 mg, 1.80 mmol) and 3-chloro-2-fluoroaniline (396 µL, 3.60 mmol) in isopropanol (3.6 mL). After

the reaction, the precipitated hydrochloride salt of **4** was converted into the free base by extraction of a sat. aq. $NaHCO_3$ solution to obtain pure **4** (507 mg, 85%) as a pale-yellow solid.

^{1}H NMR (500 MHz, $CDCl_3$): δ 8.69 (s, 1H), 8.60 (td, J = 7.3, 2.3 Hz, 1H), 7.39 (s, 1H), 7.34 (br, 1H), 7.30 (s, 1H), 7.20 – 7.10 (m, 2H), 4.45 – 4.38 (m, 4H). ^{13}C NMR (126 MHz, $CDCl_3$): δ 155.90, 153.37, 149.71, 149.33 (d, J_{CF} = 244.2 Hz), 146.75, 144.53, 128.75 (d, J_{CF} = 9.3 Hz), 124.71 (d, J_{CF} = 5.1 Hz), 124.48, 121.07, 120.86 (d, J_{CF} = 16.1 Hz), 114.54, 110.59, 105.95, 64.70, 64.52. HRMS (DART): m/z $[M - H]^-$ calcd for $C_{16}H_{10}ClFN_3O_2^-$, 330.0451; found, 330.0457.

_N_-(3-Bromo-2-fluorophenyl)-7,8-dihydro[1,4]dioxino[2,3-*g*]quinazolin-4-amine (5)

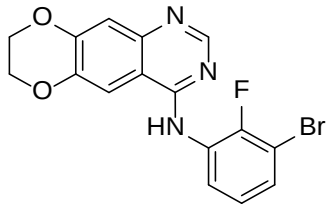

Preparation from the chloroquinazoline **24**: following general procedure **GP-1**, compound **5** was prepared from the chloroquinazoline **24** (100 mg, 0.45 mmol) and 3-bromo-2-fluoroaniline (100 µL, 0.89 mmol) in isopropanol (1.5 mL). Flash chromatography (CH_2Cl_2/EtOAc 10:0 → 10:3) gave **5** (150 mg, 89%) as a pale-yellow solid.

Preparation from the anthranilonitrile **S25**: a mixture of anthranilonitrile **S25** (2.388 g, 13.6 mmol) in toluene (35 mL) was treated with AcOH (35 µL, 0.61 mmol) and DMF-DMA (3.24 mL, 24.4 mmol), and stirred at 105 °C for 3 h. The mixture was cooled to 23 °C and evaporated to afford the corresponding *N*,*N*-dimethyl formamidine derivative (3.292 g, quant.) as a yellow, amorphous solid, which was used in the next step without any further purification.

^{1}H NMR (500 MHz, $CDCl_3$): δ 7.50 (s, 1H), 7.02 (s, 1H), 6.43 (s, 1H), 4.29 – 4.26 (m, 2H), 4.23 – 4.20 (m, 2H), 3.05 (s, 3H), 3.03 (s, 3H). ^{13}C NMR (126 MHz, $CDCl_3$): δ 153.69, 150.53, 148.11,

139.03, 121.05, 118.72, 108.10, 99.17, 64.91, 64.12, 40.39, 34.69. HRMS (DART): *m*/*z* $[M + H]^+$ calcd for $C_{12}H_{14}N_3O_2^+$, 232.1081; found, 232.1087.

A mixture of the crude *N*,*N*-dimethyl formamidine derivative (3.265 g, 14.1 mmol) in AcOH (36.4 mL) was treated with 3-bromo-2-fluoroaniline (1.98 mL, 17.6 mmol) and stirred at 125–130 °C for 3 h. The mixture was cooled to 23 °C, and poured into ice-water (70 mL). The pH was adjusted to ~9 with 30% aq. NH_4OH (46 mL), and EtOAc (18 mL) was added. The resulting mixture was stirred at 23 °C for 45 min, and filtered. The yellow residue was suspended in MeOH (70 mL), treated dropwise with conc. HCl (3.5 mL), and stirred vigorously until a precipitate formed, which was collected by filtration (washings with cold MeOH, 3 x 4 mL), and dried under HV to obtain the hydrochloride salt of **5** (3159 mg, 54%). The residue was suspended in sat. aq. $NaHCO_3$ (500 mL), and extracted with CH_2Cl_2 (3 x 200 mL). The combined organics were washed with water (150 mL), brine (150 mL), dried (Na_2SO_4), filtered, and evaporated to give **5** (2.622 g, 49%) as a yellow solid.

^{1}H NMR (500 MHz, $CDCl_3$): δ 8.68 (s, 1H), 8.65 (ddd, J = 8.3, 7.4, 1.5 Hz, 1H), 7.39 (s, 1H), 7.35 (br, 1H), 7.29 (s, 1H), 7.29 – 7.24 (m, 1H), 7.11 (td, J = 8.2, 1.6 Hz, 1H), 4.44 – 4.38 (m, 4H). ^{13}C NMR (126 MHz, $CDCl_3$): δ 155.89, 153.37, 150.15 (d, J_{CF} = 242.2 Hz), 149.70, 146.75, 144.53, 128.65 (d, J_{CF} = 10.5 Hz), 127.24, 125.31 (d, J_{CF} = 4.7 Hz), 121.79, 114.53, 110.59, 108.59 (d, J_{CF} = 19.4 Hz), 105.93, 64.70, 64.51. HRMS (DART): *m*/*z* $[M - H]^-$ calcd for $C_{16}H_{10}BrFN_3O_2^-$, 373.9946; found, 373.9946.

***N*-(2-Fluoro-3-iodophenyl)-7,8-dihydro[1,4]dioxino[2,3-*g*]quinazolin-4-amine (6)**

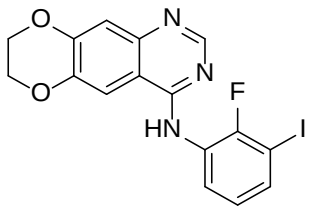

A 1 dram vial was charged with **5** (50 mg, 0.13 mmol), CuI (3.8 mg, 0.02 mmol), and NaI (42 mg, 0.28 mmol), and evacuated and backfilled with Ar (3x). Dioxane (0.9 mL) and (±)-*trans*-*N*,*N*-dimethylcyclohexane-1,2-diamine (6.3 µL, 0.04 mmol) were added. The vial was sealed and heated at 110 °C for 24 h. After cooling to 23 °C, sat. aq. $NaHCO_3$ (3 mL) was added, and the mixture transferred into water (15 mL). The mixture was extracted with CH_2Cl_2 (3 x 13 mL), and the combined organics were dried (Na_2SO_4), filtered, and evaporated. Purification by flash chromatography (CH_2Cl_2/EtOAc 1:0 → 3:1) gave **6** (47 mg, 84%) as an off-white solid.

^{1}H NMR (500 MHz, $CDCl_3$): δ 8.71 – 8.64 (m, 1H), 8.68 (s, 1H), 7.46 (ddd, J = 8.0, 5.9, 1.5 Hz, 1H), 7.39 (s, 1H), 7.34 (br, 1H), 7.28 (s, 1H), 6.99 (td, J = 8.1, 1.3 Hz, 1H), 4.45 – 4.38 (m, 4H). ^{13}C NMR (126 MHz, $CDCl_3$): δ 155.88, 153.39, 152.51 (d, J_{CF} = 240.3 Hz), 149.69, 146.73, 144.53, 132.95, 127.86 (d, J_{CF} = 11.5 Hz), 126.14 (d, J_{CF} = 4.3 Hz), 122.82, 114.53, 110.60, 105.93, 80.32 (d, J_{CF} = 23.9 Hz), 64.70, 64.51. HRMS (DART): *m*/*z* $[M + H]^+$ calcd for $C_{16}H_{12}FIN_3O_2^+$, 423.9953; found, 423.9958.

***N*-[2-Fluoro-3-(trifluoromethyl)phenyl]-7,8-dihydro[1,4]dioxino[2,3-*g*]quinazolin-4-amine (7)**

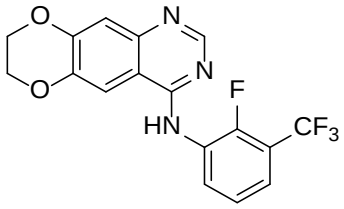

Following general procedure **GP-1**, compound **7** was prepared from the chloroquinazoline **24** (37 mg, 0.17 mmol) and 2-fluoro-3-(trifluoromethyl)aniline (42 µL, 0.33 mmol) in isopropanol (1.5 mL). Flash chromatography (CH_2Cl_2/EtOAc 1:0 → 10:3) gave **7** (35 mg, 58%) as an off-white solid. ^{1}H NMR (500 MHz, $CDCl_3$): δ 9.00 – 8.92 (m, 1H), 8.70 (s, 1H), 7.42 (br, 1H), 7.40 (s, 1H), 7.35 – 7.28 (m, 2H), 7.30 (s, 1H), 4.46 – 4.38 (m, 4H). ^{13}C NMR (126 MHz, $CDCl_3$): δ 155.77, 153.24, 150.27 (d, J_{CF} = 252.0 Hz), 149.81, 146.80, 144.66, 128.62 (d, J_{CF} = 8.5 Hz), 126.34, 124.44, 124.40, 122.66 (q, J_{CF} = 272.4 Hz), 120.41 (q, J_{CF} = 4.6 Hz), 114.58, 110.55, 105.86, 64.70, 64.51. HRMS (DART): *m*/*z* $[M - H]^-$ calcd for $C_{17}H_{10}F_4N_3O_2^-$, 364.0715; found, 364.0712.

3-[(7,8-Dihydro[1,4]dioxino[2,3-*g*]quinazolin-4-yl)amino]benzonitrile (8)

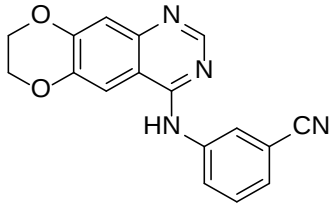

Following general procedure **GP-1**, compound **8** was prepared from the chloroquinazoline **24** (35 mg, 0.16 mmol) and 3-aminobenzonitrile (42 mg, 0.35 mmol) in isopropanol (1.5 mL). Flash chromatography (CH_2Cl_2/EtOAc 1:0 → 6:4) gave **8** (43 mg, 89%) as a white solid.

^{1}H NMR (500 MHz, DMSO-d_6): δ 9.68 (s, 1H), 8.52 (s, 1H), 8.46 (t, J = 1.9 Hz, 1H), 8.18 (ddd, J = 8.2, 2.3, 1.2 Hz, 1H), 8.08 (s, 1H), 7.58 (t, J = 7.9 Hz, 1H), 7.53 (dt, J = 7.6, 1.4 Hz, 1H), 7.22 (s, 1H), 4.45 – 4.38 (m, 4H). ^{13}C NMR (126 MHz, DMSO-d_6): δ 156.24, 152.69, 149.31, 146.15, 143.80, 140.52, 129.87, 126.35, 125.96, 124.15, 118.93, 112.66, 111.23, 109.96, 108.30, 64.52, 64.19. HRMS (DART): m/z [M + H]$^+$ calcd for $C_{17}H_{13}N_4O_2^+$, 305.1033; found, 305.1018.

_N_-(3-Chlorophenyl)-7,8-dihydro[1,4]dioxino[2,3-*g*]quinazolin-4-amine (9)

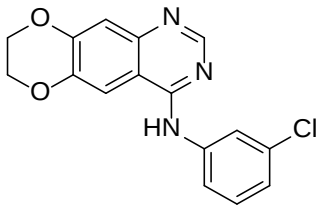

Following general procedure **GP-1**, compound **9** was prepared from the chloroquinazoline **24** (40 mg, 0.18 mmol) and 3-chloroaniline (38 µL, 0.36 mmol) in isopropanol (1.5 mL). Flash chromatography (CH_2Cl_2/EtOAc 8:2 → 1:1) gave **9** (51 mg, 91%) as a white solid.

^{1}H NMR (500 MHz, DMSO-d_6): δ 9.54 (s, 1H), 8.50 (s, 1H), 8.13 (t, J = 2.1 Hz, 1H), 8.08 (s, 1H), 7.85 (ddd, J = 8.2, 2.1, 0.9 Hz, 1H), 7.39 (t, J = 8.1 Hz, 1H), 7.20 (s, 1H), 7.13 (ddd, J = 8.0, 2.1, 0.9 Hz, 1H), 4.45 – 4.37 (m, 4H). ^{13}C NMR (126 MHz, DMSO-d_6): δ 156.29, 152.76, 149.19, 146.09, 143.71, 141.15, 132.70, 130.03, 122.62, 120.86, 119.82, 112.62, 110.00, 108.34, 64.50, 64.17. HRMS (DART): m/z [M + H]$^+$ calcd for $C_{16}H_{13}ClN_3O_2^+$, 314.0691; found, 314.0688.

_N_-(3-Bromophenyl)-7,8-dihydro[1,4]dioxino[2,3-*g*]quinazolin-4-amine (10)

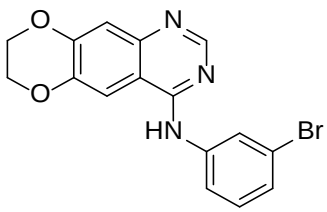

Following general procedure **GP-2**, compound **10** was prepared from the chloroquinazoline **24** (35 mg, 0.16 mmol), 3-bromooaniline (34 µL, 0.32 mmol), and a 4 M solution of HCl in dioxane (39 µL, 0.16 mmol) in acetonitrile (1.5 mL). Flash chromatography (CH_2Cl_2/EtOAc 9:1 → 6:4) gave **10** (54 mg, 96%) as a white solid.

^{1}H NMR (500 MHz, DMSO-d_6): δ 9.53 (s, 1H), 8.49 (s, 1H), 8.25 (t, J = 2.0 Hz, 1H), 8.08 (s, 1H), 7.92 (ddd, J = 8.1, 2.1, 1.0 Hz, 1H), 7.33 (t, J = 8.0 Hz, 1H), 7.26 (ddd, J = 7.9, 2.0, 1.0 Hz, 1H), 7.20 (s, 1H), 4.45 – 4.37 (m, 4H). ^{13}C NMR (126 MHz, DMSO-d_6): δ 156.27, 152.77, 149.19, 146.09, 143.71, 141.29, 130.35, 125.52, 123.68, 121.18, 120.22, 112.62, 110.00, 108.34, 64.50, 64.17. HRMS (ESI): m/z $[M + H]^+$ calcd for $C_{16}H_{13}BrN_3O_2^+$, 358.0186; found, 358.0182.

2-Bromo-6-[(7,8-dihydro[1,4]dioxino[2,3-*g*]quinazolin-4-yl)amino]phenol (11)

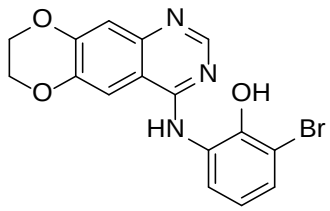

Following general procedure **GP-1**, compound **11** was prepared from the chloroquinazoline **24** (150 mg, 0.67 mmol) and 2-amino-6-bromophenol (254 mg, 1.35 mmol) in isopropanol (1.5 mL). Flash chromatography (CH_2Cl_2/EtOAc 9:1 → 6:4) afforded **11** (241 mg, 96%) as a rose-colored solid.

^{1}H NMR (500 MHz, DMSO-d_6): δ 10.60 (br, 1H), 9.50 (br, 1H), 8.35 (s, 1H), 8.04 (s, 1H), 7.45 (dd, J = 8.0, 1.5 Hz, 1H), 7.34 (dd, J = 7.9, 1.5 Hz, 1H), 7.18 (s, 1H), 6.83 (t, J = 8.0 Hz, 1H), 4.44 – 4.37 (m, 4H). ^{13}C NMR (126 MHz, DMSO-d_6): δ 157.19, 152.05, 149.33, 148.65, 145.62, 143.55, 130.14, 128.35, 126.32, 120.29, 112.54, 112.12, 109.82, 109.18, 64.55, 64.14. HRMS (DART): m/z $[M + H]^+$ calcd for $C_{16}H_{13}BrN_3O_3^+$, 374.0135; found, 374.0142.

***N*-(3-Bromo-2,4-difluorophenyl)-7,8-dihydro[1,4]dioxino[2,3-*g*]quinazolin-4-amine (12)**

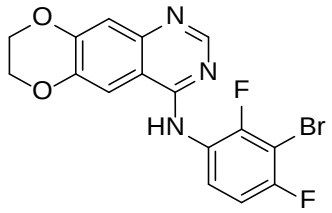

Following general procedure **GP-2**, compound **12** was prepared from the chloroquinazoline **24** (35 mg, 0.16 mmol), 3-bromo-2,4-difluoroaniline (65 mg, 0.31 mmol), and a 4 M solution of HCl in dioxane (39 µL, 0.16 mmol) in acetonitrile (1.5 mL). Flash chromatography (CH_2Cl_2/EtOAc 1:0 → 7:3) gave **12** (54 mg, 87%) as an off-white solid.

^{1}H NMR (500 MHz, $CDCl_3$): δ 8.64 (s, 1H), 8.51 (td, J = 9.0, 5.6 Hz, 1H), 7.38 (s, 1H), 7.29 (s, 1H), 7.23 (br, 1H), 7.04 (ddd, J = 9.2, 7.8, 2.1 Hz, 1H), 4.45 – 4.37 (m, 4H). ^{13}C NMR (126 MHz, $CDCl_3$): δ 156.10, 155.80 (dd, J_{CF} = 246.6, 3.5 Hz), 153.28, 151.25 (dd, J_{CF} = 245.1, 4.0 Hz), 149.74, 146.56, 144.53, 124.39 (dd, J_{CF} = 10.8, 3.4 Hz), 122.72 (dd, J_{CF} = 8.3, 1.8 Hz), 114.42, 111.49 (dd, J_{CF} = 22.5, 3.9 Hz), 110.34, 105.98, 97.86 (dd, J_{CF} = 25.7, 22.9 Hz), 64.69, 64.50. HRMS (ESI): m/z $[M + H]^+$ calcd for $C_{16}H_{11}BrF_2N_3O_2^+$, 393.9997; found, 394.0013.

***N*-(3-Bromo-4-chloro-2-fluorophenyl)-7,8-dihydro[1,4]dioxino[2,3-*g*]quinazolin-4-amine (13)**

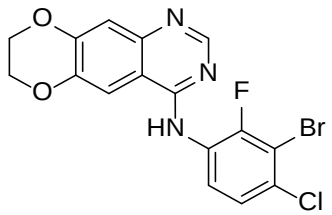

Following general procedure **GP-1**, compound **13** was prepared from the chloroquinazoline **24** (35 mg, 0.16 mmol) and 3-bromo-4-chloro-2-fluoroaniline (**S12**) (70 mg, 0.31 mmol) in isopropanol (1.5 mL). After the reaction, the precipitated hydrochloride salt of **13** was converted into the free

base by extraction of a sat. aq. $NaHCO_3$ solution to obtain pure **13** (35 mg, 54%) as a fluffy pale-yellow solid.

^{1}H NMR (500 MHz, DMSO-d_6): δ 9.70 (s, 1H), 8.35 (s, 1H), 7.94 (s, 1H), 7.61 (dd, J = 8.8, 7.7 Hz, 1H), 7.55 (dd, J = 8.7, 1.5 Hz, 1H), 7.20 (s, 1H), 4.47 – 4.35 (m, 4H). ^{13}C NMR (126 MHz, DMSO-d_6): δ 157.03, 154.14 (d, J_{CF} = 249.5 Hz), 153.01, 149.36, 146.08, 143.74, 130.75, 127.77 (d, J_{CF} = 2.9 Hz), 126.80 (d, J_{CF} = 13.4 Hz), 125.37 (d, J_{CF} = 3.8 Hz), 112.50, 110.15 (d, J_{CF} = 22.5 Hz), 109.66, 108.39, 64.51, 64.14. HRMS (DART): m/z $[M + H]^+$ calcd for $C_{16}H_{11}BrClFN_3O_2^+$, 409.9702; found, 409.9697.

_N_-(3,4-Dibromo-2-fluorophenyl)-7,8-dihydro[1,4]dioxino[2,3-_g_]quinazolin-4-amine (14)

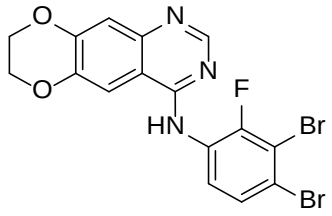

Following general procedure **GP-2**, compound **14** was prepared from the chloroquinazoline **24** (40 mg, 0.18 mmol), 3,4-dibromo-2-fluoroaniline (**S13**) (96 mg, 0.36 mmol), and a 4 M solution of HCl in dioxane (45 µL, 0.18 mmol) in acetonitrile (1.5 mL). Flash chromatography (CH_2Cl_2/EtOAc 1:0 → 7:3) gave **14** (67 mg, 82%) as a white solid.

^{1}H NMR (500 MHz, DMSO-d_6): δ 9.65 (s, 1H), 8.34 (s, 1H), 7.92 (s, 1H), 7.67 (d, J = 8.7 Hz, 1H), 7.55 (t, J = 8.2 Hz, 1H), 7.20 (s, 1H), 4.45 – 4.35 (m, 4H). ^{13}C NMR (126 MHz, DMSO-d_6): δ 156.95, 153.98 (d, J_{CF} = 249.1 Hz), 152.99, 149.35, 146.09, 143.74, 128.50 (d, J_{CF} = 3.7 Hz), 128.14, 127.21 (d, J_{CF} = 13.7 Hz), 120.96, 112.51, 112.33, 109.68, 108.36, 64.51, 64.14. HRMS (DART): m/z $[M + H]^+$ calcd for $C_{16}H_{11}Br_2FN_3O_2^+$, 453.9197; found, 453.9191.

***N*-(3-Bromo-2,5-difluorophenyl)-7,8-dihydro[1,4]dioxino[2,3-*g*]quinazolin-4-amine (15)**

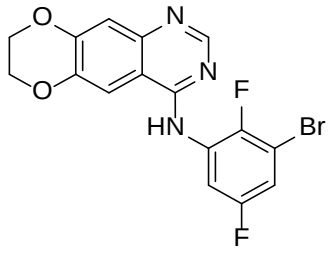

Following general procedure **GP-2**, compound **15** was prepared from the chloroquinazoline **24** (35 mg, 0.16 mmol), 3-bromo-2,5-difluoroaniline (**S14**) (54 mg, 0.26 mmol), and a 4 M solution of HCl in dioxane (39 µL, 0.16 mmol) in acetonitrile (1.5 mL). Flash chromatography (CH_2Cl_2/EtOAc 1:0 → 7:3) gave **15** (57 mg, 92%) as an off-white solid.

^{1}H NMR (500 MHz, DMSO-d_6): δ 9.65 (s, 1H), 8.40 (s, 1H), 7.93 (s, 1H), 7.63 – 7.54 (m, 2H), 7.21 (s, 1H), 4.45 – 4.37 (m, 4H). ^{13}C NMR (126 MHz, DMSO-d_6): δ 157.29 (d, J_{CF} = 243.5 Hz), 156.84, 152.93, 149.97 (d, J_{CF} = 242.9 Hz), 149.43, 146.16, 143.81, 128.83 (m), 116.30 (d, J_{CF} = 26.7 Hz), 113.99 (d, J_{CF} = 25.7 Hz), 112.53, 109.73, 108.76 (dd, J_{CF} = 22.5, 12.5 Hz), 108.33, 64.52, 64.15. HRMS (DART): *m*/*z* $[M + H]^+$ calcd for $C_{16}H_{11}BrF_2N_3O_2^+$, 393.9997; found, 393.9988.

***N*-(3-Bromo-5-chloro-2-fluorophenyl)-7,8-dihydro[1,4]dioxino[2,3-*g*]quinazolin-4-amine (16)**

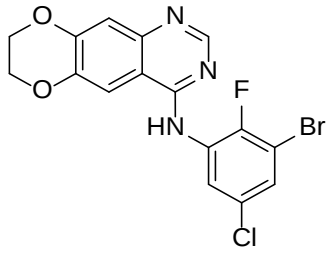

Following general procedure **GP-2**, compound **16** was prepared from the chloroquinazoline **24** (35 mg, 0.16 mmol), 3-bromo-5-chloro-2-fluoroaniline (**S15**) (71 mg, 0.32 mmol), and a 4 M

solution of HCl in dioxane (39 µL, 0.16 mmol) in acetonitrile (1.5 mL). Flash chromatography (hexanes/ CH_2Cl_2 1:9 → CH_2Cl_2/EtOAc 1:0 → 7:3) gave **16** (36 mg, 56%) as a white solid.

^{1}H NMR (500 MHz, $CDCl_3$): δ 8.88 (dd, J = 6.6, 2.6 Hz, 1H), 8.73 (s, 1H), 7.41 (s, 1H), 7.37 (br, 1H), 7.26 (s, 1H), 7.28 – 7.23 (m, 1H), 4.44 – 4.39 (m, 4H). ^{13}C NMR (126 MHz, $CDCl_3$): δ 155.45, 153.13, 149.88, 148.60 (d, J_{CF} = 241.7 Hz), 146.76, 144.72, 130.30 (d, J_{CF} = 4.4 Hz), 129.26 (d, J_{CF} = 10.8 Hz), 126.08, 121.21, 114.60, 110.49, 108.68 (d, J_{CF} = 20.9 Hz), 105.71, 64.70, 64.52. HRMS (ESI): m/z $[M + H]^+$ calcd for $C_{16}H_{11}BrClFN_3O_2^+$, 409.9702; found, 409.9713.

_N_-(3,4-Dichloro-2-fluorophenyl)-7,8-dihydro[1,4]dioxino[2,3-_g_]quinazolin-4-amine (17)

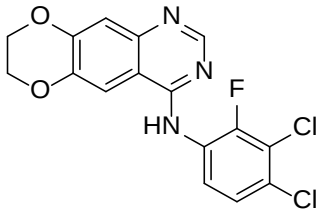

Following general procedure **GP-2**, compound **17** was prepared from the chloroquinazoline **24** (35 mg, 0.16 mmol), 3,4-dichloro-2-fluoroaniline (57 mg, 0.32 mmol), and a 4 M solution of HCl in dioxane (39 µL, 0.16 mmol) in acetonitrile (1.5 mL). Flash chromatography (CH_2Cl_2/EtOAc 1:0 → 3:1) gave **17** (46 mg, 80%) as a white solid.

^{1}H NMR (500 MHz, $CDCl_3$): δ 8.67 (s, 1H), 8.59 (t, J = 8.6 Hz, 1H), 7.40 (s, 1H), 7.38 (br, 1H), 7.33 (dd, J = 9.1, 2.1 Hz, 1H), 7.31 (s, 1H), 4.45 – 4.38 (m, 4H). ^{13}C NMR (126 MHz, $CDCl_3$): δ 155.84, 153.08, 149.98 (d, J_{CF} = 246.3 Hz), 149.88, 146.42, 144.67, 127.55, 127.19 (d, J_{CF} = 10.0 Hz), 125.30 (d, J_{CF} = 4.1 Hz), 121.05, 120.47 (d, J_{CF} = 18.2 Hz), 114.36, 110.43, 105.97, 64.71, 64.51. HRMS (ESI): m/z $[M + H]^+$ calcd for $C_{16}H_{11}Cl_2FN_3O_2^+$, 366.0207; found, 366.0207.

***N*-(5-Bromo-2-fluorophenyl)-7,8-dihydro[1,4]dioxino[2,3-*g*]quinazolin-4-amine (18)**

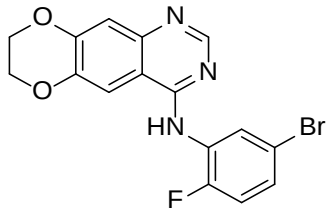

Following general procedure **GP-2**, compound **18** was prepared from the chloroquinazoline **24** (35 mg, 0.16 mmol), 5-bromo-2-fluoroaniline (60 mg, 0.32 mmol), and a 4 M solution of HCl in dioxane (40 µL, 0.16 mmol) in acetonitrile (1.5 mL). Flash chromatography (CH_2Cl_2/EtOAc 1:0 → 7:3) gave **18** (42 mg, 71%) as a white solid.

^{1}H NMR (500 MHz, $CDCl_3$): δ 8.99 (dd, J = 7.3, 2.5 Hz, 1H), 8.72 (s, 1H), 7.38 (s, 1H), 7.36 (br, 1H), 7.27 (s, 1H), 7.16 (ddd, J = 8.7, 4.6, 2.5 Hz, 1H), 7.04 (dd, J = 10.9, 8.7 Hz, 1H), 4.44 – 4.36 (m, 4H). ^{13}C NMR (126 MHz, $CDCl_3$): δ 155.59, 153.35, 152.16 (d, J_{CF} = 243.1 Hz), 149.69, 146.67, 144.52, 128.75 (d, J_{CF} = 10.5 Hz), 126.16 (d, J_{CF} = 7.6 Hz), 125.06, 117.19 (d, J_{CF} = 3.4 Hz), 116.20 (d, J_{CF} = 20.9 Hz), 114.52, 110.48, 105.85, 64.68, 64.50. HRMS (DART): *m*/*z* [M + H]$^+$ calcd for $C_{16}H_{12}BrFN_3O_2^+$, 376.0091; found, 376.0077.

***N*-(3-Bromo-2,6-difluorophenyl)-7,8-dihydro[1,4]dioxino[2,3-*g*]quinazolin-4-amine (19)**

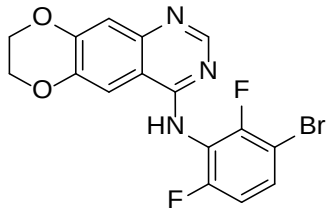

Following general procedure **GP-2**, compound **19** was prepared from chloroquinazoline **24** (35 mg, 0.16 mmol), 3-bromo-2,6-difluoroaniline (65 mg, 0.31 mmol), and a 4 M solution of HCl in dioxane (39 µL, 0.16 mmol) in acetonitrile (1.5 mL). Flash chromatography (CH_2Cl_2/EtOAc 1:0 → 6:4) gave **19** (29 mg, 47%) as a white solid.

^{1}H NMR (500 MHz, DMSO-d_6): δ 9.60 (s, 1H), 8.32 (s, 1H), 7.94 (s, 1H), 7.74 (td, J = 8.1, 5.5 Hz, 1H), 7.28 (t, J = 9.3 Hz, 1H), 7.21 (s, 1H), 4.44 – 4.38 (m, 4H). ^{13}C NMR (126 MHz, DMSO-d_6): δ 157.78 (dd, J_{CF} = 248.8, 3.3 Hz), 157.37, 155.01 (dd, J_{CF} = 247.9, 4.9 Hz), 153.08, 149.47, 146.04, 143.86, 130.76 (d, J_{CF} = 9.3 Hz), 117.30 (t, J_{CF} = 17.5 Hz), 113.30 (dd, J_{CF} = 21.8, 3.0 Hz), 112.56, 109.45, 108.28, 103.55 (dd, J_{CF} = 20.4, 3.6 Hz), 64.52, 64.14. HRMS (ESI): m/z [M + H]$^+$ calcd for $C_{16}H_{11}BrF_2N_3O_2^+$, 393.9997; found, 394.0008.

_N_-(2-Fluorophenyl)-7,8-dihydro[1,4]dioxino[2,3-_g_]quinazolin-4-amine (S1)

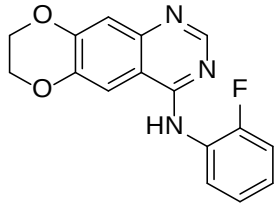

Following general procedure **GP-1**, compound **S1** was prepared from the chloroquinazoline **24** (51 mg, 0.23 mmol) and 2-fluoroaniline (40 µL, 0.48 mmol) in isopropanol (1.5 mL). Flash chromatography (CH_2Cl_2/EtOAc 10:1 → 10:4) gave **S1** (56 mg, 82%) as a white solid.

^{1}H NMR (500 MHz, $CDCl_3$): δ 8.68 (s, 1H), 8.64 (td, J = 8.2, 1.7 Hz, 1H), 7.38 (s, 1H), 7.36 (br, 1H), 7.31 (s, 1H), 7.22 (t, J = 7.5 Hz, 1H), 7.17 (ddd, J = 11.2, 8.3, 1.5 Hz, 1H), 7.10 – 7.05 (m, 1H), 4.44 – 4.37 (m, 4H). ^{13}C NMR (126 MHz, $CDCl_3$): δ 156.08, 153.60, 153.50 (d, J_{CF} = 242.7 Hz), 149.52, 146.65, 144.34, 127.31 (d, J_{CF} = 9.5 Hz), 124.66 (d, J_{CF} = 3.7 Hz), 123.97 (d, J_{CF} = 7.8 Hz), 122.89, 115.06 (d, J_{CF} = 19.3 Hz), 114.46, 110.62, 106.10, 64.69, 64.51. HRMS (DART): m/z [M – H]$^-$ calcd for $C_{16}H_{11}FN_3O_2^-$, 296.0841; found, 296.0841.

***N*-(3-Fluorophenyl)-7,8-dihydro[1,4]dioxino[2,3-*g*]quinazolin-4-amine (S2)**

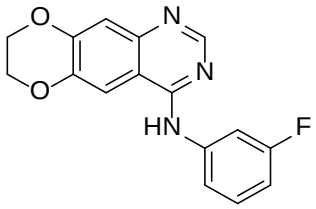

Following general procedure **GP-1**, compound **S2** was prepared from the chloroquinazoline **24** (40 mg, 0.18 mmol) and 3-fluoroaniline (35 µL, 0.36 mmol) in isopropanol (1.5 mL). After the reaction, the precipitated hydrochloride salt of **S2** was converted into the free base by extraction of a sat. aq. $NaHCO_3$ solution to obtain pure **S2** (30 mg, 56%) as an off-white solid.

^{1}H NMR (500 MHz, DMSO-d_6): δ 9.56 (s, 1H), 8.50 (s, 1H), 8.09 (s, 1H), 7.97 (dt, J = 12.1, 2.3 Hz, 1H), 7.69 (ddd, J = 8.3, 2.0, 0.9 Hz, 1H), 7.39 (td, J = 8.2, 6.9 Hz, 1H), 7.20 (s, 1H), 6.90 (tdd, J = 8.4, 2.6, 0.9 Hz, 1H), 4.45 – 4.36 (m, 4H). ^{13}C NMR (126 MHz, DMSO-d_6): δ 161.98 (d, J_{CF} = 240.4 Hz), 156.31, 152.77, 149.17, 146.09, 143.70, 141.44 (d, J_{CF} = 11.4 Hz), 129.89 (d, J_{CF} = 9.5 Hz), 117.11 (d, J_{CF} = 2.4 Hz), 112.62, 110.02, 109.36 (d, J_{CF} = 21.1 Hz), 108.35, 108.16 (d, J_{CF} = 26.2 Hz), 64.51, 64.18. HRMS (DART): m/z $[M + H]^+$ calcd for $C_{16}H_{13}FN_3O_2^+$, 298.0986; found, 298.0988.

***N*-(2,3-Difluorophenyl)-7,8-dihydro[1,4]dioxino[2,3-*g*]quinazolin-4-amine (S3)**

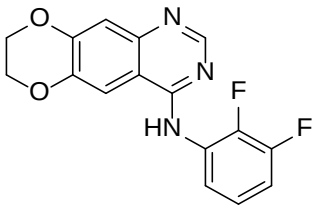

Following general procedure **GP-2**, compound **S3** was prepared from the chloroquinazoline **24** (35 mg, 0.16 mmol), 2,3-difluoroaniline (32 µL, 0.32 mmol), and a 4 M solution of HCl in dioxane (39 µL, 0.16 mmol) in acetonitrile (1.5 mL). After the reaction, the precipitated hydrochloride salt

of **S3** was converted into the free base by extraction of a sat. aq. $NaHCO_3$ solution to obtain pure **S3** (41 mg, 83%) as a white solid.

^{1}H NMR (500 MHz, DMSO-d_6): δ 9.64 (s, 1H), 8.34 (s, 1H), 7.94 (s, 1H), 7.36 – 7.29 (m, 2H), 7.27 – 7.21 (m, 1H), 7.19 (s, 1H), 4.44 – 4.37 (m, 4H). ^{13}C NMR (126 MHz, DMSO-d_6): δ 157.13, 153.12, 150.33 (dd, J_{CF} = 244.5, 11.7 Hz), 149.28, 146.06, 145.07 (dd, J_{CF} = 248.6, 13.5 Hz), 143.69, 128.60 (d, J_{CF} = 9.1 Hz), 124.01 (dd, J_{CF} = 8.3, 4.6 Hz), 123.27 (d, J_{CF} = 2.9 Hz), 114.14 (d, J_{CF} = 17.1 Hz), 112.49, 109.66, 108.40, 64.51, 64.14. HRMS (DART): *m/z* $[M + H]^+$ calcd for $C_{16}H_{12}F_2N_3O_2^+$, 316.0892; found 316.0878.

_N_-(2,4-Difluorophenyl)-7,8-dihydro[1,4]dioxino[2,3-_g_]quinazolin-4-amine (S4)

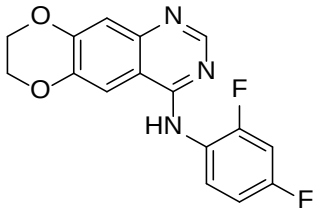

Following general procedure **GP-3**, compound **S4** was prepared from chloroquinazoline **24** (88 mg, 0.40 mmol) and 2,4-difluoroaniline (140 µL, 1.38 mmol) in DMF (2.2 mL). Flash chromatography afforded **S4** (36 mg, 29%) as a white solid.

^{1}H NMR (500 MHz, DMSO-d_6): δ 9.46 (s, 1H), 8.29 (s, 1H), 7.92 (s, 1H), 7.53 (td, J = 8.8, 6.2 Hz, 1H), 7.36 (ddd, J = 10.6, 9.1, 2.9 Hz, 1H), 7.17 (s, 1H), 7.14 (tdd, J = 8.5, 2.9, 1.3 Hz, 1H), 4.44 – 4.35 (m, 4H). ^{13}C NMR (126 MHz, DMSO-d_6): δ 159.90 (dd, J_{CF} = 244.4, 11.5 Hz), 157.56, 157.07 (dd, J_{CF} = 249.6, 12.9 Hz), 153.21, 149.14, 145.93, 143.57, 129.64 (dd, J_{CF} = 9.8, 3.1 Hz), 123.02 (dd, J_{CF} = 12.6, 3.7 Hz), 112.46, 111.24 (dd, J_{CF} = 22.0, 3.6 Hz), 109.56, 108.36, 104.47 (dd, J_{CF} = 26.5, 24.7 Hz), 64.49, 64.12. HRMS (ESI): *m/z* $[M + H]^+$ calcd for $C_{16}H_{12}F_2N_3O_2^+$, 316.0892; found, 316.0890.

***N*-(2,5-Difluorophenyl)-7,8-dihydro[1,4]dioxino[2,3-*g*]quinazolin-4-amine (S5)**

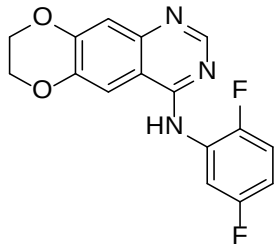

Following general procedure **GP-3**, compound **S5** was prepared from the chloroquinazoline **24** (44 mg, 0.20 mmol) and 2,5-difluoroaniline (67 µL, 0.66 mmol) in DMF (1.5 mL). Flash chromatography afforded **S5** (16 mg, 26%) as a white solid.

^{1}H NMR (500 MHz, DMSO-d_6): δ 9.52 (s, 1H), 8.36 (s, 1H), 7.95 (s, 1H), 7.52 (ddd, J = 9.5, 5.9, 3.2 Hz, 1H), 7.35 (td, J = 9.5, 5.0 Hz, 1H), 7.19 (s, 1H), 7.13 (ddd, J = 11.6, 8.1, 3.1 Hz, 1H), 4.45 – 4.35 (m, 4H). ^{13}C NMR (126 MHz, DMSO-d_6): δ 157.62 (dd, J_{CF} = 239.3, 1.6 Hz), 157.06, 153.04, 152.82 (dd, J_{CF} = 243.5, 2.3 Hz), 149.27, 146.08, 143.68, 127.78 (td, J_{CF} = 11.4, 2.3 Hz), 116.77 (dd, J_{CF} = 22.9, 9.7 Hz), 114.47 (d, J_{CF} = 25.9 Hz), 112.79 (dd, J_{CF} = 24.2, 8.1 Hz), 112.49, 109.72, 108.38, 64.50, 64.13. HRMS (ESI): *m/z* $[M + H]^+$ calcd for $C_{16}H_{12}F_2N_3O_2^+$, 316.0892; found, 316.0893.

***N*-(2,6-Difluorophenyl)-7,8-dihydro[1,4]dioxino[2,3-*g*]quinazolin-4-amine (S6)**

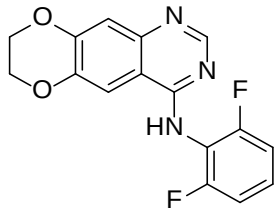

Following general procedure **GP-2**, compound **S6** was prepared from the chloroquinazoline **24** (35 mg, 0.16 mmol), 2,6-difluoroaniline (34 µL, 0.32 mmol), and a 4 M solution of HCl in dioxane (39 µL, 0.16 mmol) in acetonitrile (1.5 mL). After the reaction, the precipitated hydrochloride salt

of **S6** was converted into the free base by extraction of a sat. aq. $NaHCO_3$ solution to obtain crude **S6**, which was purified by PTLC (CH_2Cl_2/EtOAc 4:6) to obtain pure **S6** (31 mg, 63%) as a white solid.

^{1}H NMR (500 MHz, $CDCl_3$): δ 8.59 (s, 1H), 7.38 (s, 1H), 7.35 (s, 1H), 7.29 – 7.21 (m, 1H), 7.06 – 6.99 (m, 2H), 6.69 (br, 1H), 4.44 – 4.34 (m, 4H). ^{13}C NMR (126 MHz, $CDCl_3$): δ = 158.23 (dd, J_{CF} = 250.0, 4.8 Hz), 157.14, 153.86, 149.66, 146.71, 144.29, 127.37 (t, J_{CF} = 9.7 Hz), 115.44 (t, J_{CF} = 16.1 Hz), 114.20, 112.02 (dd, J_{CF} = 19.2, 4.4 Hz), 110.45, 106.79, 64.70, 64.48. HRMS (DART): *m/z* $[M - H]^-$ calcd for $C_{16}H_{10}F_2N_3O_2^-$, 314.0747; found 314.0733.

_N_-(2,4,6-Trifluorophenyl)-7,8-dihydro[1,4]dioxino[2,3-*g*]quinazolin-4-amine (S7)

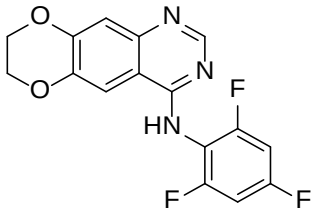

Following general procedure **GP-2**, compound **S7** was prepared from the chloroquinazoline **24** (35 mg, 0.16 mmol), 2,4,6-trifluoroaniline (46 mg, 0.32 mmol), and a 4 M solution of HCl in dioxane (39 µL, 0.16 mmol) in acetonitrile (1.5 mL). After the reaction, the precipitated hydrochloride salt of **S7** was converted into the free base by extraction of a sat. aq. $NaHCO_3$ solution to obtain pure **S7** (52 mg, 99%) as a white solid.

^{1}H NMR (500 MHz, $CDCl_3$): δ 8.56 (s, 1H), 7.38 (s, 1H), 7.34 (s, 1H), 6.85 – 6.78 (m, 2H), 6.56 (br, 1H), 4.43 – 4.36 (m, 4H). ^{13}C NMR (126 MHz, $CDCl_3$): δ 160.85 (dt, J_{CF} = 249.3, 14.6 Hz), 158.67 (ddd, J_{CF} = 251.2, 15.1, 7.0 Hz), 157.25, 153.77, 149.73, 146.70, 144.35, 114.24, 111.95 (td, J_{CF} = 16.5, 5.0 Hz), 110.23, 106.66, 100.96 (td, J_{CF} = 26.0, 2.9 Hz), 64.70, 64.48. HRMS (DART): *m/z* $[M + H]^+$ calcd for $C_{16}H_{11}F_3N_3O_2^+$, 334.0798; found 334.0789.

***N*-(Pentafluorophenyl)-7,8-dihydro[1,4]dioxino[2,3-*g*]quinazolin-4-amine (S8)**

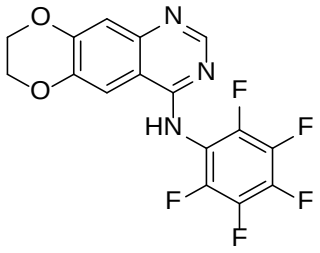

Following general procedure **GP-2**, compound **S8** was prepared from the chloroquinazoline **24** (35 mg, 0.16 mmol), pentafluoroaniline (58 mg, 0.32 mmol), and a 4 M solution of HCl in dioxane (39 µL, 0.16 mmol) in acetonitrile (1.5 mL). Flash chromatography (CH_2Cl_2/EtOAc 1:0 → 7:3) followed by PTLC (hexanes/EtOAc 4:6) gave **S8** (36 mg, 62%) as a white solid.

^{1}H NMR (500 MHz, $CDCl_3$): δ 8.57 (s, 1H), 7.41 (s, 1H), 7.34 (s, 1H), 6.64 (br, 1H), 4.45 – 4.37 (m, 4H). ^{13}C NMR (126 MHz, $CDCl_3$): δ 156.57, 153.40, 150.05, 146.89, 144.67, 114.34, 110.22, 106.52, 64.71, 64.50, carbons of perfluorophenyl ring not observed. HRMS (DART): *m*/*z* $[M + H]^+$ calcd for $C_{16}H_9F_5N_3O_2^+$, 370.0609; found, 370.0592.

6,7-Dimethoxyquinazolin-4(3*H*)-one (21)[48]

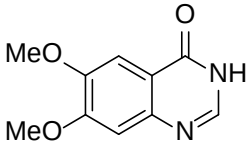

A mixture of methyl 2-amino-4,5-dimethoxybenzoate (**21**) (100.45 g, 475.6 mmol), formamide (793 mL), and formic acid (22.6 mL, 599.2 mmol) was stirred at 145 °C for 18 h. The mixture was cooled to 5 °C, water (800 mL) was added, and the suspension was stirred at 0–5 °C for 30 min. The precipitate was filtered off (washings with water), and recrystallized from EtOH (600 mL), and dried in a desiccator to afford the title compound **21** (89.44 g, 91%) as an off-white solid.

^{1}H NMR (300 MHz, DMSO-d_6): δ 12.07 (s, 1H), 7.98 (d, J = 3.5 Hz, 1H), 7.44 (s, 1H), 7.13 (s, 1H), 3.90 (s, 3H), 3.87 (s, 3H). ^{13}C NMR (101 MHz, DMSO-d_6): δ 160.03, 154.43, 148.53, 144.84, 143.82, 115.58, 108.00, 104.91, 55.91, 55.68. HRMS (DART): m/z $[M + H]^+$ calcd for $C_{10}H_{11}N_2O_3^+$, 207.0764; found, 207.0755.

4-Oxo-3,4-dihydroquinazoline-6,7-diyl bis(2,2-dimethylpropanoate) (22)[49,50]

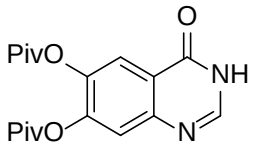

A mixture of quinazolinone **21** (89.39 g, 433.5 mmol) in 48% hydrobromic acid (1250 mL) was stirred at 135 °C for 18.5 h. The mixture was cooled to 10 °C, and filtered off. The residue was suspended in water (800 mL), and stirred at 10 °C for 30 min. The pH was adjusted to ~7 with sat. aq. NH_4OH (70 mL), and the precipitate was filtered off (washings with water (80 mL)), and dried in a desiccator to afford 6,7-dihydroxyquinazolin-4(3*H*)-one (81.36 g, quant.) as an off-white solid. ^{1}H NMR (400 MHz, DMSO-d_6): δ 11.82 (br, 1H), 10.15 (s, 1H), 9.77 (s, 1H), 7.84 (s, 1H), 7.36 (s, 1H), 6.94 (s, 1H). ^{13}C NMR (101 MHz, DMSO-d_6): δ 160.02, 152.38, 145.93, 143.65, 142.78, 115.06, 111.22, 109.10. HRMS (DART): m/z $[M + H]^+$ calcd for $C_8H_7N_2O_3^+$, 179.0451; found, 179.0444.

A mixture of 6,7-dihydroxyquinazolin-4(3*H*)-one (41.62 g, 233.6 mmol) in DMF (467 mL) was treated with Et_3N (98 mL, 700.9 mmol), cooled to 0 °C, and treated dropwise with pivaloyl chloride (86.3 mL, 700.9 mmol) over 45 min at 0–10 °C. The cooling bath was removed, and the mixture was stirred at 23 °C for 18 h. The mixture was treated dropwise with MeOH (20 mL) at 0 °C, stirred at 23 °C for 15 min, and concentrated. The residue was taken up in EtOAc (1250 mL), washed with water (1 x 100 mL, 4 x 20 mL), and concentrated. The residue was triturated with

water (100 mL), and filtered to give a red solid, which was washed several times with water (2 x 50 mL), and MeCN (2 x 40 mL), and dried in a desiccator to afford the title compound **22** (43.18 g, 53%) as an off-white solid.

^{1}H NMR (400 MHz, DMSO-d_6): δ 12.39 (br, 1H), 8.14 (s, 1H), 7.92 (s, 1H), 7.59 (s, 1H), 1.31 (s, 18H). ^{13}C NMR (101 MHz, DMSO-d_6): δ 175.34, 174.91, 159.75, 147.33, 147.25, 146.20, 141.06, 121.52, 120.81, 120.02, 38.76, 38.70, 26.75, 26.72. HRMS (DART): *m*/*z* $[M - H]^-$ calcd for $C_{18}H_{21}N_2O_5^-$, 345.1456; found, 345.1454.

4-Chloroquinazoline-6,7-diol (23)[50,51]

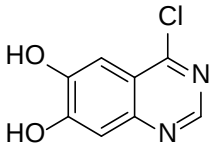

A stirred suspension of quinazolinone **22** (79.28 g, 228.9 mmol) in toluene (320 mL) was cooled to 10 °C, treated with DIPEA (120 mL, 689.0 mmol), and subsequently with $POCl_3$ (57 mL, 620.9 mmol) over 40 min. Stirring was continued at 23 °C for 1 h, and then at 90 °C for 6 h. The mixture was cooled to 23 °C, and concentrated. The residue was treated carefully with sat. aq. $NaHCO_3$ (700 mL) at 0 °C, and let stand for 1 h. The mixture was diluted with water (400 mL), and extracted with CH_2Cl_2 (3 x 500 mL). The combined organics were washed with half-sat. $NaHCO_3$ (400 mL), brine (400 mL), dried (Na_2SO_4), filtered, and evaporated to obtain crude 4-chloroquinazoline-6,7-diyl bis(2,2-dimethylpropanoate) (**S27**) (65.28 g, 78%) as a viscous brown oil, which was used without any further purification in the next step.

^{1}H NMR (400 MHz, $CDCl_3$): δ 9.02 (s, 1H), 8.03 (s, 1H), 7.88 (s, 1H), 1.41 (s, 9H), 1.40 (s, 9H). ^{13}C NMR (101 MHz, $CDCl_3$): δ 175.74, 175.31, 161.70, 154.16, 149.74, 149.62, 144.22, 122.33,

122.28, 119.11, 39.64, 39.57, 27.38, 27.31. HRMS (DART): *m*/*z* $[M + H]^+$ calcd for $C_{18}H_{22}ClN_2O_4^+$, 365.1263; found, 365.1251.

A stirred slurry of 4-chloroquinazoline-6,7-diyl bis(2,2-dimethylpropanoate) (**S27**) (23.39 g, 64.1 mmol) was treated dropwise at 0 °C with a 7 M solution of NH_3 in MeOH (229 mL, 1.603 mol). The mixture was stirred at 0 °C for 15 min, and then at 23 °C for 4 h, and evaporated. The residue was triturated with MeCN (150 mL), filtered, and washed several times with CH_2Cl_2 (4 x 100 mL), Et_2O (2 x 100 mL), and dried in a desiccator to yield the title compound **23** (11.92 g, 95%) as a yellow solid.

^{1}H NMR (500 MHz, DMSO-d_6): δ 8.35 (s, 1H), 6.98 (s, 1H), 6.59 (s, 1H), signals of phenolic protons missing (due to peak broadening). ^{13}C NMR (126 MHz, DMSO-d_6): δ 165.28, 154.36, 153.44, 150.45, 150.08, 114.74, 105.08, 99.75. HRMS (DART): *m*/*z* $[M - H]^-$ calcd for $C_8H_4ClN_2O_2^-$, 194.9967; found, 194.9968.

4-Chloro-7,8-dihydro[1,4]dioxino[2,3-*g*]quinazoline (24)[25,37]

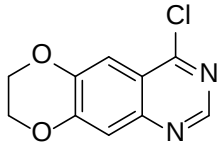

A solution of diol **23** (3.528 g, 17.9 mmol) in DMF (123 mL) was treated with K_2CO_3 (5586 mg, 40.4 mmol), stirred for 5–10 min, and treated dropwise with 1-bromo-2-chloroethane (5.4 mL, 64.6 mmol). The mixture was stirred at 23 °C for 1 h, and then at 70 °C for 15 h. The mixture was cooled to 23 °C, and evaporated. CH_2Cl_2 (400 mL) was added, and the organic phase was washed with water (2 x 60 mL), brine (60 mL), dried ($MgSO_4$), filtered, and concentrated. Flash chromatography (hexanes/CH_2Cl_2 1:10 → CH_2Cl_2/EtOAc 1:0 → 85:15) afforded the chloroquinazoline **24** (1.631 g, 41%) as a fluffy white solid.

^{1}H NMR (400 MHz, $CDCl_3$): δ 8.84 (s, 1H), 7.65 (s, 1H), 7.47 (s, 1H), 4.46 – 4.39 (m, 4H). ^{13}C NMR (101 MHz, $CDCl_3$): δ 160.19, 152.52, 151.55, 147.93, 146.07, 120.10, 113.73, 110.84, 64.75, 64.38. HRMS (DART): *m*/*z* $[M + H]^+$ calcd for $C_{10}H_8ClN_2O_2^+$, 223.0269; found, 223.0264.

4-(3-Amino-2-fluorophenyl)-2-methylbut-3-yn-2-ol (S17)

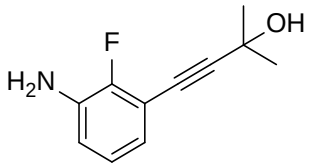

A vial was charged with $[Pd(OAc)_2]$ (18 mg, 0.08 mmol) and PPh_3 (42 mg, 0.16 mmol), and evacuated and backfilled with Ar (3x). THF (8 mL), DBU (1.18 mL, 7.89 mmol), 2-methyl-3-butyne-2-ol (316 µL, 3.26 mmol), and 3-bromo-2-fluoroaniline (**S16**) (546 mg, 2.87 mmol) were added, and the mixture was stirred at 80 °C for 12 h. The mixture was cooled to 23 °C, diluted with EtOAc (10 mL), and filtered through a plug of Celite (washings with EtOAc), and evaporated. Flash chromatography (hexanes/EtOAc 9:1 → 65:35) gave the title compound **S17** (482 mg, 87%) as a yellow oil, which solidified upon standing to give an off-white solid.

^{1}H NMR (400 MHz, $CDCl_3$): δ 6.85 (td, J = 7.8, 0.9 Hz, 1H), 6.77 (ddd, J = 7.7, 6.1, 1.7 Hz, 1H), 6.73 (td, J = 8.1, 1.8 Hz, 1H), 3.74 (br, 2H), 2.13 (s, 1H), 1.63 (s, 6H). ^{13}C NMR (101 MHz, $CDCl_3$): δ 151.74 (d, J_{CF} = 244.0 Hz), 134.67 (d, J_{CF} = 12.5 Hz), 124.08 (d, J_{CF} = 4.5 Hz), 122.58, 117.20 (d, J_{CF} = 3.9 Hz), 111.20 (d, J_{CF} = 13.5 Hz), 98.65 (d, J_{CF} = 3.7 Hz), 75.97 (d, J_{CF} = 1.9 Hz), 65.85, 31.55. HRMS (DART): *m*/*z* $[M - H]^-$ calcd for $C_{11}H_{11}FNO^-$, 192.0830; found, 192.0826.

3-Ethynyl-2-fluoroaniline (S11)

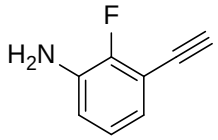

A mixture of aniline **S17** (360 mg, 1.86 mmol) and *n*Bu_4NI (69 mg, 0.19 mmol) in toluene (9.3 mL) was treated with 6 M NaOH (9.3 mL, 55.9 mmol), and stirred at 80 °C for 21 h. The mixture was cooled to 5 °C, treated with 1 M HCl (80 mL) and Et_2O (100 mL). The organic layer was separated, and washed with water, brine, dried ($MgSO_4$), filtered, and evaporated. Flash chromatography (hexanes/EtOAc 40:1 → 8:2) gave the title compound **S11** (66 mg, 26%) as a yellow oil.

^{1}H NMR (500 MHz, $CDCl_3$): δ 6.90 – 6.82 (m, 2H), 6.77 (ddd, J = 8.5, 7.6, 2.1 Hz, 1H), 3.77 (br, 2H), 3.27 (d, J = 0.7 Hz, 1H). ^{13}C NMR (126 MHz, $CDCl_3$): δ 152.27 (d, J_{CF} = 244.8 Hz), 134.74 (d, J_{CF} = 12.3 Hz), 124.19 (d, J_{CF} = 4.3 Hz), 122.98, 117.69 (d, J_{CF} = 4.1 Hz), 110.51 (d, J_{CF} = 13.4 Hz), 82.00 (d, J_{CF} = 3.7 Hz), 77.46 (d, J_{CF} = 2.1 Hz). HRMS (DART): m/z $[M]^{\bullet+}$ calcd for $C_8H_6FN^{\bullet+}$, 135.0479; found, 135.0470.

3-Bromo-4-chloro-2-fluoroaniline (S12)[52]

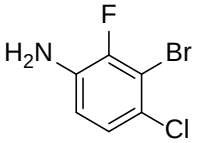

A mixture of 3-bromo-2-fluoroaniline (**S16**) (266 µL, 2.37 mmol) in DMF (2.4 mL) was treated with NCS (333 mg, 2.49 mmol), and stirred at 23 °C for 21.5 h. The reaction mixture was diluted with EtOAc (100 mL), and washed with brine (4 x 5 mL), dried (Na_2SO_4), filtered, and concentrated. Flash chromatography (hexanes/EtOAc 40:1 → 85:15) afforded the title compound **S12** (294 mg, 55%) as orange-red crystals which were grinded into a light-brown solid.

^{1}H NMR (500 MHz, $CDCl_3$): δ 7.04 (dd, J = 8.7, 1.9 Hz, 1H), 6.67 (t, J = 8.8 Hz, 1H), 3.81 (br, 2H). ^{13}C NMR (126 MHz, $CDCl_3$): δ 148.84 (d, J_{CF} = 240.9 Hz), 134.17 (d, J_{CF} = 14.2 Hz), 125.26 (d, J_{CF} = 3.7 Hz), 123.60, 115.76 (d, J_{CF} = 4.3 Hz), 110.61 (d, J_{CF} = 20.5 Hz). HRMS (DART): m/z $[M]^{\bullet+}$ calcd for $C_6H_4BrClFN^{\bullet+}$, 222.9194; found, 222.9188.

3,4-Dibromo-2-fluoroaniline (S13)

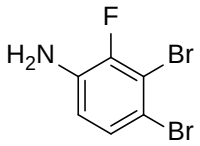

A mixture of 3-bromo-2-fluoroaniline (**S16**) (266 µL, 2.37 mmol) in DMF (2.4 mL) was treated with NBS (445 mg, 2.50 mmol), and stirred at 23 °C for 22 h. The reaction mixture was diluted with EtOAc (100 mL), and washed with brine (4 x 5 mL), dried (Na_2SO_4), filtered, and concentrated. Flash chromatography (hexanes/EtOAc 40:1 → 8:2) afforded the title compound **S13** (581 mg, 91%) as a light-brown solid.

^{1}H NMR (400 MHz, $CDCl_3$): δ 7.18 (dd, J = 8.6, 1.8 Hz, 1H), 6.62 (t, J = 8.7 Hz, 1H), 3.83 (br, 2H). ^{13}C NMR (101 MHz, $CDCl_3$): δ 148.80 (d, J_{CF} = 241.6 Hz), 134.72 (d, J_{CF} = 14.2 Hz), 128.39 (d, J_{CF} = 3.8 Hz), 116.36 (d, J_{CF} = 4.3 Hz), 112.74 (d, J_{CF} = 20.3 Hz), 112.40. HRMS (DART): m/z $[M]^{\bullet+}$ calcd for $C_6H_4Br_2FN^{\bullet+}$, 266.8689; found, 266.8686.

***tert*-Butyl *N*-(3-bromo-2,5-difluorophenyl)carbamate (S19)**

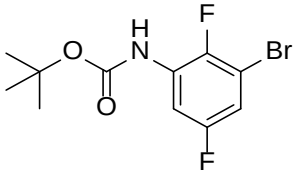

A 1 dram vial was charged with 1,3-dibromo-2,5-difluorobenzene (**S18**) (150 mg, 0.55 mmol), *tert*-butyl carbamate (66 mg, 0.56 mmol), [$Pd(OAc)_2$] (12.4 mg, 0.06 mmol), Xantphos (64 mg,

0.11 mmol), and Cs_2CO_3 (270 mg, 0.83 mmol). The vial was evacuated and backfilled with Ar (3x), and dioxane (2.5 mL) was added. The mixture was stirred at 23 °C for 5 min, and then at 100 °C for 23 h. The reaction mixture was cooled to 23 °C, diluted with EtOAc, filtered through a plug of Celite (washings with EtOAc), and evaporated. Flash chromatography (hexanes/EtOAc 40:1 → 15:1) provided the title compound **S19** (113 mg, 67%) as a clear, colorless oil, which turned into a white solid upon standing.

^{1}H NMR (400 MHz, $CDCl_3$): δ 7.93 (ddd, J = 9.8, 5.8, 3.2 Hz, 1H), 6.90 (ddd, J = 7.4, 5.2, 3.1 Hz, 1H), 6.76 (br, 1H), 1.53 (s, 9H). ^{13}C NMR (126 MHz, $CDCl_3$): δ 158.55 (dd, J_{CF} = 244.7, 3.1 Hz), 151.86, 145.33 (dd, J_{CF} = 237.7, 3.6 Hz), 128.91 (t, J_{CF} = 12.7 Hz), 112.68 (d, J_{CF} = 27.2 Hz), 108.15 (dd, J_{CF} = 21.4, 12.2 Hz), 106.37 (d, J_{CF} = 30.2 Hz), 82.15, 28.34. HRMS (DART): *m*/*z* [M – H]$^-$ calcd for $C_{11}H_{11}BrF_2NO_2^-$, 305.9947; found, 305.9949.

3-Bromo-2,5-difluoroaniline (S14)[53]

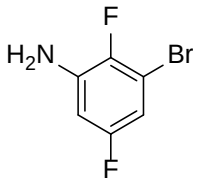

A mixture of compound **S19** (106 mg, 0.34 mmol) in CH_2Cl_2/CF_3CO_2H 2:1 (3.45 mL) was stirred at 23 °C for 19.5 h. The reaction mixture was concentrated, diluted with half-sat. aq. $NaHCO_3$ (20 mL), and extracted with CH_2Cl_2 (3 x 20 mL). The combined organics were washed with water (20 mL), brine (20 mL), dried (Na_2SO_4), filtered, and evaporated to give the title compound **S14** (62 mg, 87%) as a yellow oil.

^{1}H NMR (400 MHz, $CDCl_3$): δ 6.61 (ddd, J = 7.8, 4.8, 2.9 Hz, 1H), 6.43 (ddd, J = 9.5, 6.6, 2.9 Hz, 1H), 3.85 (br, 2H). ^{13}C NMR (101 MHz, $CDCl_3$): δ 158.82 (dd, J_{CF} = 243.7, 3.0 Hz), 145.01 (dd, J_{CF} = 234.6, 3.3 Hz), 136.42 (dd, J_{CF} = 15.5, 12.2 Hz), 108.88 (dd, J_{CF} = 20.7, 12.8 Hz), 108.39

(d, J_{CF} = 27.0 Hz), 102.63 (dd, J_{CF} = 27.0, 3.0 Hz). HRMS (DART): *m*/*z* $[M + H]^+$ calcd for $C_6H_5BrF_2N^+$, 207.9568; found, 207.9563.

3-Bromo-5-chloro-2-fluorobenzoic acid (S21)[52]

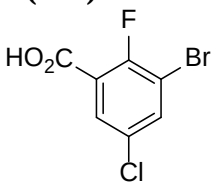

A mixture of 1.6 M *n*-butyllithium (*n*BuLi) in hexanes (15.4 mL, 24.64 mmol) in THF (32 mL) was treated consecutively with $(i\text{Pr})_2\text{NH}$ (3.45 mL, 24.63 mmol) and 2-bromo-4-chloro-1-fluorobenzene (**S20**) (4.962 g, 23.69 mmol) at –78 °C. After 2 h at that temperature, the mixture was poured via cannula onto an excess of freshly crushed pieces of solid CO_2 under an Ar atmosphere. The suspension was allowed to warm to 23 °C while stirring. All volatiles were removed in vacuo, water (200 mL) was added, and the mixture was extracted with Et_2O (3 x 70 mL). The aqueous layer was acidified with 6 M HCl (10 mL), and extracted with CH_2Cl_2 (3 x 100 mL). The combined organics were washed with brine (100 mL), dried ($MgSO_4$), filtered, and evaporated to afford the title compound **S21** (4.953 g, 83%) as a white solid, contaminated with about 10% of the regioisomer.

^{1}H NMR (400 MHz, DMSO-d_6): δ 13.88 (br, 1H), 8.13 (dd, J = 5.4, 2.7 Hz, 1H), 7.83 (dd, J = 5.7, 2.7 Hz, 1H). ^{13}C NMR (101 MHz, DMSO-d_6): δ 163.05 (d, J_{CF} = 3.6 Hz), 156.16 (d, J_{CF} = 256.9 Hz), 136.48, 130.55, 128.89 (d, J_{CF} = 4.4 Hz), 122.08 (d, J_{CF} = 13.1 Hz), 111.17 (d, J_{CF} = 23.5 Hz). HRMS (DART): *m*/*z* $[M - H]^-$ calcd for $C_7H_2BrClFO_2^-$, 250.8916; found, 250.8918.

3-Bromo-5-chloro-2-fluoroaniline (S15)[25]

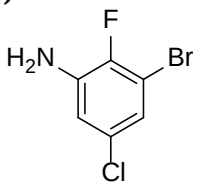

A mixture of benzoic acid **S21** (2.500 g, 9.86 mmol) in toluene/*t*BuOH 1:1 (50 mL) was treated with diisopropylethylamine (2.1 mL, 12.08 mmol), and with diphenylphosphoryl azide (2.6 mL, 12.08 mmol) at 10 °C. The mixture was stirred at 23 °C for 25 min, and then at 100 °C for 16 h. The reaction mixture was cooled to 23 °C, and evaporated. The residue was dissolved in EtOAc (350 mL), and washed with sat. $NaHCO_3$ (100 mL), water (100 mL), brine (100 mL), dried ($MgSO_4$), filtered, and evaporated. Purification by flash chromatography (hexanes/EtOAc 50:1 → 7:3) gave a mixture of compounds which was again purified by flash chromatography (hexanes/CH_2Cl_2 1:0 → 7:3) to directly afford the deprotected aniline **S15** (328 mg, 15%) as a hard, white solid.

^{1}H NMR (500 MHz, $CDCl_3$): δ 6.87 (dd, J = 5.3, 2.4 Hz, 1H), 6.69 (dd, J = 7.1, 2.5 Hz, 1H), 3.88 (br, 2H). ^{13}C NMR (126 MHz, $CDCl_3$): δ 147.07 (d, J_{CF} = 238.8 Hz), 136.40 (d, J_{CF} = 14.9 Hz), 129.89 (d, J_{CF} = 4.2 Hz), 121.27, 115.52 (d, J_{CF} = 3.3 Hz), 109.43 (d, J_{CF} = 20.0 Hz). HRMS (DART): m/z $[M]^{\bullet+}$ calcd for $C_6H_4BrClFN^{\bullet+}$, 222.9194; found, 222.9196.

2,3-Dihydro-1,4-benzodioxine-6-carbonitrile (S23)

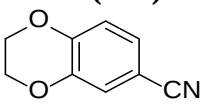

A mixture of 3,4-dihydroxybenzonitrile (**S22**) (3.708 g, 27.4 mmol) in DMF (55 mL) was treated with K_2CO_3 (9.481 g, 68.6 mmol), stirred for 10 min at 23 °C, and treated dropwise with 1-bromo-2-chloroethane (4.57 mL, 54.9 mmol). The mixture was stirred at 23 °C for 1 h, and then at 95 °C for 16 h. The mixture was cooled to 23 °C, diluted with water (200 mL), and extracted with EtOAc

(3 x 125 mL). The combined organics were washed with half-sat. aq. $NaHCO_3$ (100 mL), water (100 mL), brine (100 mL), dried (Na_2SO_4), filtered, and evaporated to give the title compound **S23** (4.178 g, 95%) as a light-brown solid, which was used in the next step without any further purification.

^{1}H NMR (500 MHz, $CDCl_3$): δ 7.16 – 7.12 (m, 2H), 6.91 (dd, J = 8.1, 0.6 Hz, 1H), 4.34 – 4.26 (m, 4H). ^{13}C NMR (126 MHz, $CDCl_3$): δ 147.84, 143.92, 126.07, 121.39, 119.02, 118.38, 104.64, 64.72, 64.25. HRMS (DART): m/z $[M + H]^+$ calcd for $C_9H_8NO_2^+$, 162.0550; found, 162.0542.

7-Nitro-2,3-dihydro-1,4-benzodioxine-6-carbonitrile (S24)

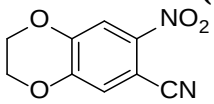

A mixture of carbonitrile **S23** (3.719 g, 23.1 mmol) in AcOH (22.9 mL) was treated at 10 °C with H_2SO_4 (6.4 mL, 120 mmol), cooled to 0 °C, and treated dropwise with 70% HNO_3 (8.2 mL, 120 mmol). The mixture was stirred at 0 °C for 30 min, and then at 23 °C for 10.5 h. The mixture was poured into ice-water (300 mL), and filtered. The residue was washed with water (3 x 30 mL), and dried in a desiccator for 1 h to obtain crude **S24** as a pale-yellow solid. Recrystallization from EtOH gave pure **S24** (3.058 g, 64%) as an off-white powder.

^{1}H NMR (500 MHz, $CDCl_3$): δ 7.86 (s, 1H), 7.33 (s, 1H), 4.41 (s, 4H). ^{13}C NMR (126 MHz, $CDCl_3$): δ 148.41, 146.89, 142.67, 123.87, 115.73, 115.16, 101.22, 64.77, 64.72. HRMS (DART): m/z $[M + H]^+$ calcd for $C_9H_7N_2O_4^+$, 207.0400; found, 207.0399.

7-Amino-2,3-dihydro-1,4-benzodioxine-6-carbonitrile (S25)

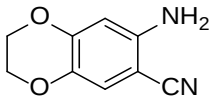

A mixture of carbonitrile **S24** (3.011 mg, 14.6 mmol) in EtOAc (146 mL) under argon was treated with 5% Pd/C (782 mg, 0.37 mmol), and the mixture was stirred under 1 atm (balloon) of hydrogen at 23 °C for 15 h. The mixture was filtered through a plug of Celite (washings with EtOAc), and evaporated to afford the anthranilonitrile **S25** (2.461 mg, 96%) as a yellow solid, which was used in the next step without any further purification.

^{1}H NMR (500 MHz, DMSO-d_6): δ 6.91 (s, 1H), 6.28 (s, 1H), 5.50 (s, 2H), 4.26 – 4.21 (m, 2H), 4.15 – 4.10 (m, 2H). ^{13}C NMR (126 MHz, DMSO-d_6): δ 148.89, 147.37, 134.69, 119.11, 118.03, 102.58, 86.55, 64.82, 63.57. HRMS (DART): *m*/*z* $[M]^{\bullet+}$ calcd for $C_9H_8N_2O_2^{\bullet+}$, 176.0580; found, 176.0578.

4-Chloro(7,7,8,8-$^{2}H_4$)-7,8-dihydro[1,4]dioxino[2,3-*g*]quinazoline (S26)

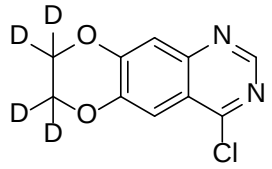

A solution of compound **23** (193 mg, 0.98 mmol) in dry DMF (4.8 mL) was treated with Cs_2CO_3 (788 mg, 2.42 mmol), stirred for 5 min, and treated dropwise with 1-bromo-2-chloro($^{2}H_4$)ethane (270 µL, 3.16 mmol). The mixture was stirred at RT for 1 h, and then at 70 °C for 18 h. After cooling to RT, all volatiles were removed in vacuo. The residue was dissolved in CH_2Cl_2 (40 mL), washed with water (2 x 13 mL), brine (13 mL), dried (Na_2SO_4), filtered, and evaporated. Purification by flash chromatography (CH_2Cl_2/EtOAc 1:0 → 10:1.5) afforded the title compound **S26** (109 mg, 49%) as a white fluffy solid.

^{1}H NMR (400 MHz, $CDCl_3$): δ 8.84 (s, 1H), 7.64 (s, 1H), 7.47 (s, 1H). ^{13}C NMR (101 MHz, $CDCl_3$): δ 160.19, 152.52, 151.54, 147.93, 146.06, 120.10, 113.72, 110.83. HRMS (DART): *m*/*z* $[M + H]^+$ calcd for $C_{10}H_4D_4ClN_2O_2^+$, 227.0520; found, 227.0516.

_N_-(3-Bromo-2-fluorophenyl)(7,7,8,8-$^2H_4$)-7,8-dihydro[1,4]dioxino[2,3-_g_]quinazolin-4-amine (S9)

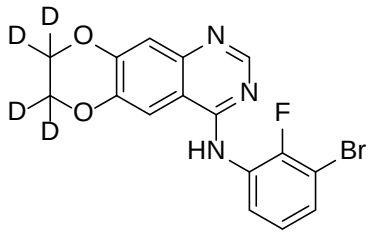

Following general procedure **GP-1**, compound **S9** was prepared from chloroquinazoline **S26** (29 mg, 0.128 mmol) and 3-bromo-2-fluoroaniline (30 µL, 0.267 mmol) in *i*PrOH (1.26 mL). Flash chromatography (CH_2Cl_2/EtOAc 1:0 → 1:1) gave **S9** (38 mg, 78%) as an off-white solid.

^{1}H NMR (500 MHz, DMSO-d_6): δ 9.61 (s, 1H), 8.33 (s, 1H), 7.93 (s, 1H), 7.59 (ddd, J = 7.9, 6.3, 1.6 Hz, 1H), 7.54 (ddd, J = 8.4, 7.1, 1.6 Hz, 1H), 7.21 (td, J = 8.1, 1.2 Hz, 1H), 7.19 (s, 1H). ^{13}C NMR (126 MHz, DMSO-d_6): δ 157.19, 153.37 (d, J = 247.2 Hz), 153.10, 149.27, 146.03, 143.67, 130.12, 128.03 (d, J = 13.0 Hz), 127.74, 125.44 (d, J = 4.2 Hz), 112.47, 109.63, 108.55 (d, J = 19.9 Hz), 108.35. HRMS (DART): m/z $[M + H]^+$ calcd for $C_{16}H_8D_4BrFN_3O_2^+$, 380.0342; found, 380.0327.

4-(3-Bromo-2-fluoroanilino)quinazoline-6,7-diyl bis(2,2-dimethylpropanoate) (S28)

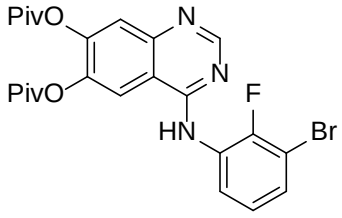

A mixture of 4-chloroquinazoline-6,7-diyl bis(2,2-dimethylpropanoate) (**S27**) (41.08 g, 113 mmol) in *i*PrOH (450 mL) was treated with 3-bromo-2-fluoroaniline (17.05 mL, 152 mmol) and stirred at 80 °C for 3.5 h. The mixture was cooled to 23 °C and evaporated. The residue was several

times resuspended in hexanes (50 mL) and concentrated, and then dried under HV. The residue was recrystallized from EtOH to give a yellow solid, which was suspended in sat. aq. $NaHCO_3$ (1 L), and extracted with CH_2Cl_2 (3 x 550 mL). The combined organics were washed with water (400 mL), brine (400 mL), dried ($MgSO_4$), filtered, and evaporated to afford the title compound **S28** (35.057 g, 60%) as a yellow friable foam.

^{1}H NMR (500 MHz, $CDCl_3$): δ 8.76 (s, 1H), 8.46 (t, J = 7.5 Hz, 1H), 7.72 (s, 1H), 7.68 (s, 1H), 7.56 (br, 1H), 7.32 (ddd, J = 8.0, 6.4, 1.5 Hz, 1H), 7.11 (td, J = 8.2, 1.5 Hz, 1H), 1.40 (s, 9H), 1.39 (s, 9H). ^{13}C NMR (126 MHz, $CDCl_3$): δ 176.13, 175.55, 156.71, 154.96, 150.69 (d, J_{CF} = 243.7 Hz), 148.75, 147.83, 142.45, 128.27, 127.86 (d, J_{CF} = 10.8 Hz), 125.29 (d, J_{CF} = 4.7 Hz), 122.70, 122.51, 114.43, 113.21, 108.84 (d, J_{CF} = 19.4 Hz), 39.54, 39.51, 27.40, 27.32. HRMS (DART): m/z $[M + H]^+$ calcd for $C_{24}H_{26}BrFN_3O_4^+$, 518.1085; found, 518.1072.

4-(3-Bromo-2-fluoroanilino)quinazoline-6,7-diol (S29)

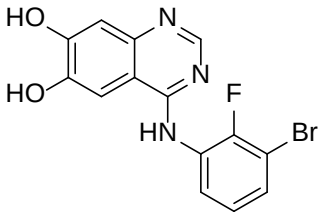

A stirred slurry of **S28** (34.988 g, 67.5 mmol) was treated at 0 °C with 7 M solution of NH_3 in MeOH (241 mL, 1.69 mol). The mixture was stirred at 0 °C for 15 min, and then at 23 °C for 4.5 h. The mixture was evaporated, and the residue suspended in water (400 mL), stirred overnight, and filtered. The residue was washed with water (500 mL), acetonitrile (100 mL), CH_2Cl_2 (4 x 150 mL), Et_2O (2 x 150 mL), and dried in a desiccator to afford the title compound **S29** (23.68 g, quant.) as a pale-yellow powder.

^{1}H NMR (400 MHz, DMSO-d_6): δ 9.38 (br, 1H), 8.26 (s, 1H), 7.61 (s, 1H), 7.59 – 7.48 (m, 2H), 7.18 (t, J = 8.0 Hz, 1H), 7.05 (s, 1H), signals of phenolic protons missing (due to peak broadening). ^{13}C NMR (126 MHz, DMSO-d_6): δ 156.43, 156.12, 153.06 (d, J_{CF} = 246.7 Hz), 151.34, 148.39, 146.80, 129.23, 129.01, 127.12, 125.23 (d, J_{CF} = 4.3 Hz), 108.47, 108.32, 107.09, 103.04. HRMS (DART): m/z $[M + H]^+$ calcd for $C_{14}H_{10}BrFN_3O_2^+$, 349.9935; found, 349.9923.

4-(3-Bromo-2-fluoroanilino)-7-hydroxyquinazolin-6-yl 2,2-dimethylpropanoate (S30)

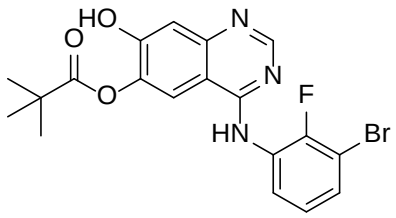

A stirred suspension of **S29** (3500 mg, 10.0 mmol) in DMF (52.6 mL) was treated with Et_3N (5.57 mL, 40.0 mmol), cooled to –40 °C, and treated dropwise with Piv_2O (3.14 mL, 15.5 mmol). The mixture was stirred at –40 °C for 1 h, after which the cooling bath was removed, and stirring was continued for 2.5 h. The reaction mixture was diluted with CH_2Cl_2 (500 mL), washed with 10% citric acid (2 x 50 mL), dried (Na_2SO_4), filtered, and evaporated. Purification by flash chromatography (DCM/EtOAc 1:1 → 0:1) afforded a solid, which was redissolved in EtOAc (750 mL), and washed with half-sat. aq. NH_4Cl (4 x 75 mL), dried (Na_2SO_4), filtered, and evaporated to afford the title compound **S30** (2.844 g, 66%) as a beige-yellow solid.

^{1}H NMR (500 MHz, DMSO-d_6): δ 11.00 (br, 1H), 9.70 (s, 1H), 8.39 (s, 1H), 8.14 (s, 1H), 7.59 (ddd, J = 8.0, 6.2, 1.6 Hz, 1H), 7.53 (ddd, J = 8.3, 7.1, 1.6 Hz, 1H), 7.21 (td, J = 8.1, 1.2 Hz, 1H), 7.17 (s, 1H), 1.36 (s, 9H). ^{13}C NMR (126 MHz, DMSO-d_6): δ 175.93, 157.68, 154.61, 154.53, 153.34 (d, J_{CF} = 247.3 Hz), 149.80, 139.65, 130.14, 127.92 (d, J_{CF} = 12.9 Hz), 127.62, 125.47 (d,

J_{CF} = 4.4 Hz), 116.36, 111.00, 108.55 (d, J = 20.0 Hz), 107.77, 38.64, 26.93. HRMS (DART): m/z $[M + H]^+$ calcd for $C_{19}H_{18}BrFN_3O_3^+$, 434.0510; found, 434.0489.

(±)-4-(3-Bromo-2-fluoroanilino)-7-[(3-oxobutan-2-yl)oxy]quinazolin-6-yl 2,2-dimethylpropanoate (S31)

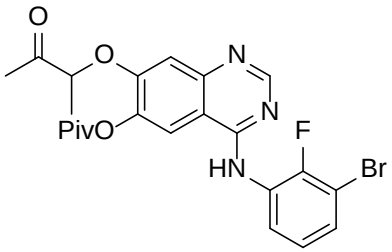

A mixture of **S30** (100 mg, 0.230 mmol) and resin-bound PPh_3 (1% crosslinked with DVB, 100–200 mesh, 1.0–1.5 mmol/g) (480 mg, 0.576 mmol) was swollen in THF (3.4 mL) for 5 min, treated with acetoin (48 µL, 0.553 mmol), cooled to 0 °C, and treated dropwise with DIAD (109 µL, 0.553 mmol). The mixture was stirred at 23 °C for 3 h, diluted with CH_2Cl_2, filtered, and evaporated. Flash chromatography (CH_2Cl_2/EtOAc 1:0 → 6:4) afforded the title compound **S31** (65 mg, 56%) as a white, friable foam.

^{1}H NMR (500 MHz, $CDCl_3$): δ 8.73 (s, 1H), 8.52 (t, J = 7.6 Hz, 1H), 7.58 (s, 1H), 7.49 (br, 1H), 7.32 (ddd, J = 8.1, 6.4, 1.6 Hz, 1H), 7.19 (s, 1H), 7.12 (td, J = 8.2, 1.5 Hz, 1H), 4.82 (q, J = 6.9 Hz, 1H), 2.19 (s, 3H), 1.56 (d, J = 6.8 Hz, 3H), 1.45 (s, 9H). ^{13}C NMR (126 MHz, $CDCl_3$): δ 207.51, 176.68, 156.54, 154.88, 154.25, 150.51 (d, J = 243.3 Hz), 149.95, 141.03, 128.10, 128.01, 125.33 (d, J = 4.7 Hz), 122.35, 114.41, 109.75, 109.61, 108.78 (d, J = 19.5 Hz), 79.93, 39.38, 27.43, 24.91, 17.42. HRMS (DART): m/z $[M + H]^+$ calcd for $C_{23}H_{24}BrFN_3O_4^+$, 504.0929; found, 504.0919.

Diastereoisomeric mixture of (±)-*syn*- and (±)-*anti*-4-(3-Bromo-2-fluoroanilino)-7-[(3-hydroxybutan-2-yl)oxy]quinazolin-6-ol (S32)

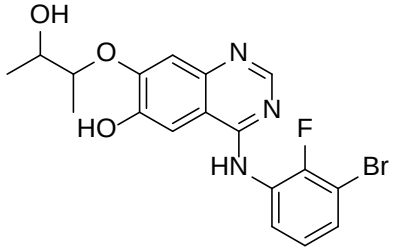

A mixture of **S31** (49 mg, 0.097 mmol) in EtOH (1 mL) was treated with $NaBH_4$ (21 mg, 0.554 mmol), and stirred at 23 °C for 2.5 h. Sat. aq. NH_4Cl (1 mL) was added, and EtOH was removed in vacuo. Half-sat. aq. NH_4Cl (14 mL) was added, and the mixture extracted with EtOAc (3 x 13 mL). The combined organics were dried (Na_2SO_4), filtered, and evaporated. Flash chromatography (EtOAc) afforded a diastereoisomeric mixture (syn/anti ~1:2) of the title compound **S32** (30 mg, 73%) as a yellow solid.

^{1}H NMR (500 MHz, $CDCl_3$; (±)-*syn*/*anti* 1:2): δ 8.59 (s, 0.33H), 8.56 (s, 0.67H), 8.53 – 8.44 (m, 1H), 7.50 (br, 1H), 7.29 – 7.19 (m, 3H), 7.06 (t, J = 8.1 Hz, 1H), 4.56 (qd, J = 6.3, 2.6 Hz, 0.33H), 4.37 (p, J = 6.2 Hz, 0.67H), 4.22 (qd, J = 6.5, 2.7 Hz, 0.33H), 4.02 (p, J = 6.3 Hz, 0.37H), 1.39 – 1.28 (m, 6H). ^{13}C NMR (126 MHz, $CDCl_3$; (±)-*syn*/*anti* 1:2): δ 155.83, 155.81, 152.64, 152.59, 151.92, 151.59, 150.46 (d, J = 243.2 Hz), 147.86, 147.82, 145.96, 145.81, 128.46 (d, J = 10.5 Hz), 128.42 (d, J = 10.5 Hz), 127.63, 127.59, 125.24, 125.20, 122.18, 122.13, 110.28, 109.71, 109.52, 108.72 (d, J = 19.4 Hz), 103.64, 103.49, 80.35, 79.09, 70.86, 69.38, 19.41, 18.09, 15.91, 13.00. HRMS (DART): m/z $[M - H]^-$ calcd for $C_{18}H_{16}BrFN_3O_3^-$, 420.0365; found, 420.0352.

Diastereoisomeric mixture of (±)-*cis*- and (±)-*trans*-*N*-(3-Bromo-2-fluorophenyl)-7,8-dimethyl-7,8-dihydro[1,4]dioxino[2,3-*g*]quinazolin-4-amine ((±)-*cis*/*trans*-S10)

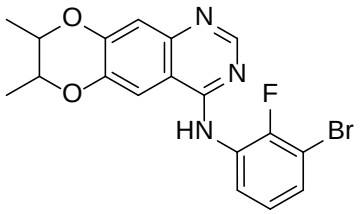

A mixture of PPh_3 (19 mg, 0.071 mmol) and DIAD (13.5 µL, 0.069 mmol) in THF (0.5 mL) was stirred at 0 °C for 15 min, and added dropwise to a mixture of **S32** (25 mg, 0.059 mmol) in THF (0.6 mL) at 0 °C during 5 min. The resulting mixture was stirred at 0 °C for 2 h, and evaporated. Purification by PTLC (hexanes/EtOAc 35:65) afforded a diastereoisomeric mixture (*cis*/*trans* ~2:1) of the title compound **S10** (20 mg, 84%) as a white, friable foam.

^{1}H NMR (500 MHz, $CDCl_3$; (±)-*cis*/*trans* 2:1): δ 8.68 (s, 1H), 8.68 – 8.63 (m, 1H), 7.37 (s, 1H), 7.35 (br, 1H), 7.28 (s, 1H), 7.28 – 7.24 (m, 1H), 7.10 (td, J = 8.2, 1.6 Hz, 1H), 4.52 – 4.39 (m, 1.3H), 4.09 – 3.98 (m, 0.7H), 1.453 (d, J = 6.1 Hz, 1.1H), 1.451 (d, J = 6.1 Hz, 1.1H), 1.369 (d, J = 6.6 Hz, 1.9H), 1.368 (d, J = 6.6 Hz, 1.9H). ^{13}C NMR (126 MHz, $CDCl_3$; (±)-*cis*/*trans* 2:1): δ 155.87, 155.84, 153.19, 150.12 (d, J = 242.5 Hz), 150.09 (d, J = 242.2 Hz), 149.87, 148.89, 146.77, 144.64, 143.63, 128.73 (d, J = 10.0 Hz), 127.15, 127.12, 125.31 (d, J = 4.7 Hz), 121.71, 121.70, 114.30, 113.93, 110.54, 110.47, 108.57 (d, J = 19.4 Hz), 105.66, 105.28, 75.30, 75.05, 72.85, 72.58, 17.24, 17.20, 14.71, 14.55. HRMS (DART): m/z $[M + H]^+$ calcd for $C_{18}H_{16}BrFN_3O_2^+$, 404.0404; found, 404.0393.

REFERENCES

1. Brennan, C. W.; Verhaak, R. G.; McKenna, A.; Campos, B.; Noushmehr, H.; Salama, S. R.; Zheng, S.; Chakravarty, D.; Sanborn, J. Z.; Berman, S. H.; et al. The somatic genomic landscape of glioblastoma. *Cell* **2013,** *155*, 462–477.

2. Fan, Q. W.; Cheng, C. K.; Gustafson, W. C.; Charron, E.; Zipper, P.; Wong, R. A.; Chen, J.; Lau, J.; Knobbe-Thomsen, C.; Weller, M.; et al. EGFR phosphorylates tumor-derived EGFRvIII driving STAT3/5 and progression in glioblastoma. *Cancer Cell* **2013,** *24*, 438–449.

3. Luwor, R. B.; Zhu, H. J.; Walker, F.; Vitali, A. A.; Perera, R. M.; Burgess, A. W.; Scott, A. M.; Johns, T. G. The tumor-specific de2–7 epidermal growth factor receptor (EGFR) promotes cells survival and heterodimerizes with the wild-type EGFR. *Oncogene* **2004,** 23, 6095–6104.

4. Lassman, A. B.; Rossi, M. R.; Razier, J. R.; Abrey, L. E.; Lieberman, F. S.; Grefe, C. N.; Lamborn, K.; Pao, W.; Shih, A. H.; Kuhn, J. G.; et al. Molecular study of malignant gliomas treated with epidermal growth factor receptor inhibitors: tissue analysis from North American Brain Tumor Consortium Trials 01-03 and 00-01. *Clin. Cancer Res.* **2005,** *11*, 7841–7850.

5. Thiessen, B.; Stewart, C.; Tsao, M.; Kamel-Reid, S.; Schaiquevich, P.; Mason, W.; Easaw, J.; Belanger, K.; Forsyth, P.; McIntosh, L.; Eisenhauer, E. A phase I/II trial of GW572016 (lapatinib) in recurrent glioblastoma multiforme: clinical outcomes, pharmacokinetics and molecular correlation. *Cancer Chemother. Pharmacol.* **2010,** *65*, 353–361.

6. Vivanco, I.; Robins, H. I.; Rohle, D.; Campos, C.; Grommes, C.; Nghiemphu, P. L.; Kubek, S.; Oldrini, B.; Chheda, M. G.; Yannuzzi, N.; et al. Differential sensitivity of glioma- versus lung cancer-specific EGFR mutations to EGFR kinase inhibitors. *Cancer Discov.* **2012,** *2*, 458–471.

7. Reardon, D. A.; Nabors, L. B.; Mason, W. P.; Perry, J. R.; Shapiro, W.; Kavan, P.; Mathieu, D.; Phuphanich, S.; Cseh, A.; Fu, Y.; et al. Phase I/randomized phase II study of afatinib, an irreversible ErbB family blocker, with or without protracted temozolomide in adults with recurrent glioblastoma. *Neuro-Oncology* **2014,** *17*, 430–439.

8. Ramos, A.; Hernández-Laín, A.; Balañá, C.; Vicente, E.; Reynés, G.; Benavides, M.; Martínez-García, M.; Quindós, M.; Vaz, M. Á.; Gil-Gil, M.; et al. Phase II trial of dacomitinib, a pan–human EGFR tyrosine kinase inhibitor, in recurrent glioblastoma patients with EGFR amplification. *Neuro-Oncology* **2017,** *19*, 1522–1531.

9. Ballard, P.; Yates, J. W. T.; Yang, Z.; Kim, D.-W.; Yang, J. C.-H.; Cantarini, M.; Pickup, K.; Jordan, A.; Hickey, M.; Grist, M.; et al. Preclinical comparison of osimertinib with other EGFR-TKIs in EGFR-mutant NSCLC brain metastases models, and early evidence of clinical brain metastases activity. *Clin. Cancer Res.* **2016,** *22*, 5130–5140.

10. Freedman, R.A.; Gelman, R.S.; Agar, N.Y.; Santagata, S.; Randall, E.C.; Lopez, B.G.C.; Connolly, R.M.; Dunn, I.F.; Van Poznak, C.H.; Anders, C.K.; et al. Pre-and Postoperative Neratinib for HER2-Positive Breast Cancer Brain Metastases: Translational Breast Cancer Research Consortium 022. *Clin. Breast Cancer* **2019.** DOI: 10.1016/j.clbc.2019.07.011.

11. Finlay, M. R. V.; Ward, R. A. Small molecule inhibitors of the epidermal growth factor receptor. *Top. Med. Chem.* **2018**, *28*, 39–74.

12. Heffron, T. P. Small molecule kinase inhibitors for the treatment of brain cancer. *J. Med. Chem.* **2016,** *59*, 10030–10066.

13. Ghose, A. K.; Herbertz, T.; Hudkins, R. L.; Dorsey, B. D.; Mallamo, J. P. Knowledge-based, central nervous system (CNS) lead selection and lead optimization for CNS drug discovery. *ACS Chem. Neurosci.* **2012,** *3*, 50–68.

14. Wager, T. T.; Chandrasekaran, R. Y.; Hou, X.; Troutman, M. D.; Verhoest, P. R.; Villalobos, A.; Will, Y. Defining desirable central nervous system drug space through the alignment of molecular properties, in vitro ADME, and safety attributes. *ACS Chem. Neurosci.* **2010,** *1*, 420–434.

15. Raub, T. J. P-glycoprotein recognition of substrates and circumvention through rational drug design. *Mol. Pharmaceutics* **2006,** *3*, 3–25.

16. Broniscer, A.; Panetta, J. C.; O'Shaughnessy, M.; Fraga, C.; Bai, F.; Krasin, M. J.; Gajjar, A.; Stewart, C. F. Plasma and cerebrospinal fluid pharmacokinetics of erlotinib and its active metabolite OSI-420. *Clin. Cancer Res.* **2007,** *13*, 1511–1515.

17. Denny, W. A. The 4-anilinoquinazoline class of inhibitors of the erbB family of receptor tyrosine kinases. *Il Farmaco* **2001,** *56*, 51–56.

18. Stamos, J.; Sliwkowski, M. X.; Eigenbrot, C. Structure of the epidermal growth factor receptor kinase domain alone and in complex with a 4-anilinoquinazoline inhibitor. *J. Biol. Chem.* **2002,** *277*, 46265–46272.

19. Barker, A. J.; Zeneca Pharmaceuticals. Quinazoline derivatives. Eur. Pat. Appl. 0566226, 1993.

20. Ballard, P.; Bradbury, R. H.; Harris, C. S.; Hennequin, L. F.; Hickinson, M.; Kettle, J. G.; Kendrew, J.; Klinowska, T.; Ogilvie, D. J.; Pearson, S. E.; et al. Inhibitors of epidermal growth factor receptor tyrosine kinase: optimisation of potency and in vivo pharmacokinetics. *Bioorg. Med. Chem. Lett.* **2006,** *16*, 4908–4912.

21. Zeng, Q.; Wang, J.; Cheng, Z.; Chen, K.; Johnström, P.; Varnäs, K.; Li, D. Y.; Yang, Z. F.; Zhang, X. Discovery and evaluation of clinical candidate AZD3759, a potent, oral active, central nervous system-penetrant, epidermal growth factor receptor tyrosine kinase inhibitor. *J. Med. Chem.* **2015,** *58*, 8200–8215.

22. Böhm, H. J.; Banner, D.; Bendels, S.; Kansy, M.; Kuhn, B.; Müller, K.; Obst-Sander, U.; Stahl, M. Fluorine in medicinal chemistry. *ChemBioChem* **2004,** *5*, 637–643.

23. Müller, K.; Faeh, C.; Diederich, F. Fluorine in pharmaceuticals: looking beyond intuition. *Science* **2007,** *317*, 1881–1886.

24. Wilcken, R.; Zimmermann, M. O.; Bauer, M. R.; Rutherford, T. J.; Fersht, A. R.; Joerger, A. C.; Boeckler, F. M. Experimental and theoretical evaluation of the ethynyl moiety as a halogen bioisostere. *ACS Chem. Biol.* **2015,** *10*, 2725–2732.

25. Lee, J. Y.; Park, Y. K.; Seo, S. H.; So, I.-S.; Chung, H.-K.; Yang, B.-S.; Lee, S.-J.; Park, H.; Lee, Y. S. 1,4-Dioxane-fused 4-anilinoquinazoline as inhibitors of epidermal growth factor receptor kinase. *Arch. Pharm. Pharm. Med. Chem.* **2001,** *334*, 357–360.

26. Cha, M. Y.; Lee, K. O.; Kim, M.; Song, J. Y.; Lee, K. H.; Park, J.; Chae, Y. J.; Kim, Y. H.; Suh, K. H.; Lee, G. S.; et al. Antitumor activity of HM781-36B, a highly effective pan-HER inhibitor in erlotinib-resistant NSCLC and other EGFR-dependent cancer models. *Int. J. Cancer* **2012,** *130*, 2445–2454.

27. Szafraniec, M. J.; Szczygieł, M.; Urbanska, K.; Fiedor, L. Determinants of the activity and substrate recognition of breast cancer resistance protein (ABCG2). *Drug Metab. Rev.* **2014,** *46*, 459–474.

28. O'Brien, Z.; Moghaddam, M. F. A systematic analysis of physicochemical and ADME properties of all small molecule kinase inhibitors approved by US FDA from January 2001 to October 2015. *Curr. Med. Chem.* **2017,** *24*, 3159–3184.

29. Gao, H.; Korn, J. M.; Ferretti, S.; Monahan, J. E.; Wang, Y.; Singh, M.; Zhang, C.; Schnell, C.; Yang, G.; Zhang, Y.; et al. High-throughput screening using patient-derived tumor xenografts to predict clinical trial drug response. *Nat. Med.* **2015,** *21*, 1318–1325.

30. Spilker, M. E.; Chen, X.; Visswanathan, R.; Vage, C.; Yamazaki, S.; Li, G.; Lucas, J.; Bradshaw-Pierce, E. L.; Vicini, P. Found in translation: maximizing the clinical relevance of nonclinical oncology studies. *Clin. Cancer Res.* **2017,** *23*, 1080–1090.

31. Ling, J.; Johnson, K. A.; Miao, Z.; Rakhit, A.; Pantze, M. P.; Hamilton, M.; Lum, B. L.; Prakash, C. Metabolism and excretion of erlotinib, a small molecule inhibitor of epidermal growth factor receptor tyrosine kinase, in healthy male volunteers. *Drug Metab. Dispos.* **2006,** *34*, 420–426.

32. Burris III, H. A.; Taylor, C. W.; Jones, S. F.; Koch, K. M.; Versola, M. J.; Arya, N.; Fleming, R. A.; Smith, D. A.; Pandite, L.; Spector, N.; Wilding; G. A phase I and pharmacokinetic study of oral lapatinib administered once or twice daily in patients with solid malignancies. *Clin. Cancer Res.* **2009**, *15*, 6702–6708.

33. Mai, W. X.; Gosa, L.; Daniels, V. W.; Ta, L.; Tsang, J. E.; Higgins, B.; Gilmore, W. B.; Bayley, N. A.; Harati, M. D.; Lee, J. T.; et al. Cytoplasmic p53 couples oncogene-driven

glucose metabolism to apoptosis and is a therapeutic target in glioblastoma. *Nat. Med.* **2017,** *23*, 1342–1351.

34. Randall, E. C.; Emdal, K. B.; Laramy, J. K.; Kim, M.; Roos, A.; Calligaris, D.; Regan, M. S.; Gupta, S. K.; Mladek, A. C.; Carlson, B. L.; et al. Integrated mapping of pharmacokinetics and pharmacodynamics in a patient-derived xenograft model of glioblastoma. *Nat. Commun.* **2018,** *9*, 4904.

35. Park, J. H.; Liu, Y.; Lemmon, M. A.; Radhakrishnan, R. Erlotinib binds both inactive and active conformations of the EGFR tyrosine kinase domain. *Biochem. J.* **2012,** *448*, 417–423.

36. Wood, E. R.; Truesdale, A. T.; McDonald, O. B.; Yuan, D.; Hassell, A.; Dickerson, S. H.; Ellis, B.; Pennisi, C.; Horne, E.; Lackey, K.; et al. A unique structure for epidermal growth factor receptor bound to GW572016 (Lapatinib): relationships among protein conformation, inhibitor off-rate, and receptor activity in tumor cells. *Cancer Res.* **2004,** *64*, 6652–6659.

37. Chilin, A.; Conconi, M. T.; Marzaro, G.; Guiotto, A.; Urbani, L.; Tonus, F.; Parnigotto, P. Exploring epidermal growth factor receptor (EGFR) inhibitor features: the role of fused dioxygenated rings on the quinazoline scaffold. *J. Med. Chem.* **2010,** *53*, 1862–1866.

38. O'Connor, M.; Zhang, J.; Markovic, S.; Romashko, D.; Salomatov, A.; Ishiyama, N.; Iacone, R.; Flohr, A.; Nicolaides, T.; Mayweg, A.; et al. EGFR Oncogenes Expressed In Glioblastoma Are Activated As Covalent Dimers And Paradoxically Stimulated By Erlotinib. *bioRxiv* **2019,** 810721.

39. Yoshikawa, S.; Kukimoto-Niino, M.; Parker, L.; Handa, N.; Terada, T.; Fujimoto, T.; Terazawa, Y.; Wakiyama, M.; Sato, M.; Sano, Kobayashi, T.; Tanaka, T.; Chen, L.; Liu, Z. J.; Wang, B. C.; Shirouzu, M.; Kawa, S.; Semba, K.; Yamamoto, T.; Yokoyama, S. Structural basis for the altered drug sensitivities of non-small cell lung cancer-associated mutants of human epidermal growth factor receptor. *Oncogene* **2013,** *32*, 27–38.

40. Bridges, A. J. Chemical inhibitors of protein kinases. *Chem. Rev.* **2001,** *101*, 2541–2571.

41. Bridges, A. J., Zhou, H.; Cody, D. R.; Rewcastle, G. W.; McMichael, A.; Showalter, H. D. H.; Fry, D. W. K., A. J.; Denny, W. A. Tyrosine kinase inhibitors. 8. An unusually steep structure–activity relationship for analogues of 4-(3-bromoanilino)-6,7-dimethoxyquinazoline (PD 153035), a potent inhibitor of the epidermal growth factor receptor. *J. Med. Chem.* **1996,** *39*, 267–276.

42. Costales, A.; Mathur, M.; Ramurthy, S.; Lan, J.; Subramanian, S.; Jain, R.; Atallah, G.; Setti, L.; Lindvall, M.; Appleton, B. A.; Ornelas, E.; Feucht, P.; Warne, B.; Doyle, L.; Basham, S. E.; Aronchik, I.; Jefferson, A. B.; Shafer, C. M. 2-Amino-7-Substituted Benzoxazole Analogs as Potent RSK2 Inhibitors. *Bioorg. Med. Chem. Lett.* **2014**, *24*, 1592–1596.

43. Dai, H.; Marbach, P.; Lemaire, M.; Hayes, M.; Elmquist, W. F. Distribution of STI-571 to the brain is limited by P-glycoprotein-mediated efflux. *J. Pharmacol. Exp. Ther.* **2003,** *304*, 1085–1092.

44. Tannous, B. A. Gaussia luciferase reporter assay for monitoring biological processes in culture and in vivo. *Nat. Protoc.* **2009,** 4, 582–591.

45. Berman, H. M.; Westbrook, J.; Feng, Z.; Gilliland, G.; Bhat, T. N.; Weissig, H.; Shindyalov, I. N.; Bourne, P. E. The Protein Data Bank. *Nucleic Acids Res.* **2000,** *28*, 235–242.

46. Morris, G. M.; Huey, R.; Lindstrom, W.; Sanner, M. F.; Belew, R. K.; Goodsell, D. S.; Olson, A. J. AutoDock4 and AutoDockTools4: Automated docking with selective receptor flexibility. *J. Comput. Chem.* **2009,** *30*, 2785–2791.

47. Trott, O.; Olson, A. J. AutoDock Vina: improving the speed and accuracy of docking with a new scoring function, efficient optimization, and multithreading. *J. Comput. Chem.* **2010,** *31*, 455–461.

48. Juvale, K.; Gallus, J.; Wiese, M. Investigation of Quinazolines as Inhibitors of Breast Cancer Resistance Protein (ABCG2). *Bioorg. Med. Chem.* **2013**, *21*, 7858–7873.

49. Jyothi Prasad, R.; Nageshwar Rao, B.; Venkaiah Chowdary, N. A Novel Process for the Preparation of Erlotinib. PCT Int. Appl. WO 2007/060691 A2, May 31, 2007.

50. Harris, C. S.; Hennequin, L. F.; Willerval, O. Three-point Variation of a Gefinitib Quinazoline Core. *Tetrahedron Lett.* **2009**, *50*, 1600–1602.

51. Arnott, E. A.; Chan, L. C.; Cox, B. G.; Meyrick, B.; Phillips, A. $POCl_3$ Chlorination of 4-Quinazolones. *J. Org. Chem.* **2011**, *76*, 1653–1661.

52. Li, L.; Feng, J.; Long, Y. O.; Liu, Y.; Wu, T.; Ren, P.; Liu, Y. Substituted Quinazoline Compounds and Methods of Use Thereof. PCT Int. Appl. WO 2016/164675 A1, October 13, 2016.

53. Huang, S.; Jin, X.; Liu, Z.; Poon, D.; Tellew, J.; Wan, Y.; Wang, X.; Xie, Y. Compounds and Compositions as Protein Kinase Inhibitors. PCT Int. Appl. WO 2011/025927 A1, March 3, 2011.

CHAPTER 2: Development and Evaluation of JCN068, a Novel Highly Brain-Penetrant EGFR Tyrosine Kinase Inhibitor for Glioblastoma

INTRODUCTION

Brain cancers are highly invasive and despite surgical and medical advances, the prognosis of most brain cancer patients remains dismal. Despite being one of the rarest cancers with less than 200,000 patients and responsible for only 1% of all cancer cases in the United States, brain cancers are among the most lethal cancers (Figure 1A-B).[1] Due to new and improving treatments, the majority of cancers have had a steady improvement in survival rates and mortality rates (Figure 1C-H), however, brain cancers have been left behind and remain unchanged. Within brain cancers, glioblastoma multiforme (GBM) is the most common and the most malignant form, accounting for approximately half of all brain cancers with a median survival rate of 12-15 months.[2] Even with standard of care consisting of surgical resection followed by radiation with concomitant temozolomide chemotherapy, 5-year survival rates in GBM remains below 10%.[3] With only a few approved therapies for GBM and a stagnant survival outlook there is a desperate need for new and effective therapies for GBM.

In GBM, comprehensive genetic analysis has revealed that the majority of tumors harbor an alteration in EGFR with either mutations and/or copy number gains. Approximately 60% of GBM tumors have either an amplification (~25%) and/or mutation (~35%) of EGFR.[4] Moreover, ~35% of GBM patients have copy number gains in EGFR via polysomy of chromosome 7 (Figure 2). Unlike non-small cell lung cancer (NSCLC), where EGFR alterations consist of mutations occur in the kinase domain of the receptor, EGFR alterations in GBM occur as an amplification and/or copy number gains without a mutation (i.e. WT EGFR), or extracellular domain (ECD) mutations such as the EGFR exon 2-7 deletion (EGFRvIII) and missense mutations.[5]

These EGFR alterations have been well documented to be an oncogenic driver of GBM growth and metabolism in multiple *in vitro* and *in vivo* patient-derived model systems.[5-8] As such,

with the high frequency and oncogenicity of the EGFR alterations seen in GBM, several clinical trials have been performed using numerous EGFR tyrosine kinase inhibitors (TKI) (i.e. erlotinib, lapatinib, gefitinib, afatinib) that have been widely successful in treating lung cancer. However, despite significant evidence indicating that EGFR is important in GBM, none of the clinical trials using EGFR TKIs have improved patient outcomes.[9-12] These trials suggested several reasons for their failures but commonly proposed that these 1st generation EGFR TKIs have limited efficacy against the oncogenic forms of EGFR in GBM since they were re-purposed from NSCLC and that they do not cross the blood-brain barrier (BBB) in concentrations sufficient to achieve therapeutic outcomes in GBM tumors.

Unlike NSCLC, the activating mutations in the EGFR kinase domain which are favored by these EGFR TKI, are rarely found in GBM. Instead, WT EGFR amplification, EGFRvIII variant, and ECD missense mutations commonly occur and are known to promote tumor growth.[13-15] Interestingly, when EGFRvIII is co-expressed with WT EGFR, EGFRvIII can be activated by WT EGFR.[7] These distinct oncogenic forms of EGFR in GBM have been found to affect EGFR TKI affinity.[5,16] Type I EGFR TKIs used in NSCLC (i.e. erlotinib, gefitinib) preferentially target amplified WT EGFR and EGFR kinase domain mutants, but have poor activity against ECD mutant EGFR. Conversely, type II EGFR inhibitors used for breast cancer (i.e. lapatinib, neratinib) have higher affinity against ECD mutations, but lower activity against both amplified WT EGFR and kinase domain mutants. Since GBM is driven by mutations in the ECD of EGFR and an amplification of WT EGFR, there is a clinical need for novel EGFR TKIs that can robustly target the distinct forms of EGFR that drive GBM.

The BBB is a physical and biological barrier lining the capillaries in the brain that facilitates the transport of essential nutrients while protecting the brain from foreign objects such

as toxic compounds, viruses, and bacteria. Several mechanisms that selectively allow passage through the BBB include passive paracellular pathway, transcellular lipophilic pathway, receptor-mediated transcytosis, adsorptive transcytosis, and efflux transporters.[17] As a result, these specific regulations result in the inability of 98% of therapeutic compounds to cross the BBB, preventing effective brain delivery of therapeutics.[18] Several physicochemical parameters are involved in the ability of drugs to cross the BBB such as molecular weight, charge, number of hydrogen bond donors and acceptors, polar surface area, number of rotatable bonds, and interaction with efflux pumps and transporters.[19-21] Importantly, all of the EGFR TKIs tested clinically against GBM exhibit low brain to plasma ratios (<10%) which results in sub-optimal concentrations of the drugs in the tumor.[22] In patient GBM tumors, EGFR activation and downstream signaling were not significantly reduced in patients treated with erlotinib and gefitinib, suggesting tumor EGFR TKI concentrations were insufficient and responsible for their lack of therapeutic efficacy.[9,23] Although the EGFR TKIs osimertinib and AZD3759 – both developed for EGFR-mutated NSCLC – have reported high brain penetration, they have yet to be evaluated clinically for GBM.[24,25] Accordingly, there is an urgent need for an EGFR TKI that can both penetrate the brain to levels that are sufficient to inhibit EGFR-driven GBMs and target the forms of EGFR that drive GBM. As such, we have developed JCN068 by performing further modifications of the 1,4-dioxane ring of JCN037 to further improve potency against oncogenic forms of EGFR found in GBM, specificity, brain penetration, and *in vivo* pharmacology.[26] JCN068 is highly effective both in *in vitro* EGFR amplified/mutant patient-derived cell cultures as well as in multiple EGFR-driven orthotopic glioblastoma xenograft models.

RESULTS

The most common oncogenic forms of EGFR found in GBM consists of amplified WT EGFR, EGFRvIII, and EGFR ECD mutants. To thoroughly evaluate JCN068 in GBM, we first profiled JCN068 in comparison with a Type 1 (i.e. erlotinib) and a Type 2. (i.e. lapatinib) in U87 cells transduced with either overexpression of WT EGFR, EGFRvIII, or a EGFR ECD mutant (A289D) (Figure 4A). As expected of a Type 1 EGFR TKI, erlotinib more efficiently inhibited WT EGFR but lapatinib had a higher affinity for EGFRvIII and the EGFR ECD mutant.[5,16] Surprisingly, JCN068 was on par with or better than either erlotinib or lapatinib at inhibiting all of the oncogenic forms of EGFR found in GBM with an pEGFR IC_{50} of 1.13nM, 2.50nM, and 1.09nM in WT EGFR, EGFRvIII and EGFR A289D ECD mutant, respectively (Figure 4B-C). Additional immunoblots of other ECD mutants transduced into the U87 GBM cell culture model and the brain penetrant EGFR TKIs, osimertinib and AZD3759, were also quantified and summarized in Table 1.

Next, the EGFR TKIs erlotinib, lapatinib, JCN068, osimertinib, and AZD3759 were treated at half-log increments in a WT EGFR amplified and EGFRvIII patient-derived gliomasphere model, HK301 (Figure 5A), and an EGFR A289D ECD mutant patient-derived gliomasphere model, GS187 (Figure 5B). Relative to lapatinib, erlotinib more efficiently inhibited pWT EGFR in HK301 but fared worse against pEGFRvIII in HK301 and pEGFR A289D in GS187. JCN068 more potently inhibited pWT EGFR and pEGFRvIII in the HK301 model than either osimertinib or AZD3759. Similarly, JCN068 also outperformed both EGFR TKIs against pEGFR A289D. Downstream signaling of pERK and pS6 followed similar patterns to the pEGFR status for all of the EGFR TKIs in both patient-derived gliomasphere models.

Knowing JCN068 can potently inhibit the forms of EGFR found in GBM, we next wanted to determine its specificity. Kinome profiling was performed at 10μM across 485 wild-type and mutant kinases (Thermofisher) (Figure 6A). JCN068 strongly (>80%) inhibited 12 wild-type kinases and most EGFR kinase domain mutants with few off-target kinases, resulting in a kinase selectivity score of 0.04 (Table S1).[27] A follow-up kinase IC_{50} profiling was then performed on the strongly inhibited kinases and determined a purified kinase IC_{50} of 0.454nM, 187nM, 490nM, 569nM, 613nM, 864nM, 1090nM, 1230nM, 1540nM, and 1890nM, for EGFR, HER2, LYN B, LYN A, HER4, RIPK3, GAK, EPHB2, RIPK2, and DRAK1, respectively (Figure 6B). Interestingly, the IC_{50} for EGFR was over 400-fold better than the next closest kinase, HER2. Compared to a non-HER family kinase, EGFR was over 1000-fold more selective for EGFR than LYN B.

We then evaluated JCN068, erlotinib, lapatinib, and osimertinib against a panel of 40 patient-derived gliomaspheres and normal human astrocytes (NHA). Stratifying by copy number status of EGFR identifies EGFR amplified gliomaspheres to be the most sensitive to EGFR TKI and JCN068 to be more potent at inhibiting growth than both erlotinib and lapatinib (Figure 7A). Interestingly, a large spread of sensitivity to EGFR TKIs was observed for chromosome 7 polysomy gliomaspheres, suggesting some polysomy gliomaspheres are as sensitive to EGFR TKIs as EGFR amplified tumors. As NHAs are not dependent on EGFR for growth, they were used as a proxy for normal cell toxicity to determine the therapeutic index of each gliomasphere relative to NHAs (Figure 7B).[26] Both JCN068 and erlotinib had large therapeutic indexes, however, osimertinib's therapeutic index across all gliomaspheres remained low due to the high toxicity observed by us and reported by others at around 2000nM.[28]

Having identified JCN068 as a potent, specific inhibitor of the variants of EGFR seen in GBM, we next wanted to ascertain its *in vivo* pharmacokinetics and brain penetration. Upon a single 10mg/kg oral dose in CD-1 male mice, JCN068 achieved moderate plasma concentrations with an exposure of 11977nM·hr and very high brain concentrations with an exposure of 44246nM·hr (Figure 8A-B). At the same dose, JCN068 optimally reached significantly lower plasma exposures while attaining over 16-fold higher brain exposures compared to erlotinib. This resulted in a ~370% brain to plasma ratio for JCN068, 8.54% for erlotinib, and 1.85% for lapatinib, which were in-line with reported brain to plasma ratios (Figure 8C).[29,30] The Kp_{uu}, which is ratio of the free, unbound drug concentrations of JCN068 in the brain relative to the plasma was 1.30, indicating the drug is approximately equal across the BBB.[31,32] These unbound drug exposures was found to be above its GI_{50} of GBM tumors for JCN068, but insufficient for both erlotinib and lapatinib and may explain their lack of efficacy (Figure 8D). The pharmacokinetics was then confirmed in Hans-Wistar rats with a further improved brain to plasma ratio in rats of 473.5% (Figure 8E). With a high brain penetration, JCN068 is hypothesized to not be a substrate for drug efflux transporters such as the P-glycoprotein (P-gp) found along the BBB.[33] As assessed by an *in vitro* cell permeability and P-gp substrate status by transwell culture with MDCK-MDR1 cells, JCN068 has an efflux ratio of 0.92 and is therefore not a substrate of the P-gp (Figure 8F).

Knowing JCN068 can robustly inhibit EGFR *in vitro*, we next wanted to examine how effective it is in an *in vivo* setting. Due to the strong inhibitory effect JCN068 had *in vitro*, coupled with the high degree of brain penetration, we hypothesized JCN068 would significantly inhibit EGFR signaling *in vivo* in an in intracranial model. The EGFRvIII mutant GBM39 patient-derived gliomasphere model was intracranially implanted into the brains of of NOD-SCID Gamma (NSG) mice.[34] When tumors reached exponential growth, as determined by secreted gaussia luciferase,[35]

mice were administered 10 mg/kg, 25 mg/kg, or 75 mg/kg of JCN068 or vehicle by oral gavage. At a 1 hour time point, the intracranial tumors were harvested, lysed, and subjected to immunoblotting for activation of EGFRvIII and its downstream signaling effectors (Figure 9A). In comparison to vehicle treated tumors, JCN068 treatment at all doses showed a significant decrease in pEGFRvIII and pWT EGFR activity in a dose-dependent manner (Figure 9B). Downstream signaling pathways of EGFR, including RAS-MAPK (via p-ERK) or PI3K-AKT-mTOR (via pS6) signaling, was also associated with the decrease in pWT EGFR and pEGFRvIII activity. These data support the hypothesis that the high BBB penetration and potent EGFR inhibitory efficacy of JCN068 would result in an effective inhibition of EGFR signaling in an orthotopic GBM xenograft model.

With the pharmacodynamic effect of JCN068 in GBM tumors having been established, we next hypothesized that the significant decrease in EGFR and downstream EGFR signaling activity would lead to a significant tumor growth inhibition and survival benefit. The EGFRvIII mutant GBM39 patient-derived orthotopic xenograft model was intracranially implanted. After tumors reached exponential growth, mice were randomized into vehicle, 10 mg/kg JCN068, 25 mg/kg JCN068, or 75 mg/kg JCN068 treatment groups. Mice were treated daily for 5 days followed by 2 days of no treatment by oral gavage until euthanasia. At the measurement closest to median survival of the vehicle, tumor growth inhibition (TGI) was calculated using the secreted gaussian luciferase reporter (Figure 10A). A significant TGI of 94.2%, 96.6%, and 98.7% (p-value <0.05) was observed in mice treated with 10 mg/kg JCN068, 25 mg/kg JCN068, and 75 mg/kg JCN068, respectively, with no significant loss in body weight or other observable side effects (Figure S1). Moreover, JCN068 treatment provided a significant survival benefit, with the vehicle, 10 mg/kg JCN068, 25 mg/kg JCN068, and 75 mg/kg JCN068 reaching median survivals of 39 days, 63.5

days, 76 days, and 81 days, respectively (Figure 10B). This corresponded with an increase in median survival of +62.8%, +94.9%, and +107.7% compared to vehicle. To approximate the clinically relevant dose of JCN068, we identified the dose of erlotinib and lapatinib in which the plasma exposures in mice matches to that of human plasma levels at the standard clinical dose.[36-38] Erlotinib and lapatinib administered at 10 mg/kg and 80 mg/kg in non-tumor bearing mice reached plasma exposures of 51,689 nM·hr and 44,807 nM·hr over 24 hours, respectively; which, mirrors the 24-hour human clinical plasma exposures for both drugs.[26,39,40] Based on our pharmacokinetic experiments (Figure S2), we found JCN068 at 25 mg/kg to reach a 24-hour exposure of 42905 nM·hr.

Using the 25 mg/kg dose, we then evaluated JCN068 in a "preclinical trial" against a large cohort (n=20) of clinically relevant orthotopic GBM patient-derived xenograft models to assess both the breadth of response and molecular determinants of response to JCN068. JCN068 was found to be efficacious against the majority of EGFR amplified and EGFR mutated orthotopic GBM patient-derived xenograft models with also efficacy against approximately 40% of chromosome 7 polysomy orthotopic GBM patient-derived xenograft models (Figure 10C). Importantly, osimertinib has reported brain penetration and significant activity against NSCLC with EGFR kinase domain mutants that have metastasized to the brain.[25,41] Given these properties, and some early but inconclusive preclinical and clinical work with osimertinib in GBM, we directly compared JCN068 against osimertinib in several EGFR-altered orthotopic GBM patient-derived xenograft models.[42,43] We found that JCN068 was superior at prolonging the survival of all EGFR-altered orthotopic GBM patient-derived xenograft models (Figure 10C). These intriguing data may result from not only the higher brain penetration and exposure of JCN068 relative to osimertinib (JCN068 Kpuu = 1.30 and osimertinib Kpuu = 0.39)[25], but also the increased

potency of JCN068 against the oncogenic forms of EGFR that are unique to GBM (Table 2, Figure 5). Collectively, these data support that JCN068 is a highly brain penetrant GBM-targeting EGFR TKI, with considerable single agent efficacy against numerous EGFR-altered orthotopic GBM patient-derived xenograft models.

Although the genetic status of EGFR in GBM is a relatively good predictor of response to JCN068, it cannot stratify tumors that are polysomy for chromosome 7. However, EGFR is a strong driver of glucose metabolism through EGFR-mediated activation of PI3K-AKT-mTOR and RAS-MAPK to increase the expression and translocation of glucose transporters and Hexokinase 2.[8,34,44] Given, this relationship between EGFR signaling and glucose metabolism, and that JCN068 can potently inhibit EGFR signaling in vivo, we hypothesized that JCN068 would efficiently inhibit glucose metabolism *in vivo*. Using ^{18}F-fluorodeoxyglucose positron emission tomography (^{18}F-FDG PET), we performed delayed imaging[45] on orthotopic GBM patient-derived xenograft models that JCN068 treatment provided a survival benefit and ones that it did not (Figure 11A-B). The GBM tumors in which glucose metabolism is rapidly reduced with 3 days of JCN068 treatment lead to significant growth inhibition and a survival benefit (Figure 11A). Conversely, in GBM tumors without a change in glucose metabolism with JCN068 treatment, a therapeutic response was not observed relative to vehicle (Figure 11B). Importantly, the survival benefit response to JCN068 treatment could not be predicted by EGFR alteration status alone (p-value = 0.42) (Figure 11C). However, the ^{18}F-FDG PET response was able to significantly predict the survival outcome in response to JCN068 treatment (Figure 11D). This suggests that rapid changes in ^{18}F-FDG PET can serve as a non-invasive approach to predict both successful inhibition of EGFR signaling and therapeutic outcome *in vivo*.

DISCUSSION

Here we evaluated JCN068 and found that it potently inhibits the oncogenic forms of EGFR commonly found in GBM—amplified WT EGFR, EGFRvIII, and EGFR ECD mutants—in both synthetic U87 model systems and in patient-derived model systems. Furthermore, JCN068 was also able to induce inhibition of EGFR downstream signaling in patient-derived models better or on par with other EGFR TKIs. Consequently, JCN068 could robustly inhibit growth of multiple EGFR-altered primary GBM cells better than erlotinib and lapatinib. Importantly, the high potency of JCN068 did not compromise selectivity. Firstly, relative to an EGFR-altered GBM cell, 100-fold more JCN068 was required to inhibit growth of a non EGFR-dependent normal human astrocytes (NHA). Moreover, kinome profiling of JCN068 confirmed this high selectivity, with a nearly 400-fold difference between the IC_{50} for EGFR (0.454 nM) and with any other kinases (HER2 IC_{50}: 180 nM) and over 1000-fold selectivity for EGFR over the nearest non-HER kinase (LYNB IC_{50}: 490nM).

JCN068 was developed from previous work on JCN037 and further improved upon multiple properties including potency, specificity, brain penetration, efficacy, and *in vivo* pharmacokinetics.[26] With a brain to plasma ratio of ~400% and a Kp_{uu} of 1.30, JCN068 can effectively cross the BBB and reach the tumor. Pharmacodynamic studies of EGFR activation and downstream signaling supports the hypothesis that the high BBB penetration and potent EGFR inhibitory efficacy of JCN068 would result in an effective inhibition of EGFR activation and EGFR signaling. This, in turn, led to an improvement in survival outcomes of mice orthotopically implanted with EGFR-altered patient-derived gliomaspheres. Collectively, these data support the suggestion that EGFR TKIs made specifically for GBM can improve on currently available EGFR TKIs made for other indications. In addition, given the desirable properties of JCN068 as a GBM-

targeted EGFR TKI, we have shown an acute response in ^{18}F-FDG PET can be used as a rapid predictive biomarker of response to JCN068 in patient-derived orthotopic xenograft models. From these data, we found that JCN068 could significantly reduce ^{18}F-FDG uptake and this rapid change in glucose metabolism with drug treatment was an effective in predicting outcome. This can be used as a non-invasive, functional biomarker of response that can be easily translated to clinical use and aid patient selection.[46,47]

Taken together, these compelling data indicate that JCN068 is a GBM-targeting EGFR TKI, with potent single agent efficacy against numerous EGFR-altered patient-derived orthotopic xenograft models. Our data supports that ^{18}F-FDG PET may serve as a robust companion predictive biomarker of response to JCN068. Finally, JCN068 shows favorable specificity, selectivity, toxicity profile, oral bioavailability, distribution, metabolism. Consequently, JCN068 is currently in pre-IND studies with an anticipation to begin dosing patients in late 2021.

FIGURES AND TABLES

Chapter 2 – Figure 1.

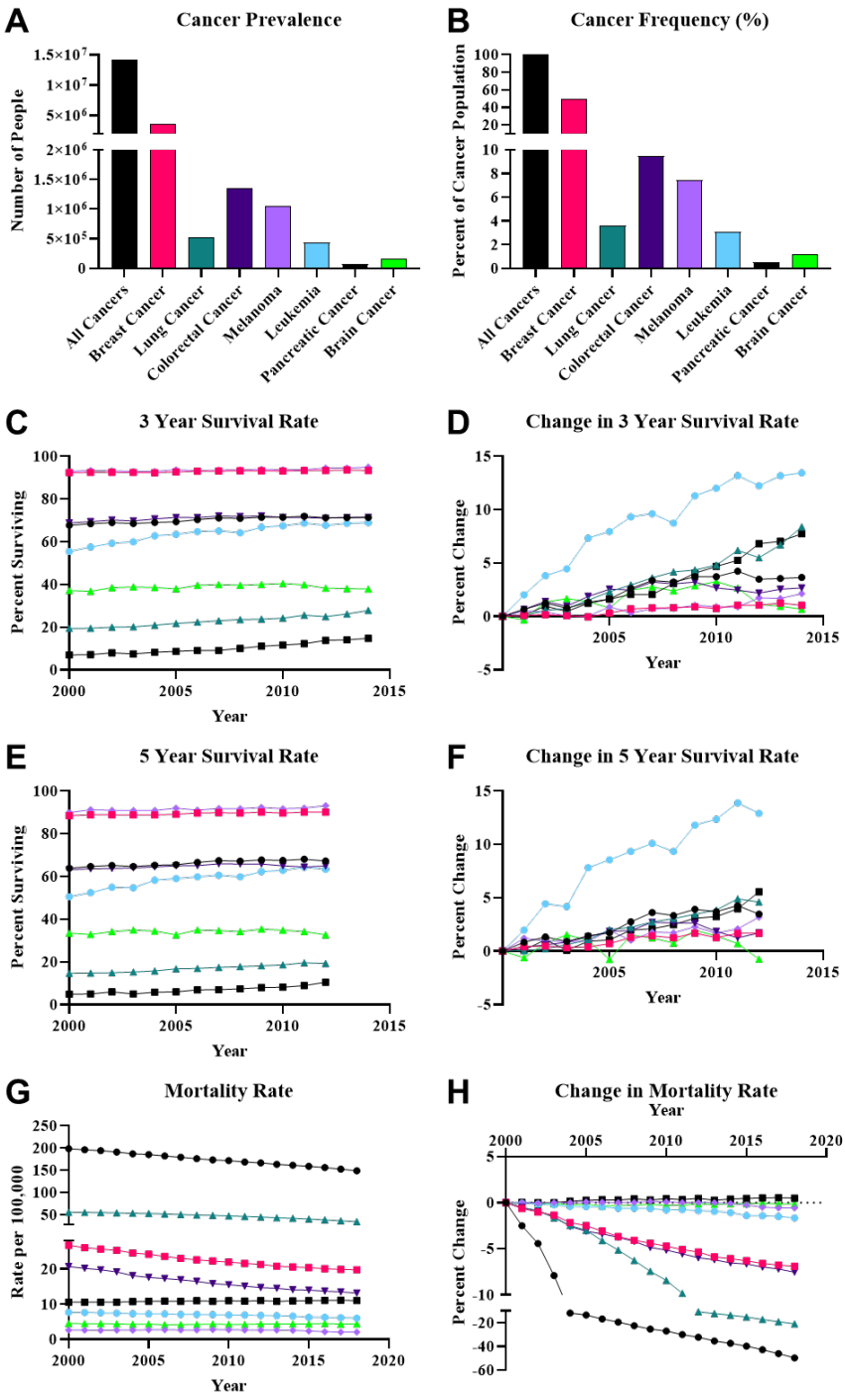

Figure 1. Cancer statistics of all combined cancers and selected common cancers. Data generated from the SEER*Explorer.[1] (A) Cancer prevalence of the number of patients with each respective cancer type in the United States as of 2018 data. (B) Cancer frequency as a percent of all patients alive with cancer as of 2018. (C) 3-year survival rate of the same set of cancers. (D) Change in the 3-year survival rate since 2000. (E) Same as (C) but for 5-year survival rate. (F) Same as (D) but for 5 year survival rate. (G) Mortality rate of each cancer, per 100,000 people in the United States. (H) Change in the mortality rates since 2000.

Chapter 2 – Figure 2

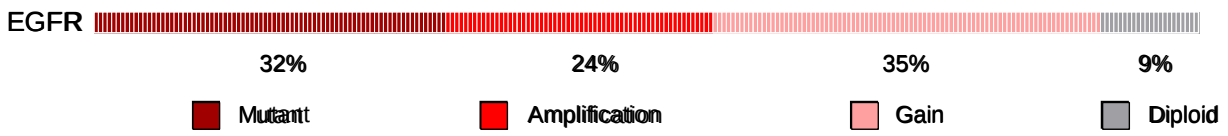

Figure 2. EGFR alteration rate in GBM based on the TCGA data set.[4] 32% of all GBM tumors have a mutation in EGFR with the majority being EGFRvIII. Alterations are not mutually exclusive, as almost all of the mutant tumors are also amplified or have copy number gains.

Chapter 2 – Figure 3.

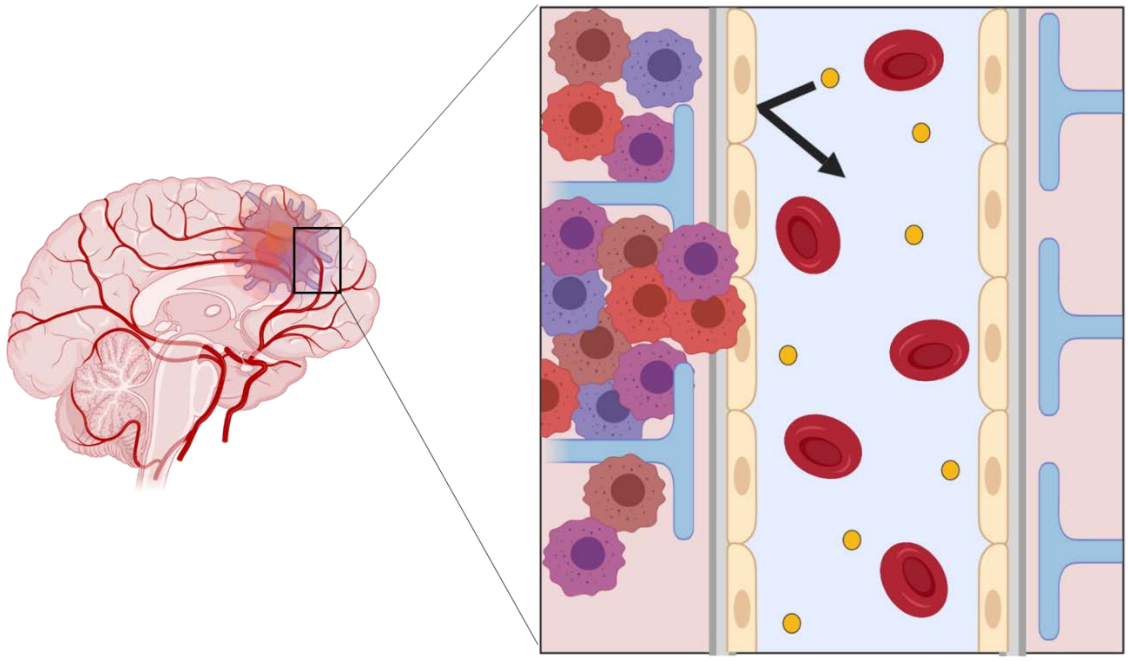

Figure 3. Schematic of the blood brain barrier. Small molecules cannot easily penetrate the blood brain barrier and tumors reside safely on the other side where drug concentrations may not reach therapeutic levels necessary to inhibit tumor growth.

Chapter 2 – Figure 4.

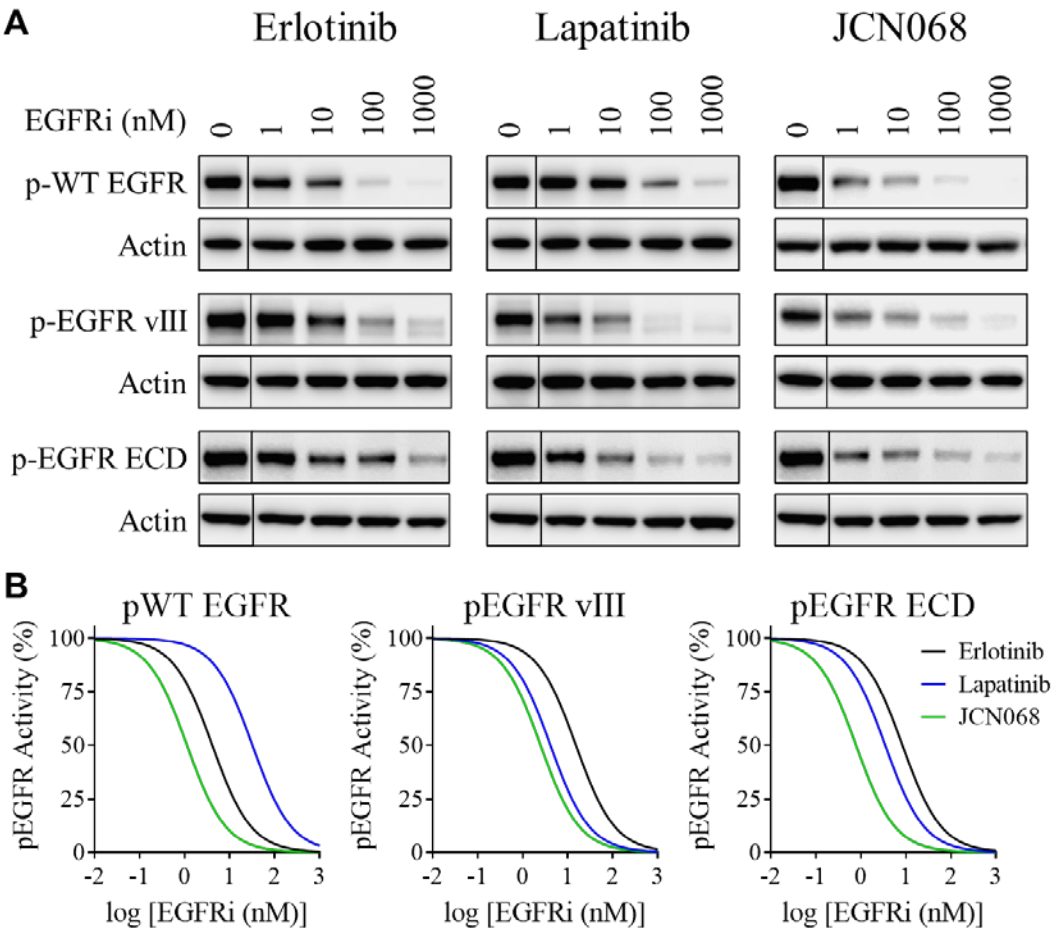

C

EGFRi (nM)	pWT EGFR (nM)	pEGFR vIII (nM)	pEGFR ECD (nM)
Erlotinib	4.13	15.24	8.36
Lapatinib	32.20	4.14	3.47
JCN068	**1.13**	**2.50**	**1.09**

Figure 4. Immunoblots of erlotinib, lapatinib, and JCN068 against U87 GBM lines transduced with EGFR alterations commonly found in GBM. (A) Immunoblots of WT EGFR, EGFRvIII, and EGFR ECD mutant A289D with escalating concentrations of EGFR TKIs erlotinib, lapatinib, and JCN068. (B) Quantification of immunoblots in (A). (C) Tabulated values of the IC_{50} of each EGFR TKI against each EGFR alteration.

Chapter 2 – Table 1. EGFR TKI IC_{50} of variants of EGFR transduced in the U87 GBM cell line calculated from the quantification of immunoblots.

EGFR IC_{50} (nM)	Erlotinib	Lapatinib	AZD9291	AZD3759	JCN068
WT	4.1	32.2	40.4	4.5	1.1
vIII	15.2	4.1	17.7	12.2	2.5
A263P	22.2	2.4	124.4	3.0	1.0
A289D	8.4	3.5	150.6	2.6	1.1
A289V	10.6	7.8	98.0	2.9	1.0
G598V	7.6	1.4	115.1	14.9	1.0

Chapter 2 – Figure 5

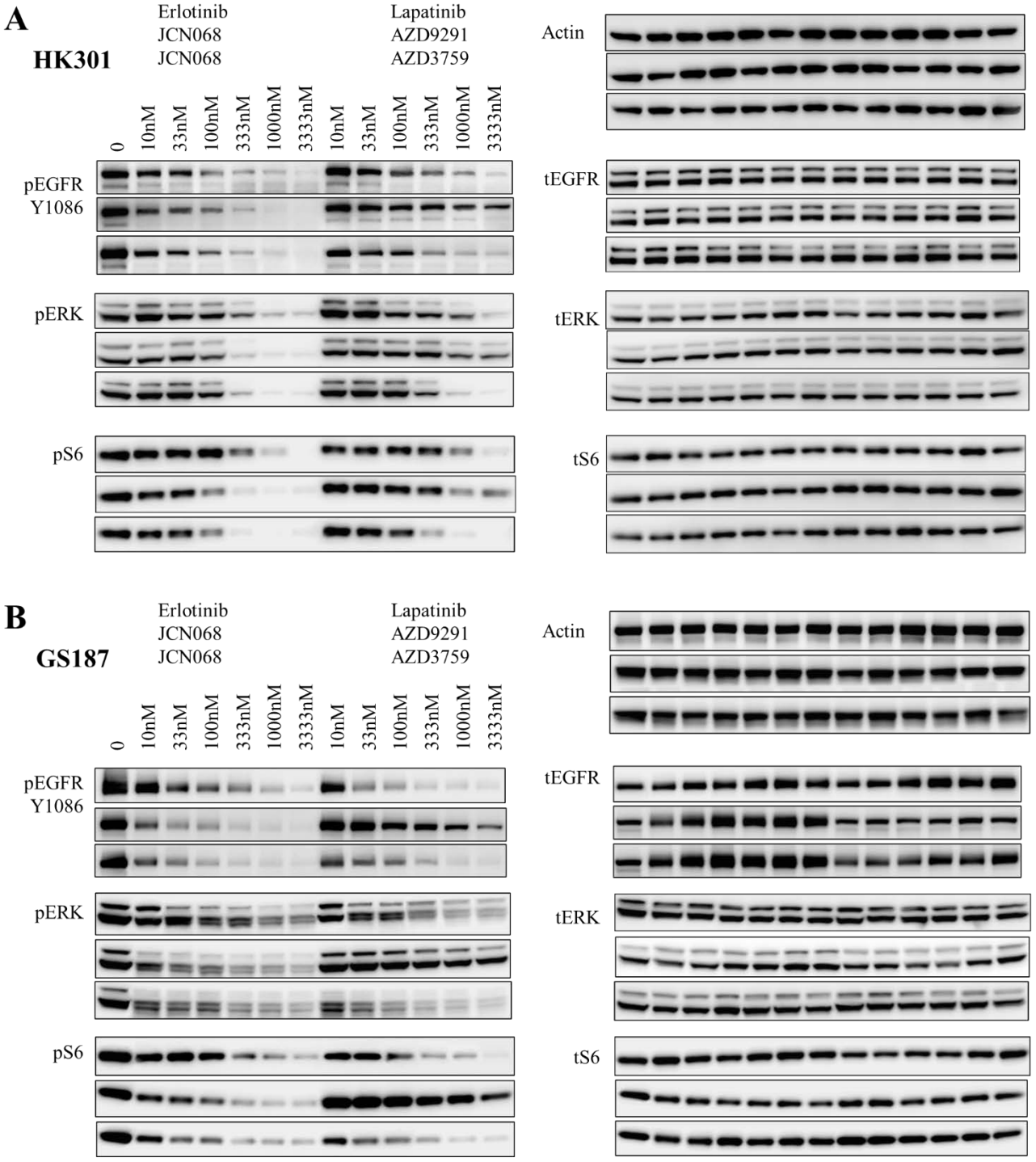

Figure 5. Immunoblots of 1st generation and next generation EGFR TKI and JCN068 against patient-derived GBM gliomaspheres. (A) Immunoblots of erlotinib, lapatinib, JCN068, osimertinib (AZD9291), and AZD3759 in HK301 gliomaspheres that express both amplified WT EGFR and EGFRvIII. EGFR, ERK, and S6 activity are probed. (B) Same as (A), but in the GS187 gliomasphere that expresses EGFR ECD A289D.

Chapter 2 – Figure 6

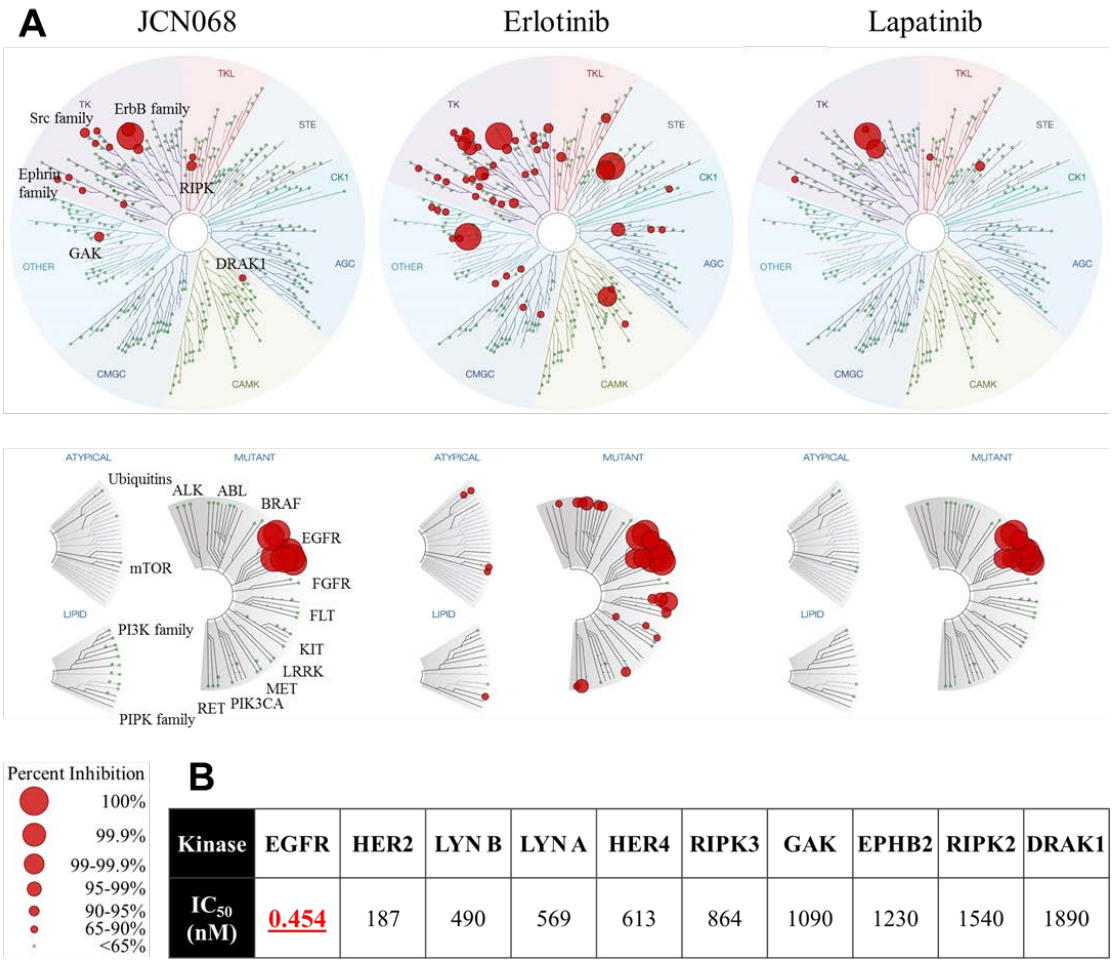

B

Kinase	EGFR	HER2	LYN B	LYN A	HER4	RIPK3	GAK	EPHB2	RIPK2	DRAK1
IC_{50} (nM)	0.454	187	490	569	613	864	1090	1230	1540	1890

Figure 6. Kinome profiling of JCN068 compared to erlotinib and lapatinib. (A) TREEspot™ kinome profile of wild-type kinases (above) and mutant kinases (below) of JCN068, erlotinib, and lapatinib. The size of the circle refers to the percent of control of kinase activity remaining at a drug concentration of 10µM. Image generated using TREEspot™ Software Tool and reprinted with permission from KINOMEscan®, a division of DiscoveRx Corporation, © DISCOVERX CORPORATION 2010. (B) IC_{50} determinations of the top wild-type kinase hits from the primary screen.

Chapter 2 – Figure 7

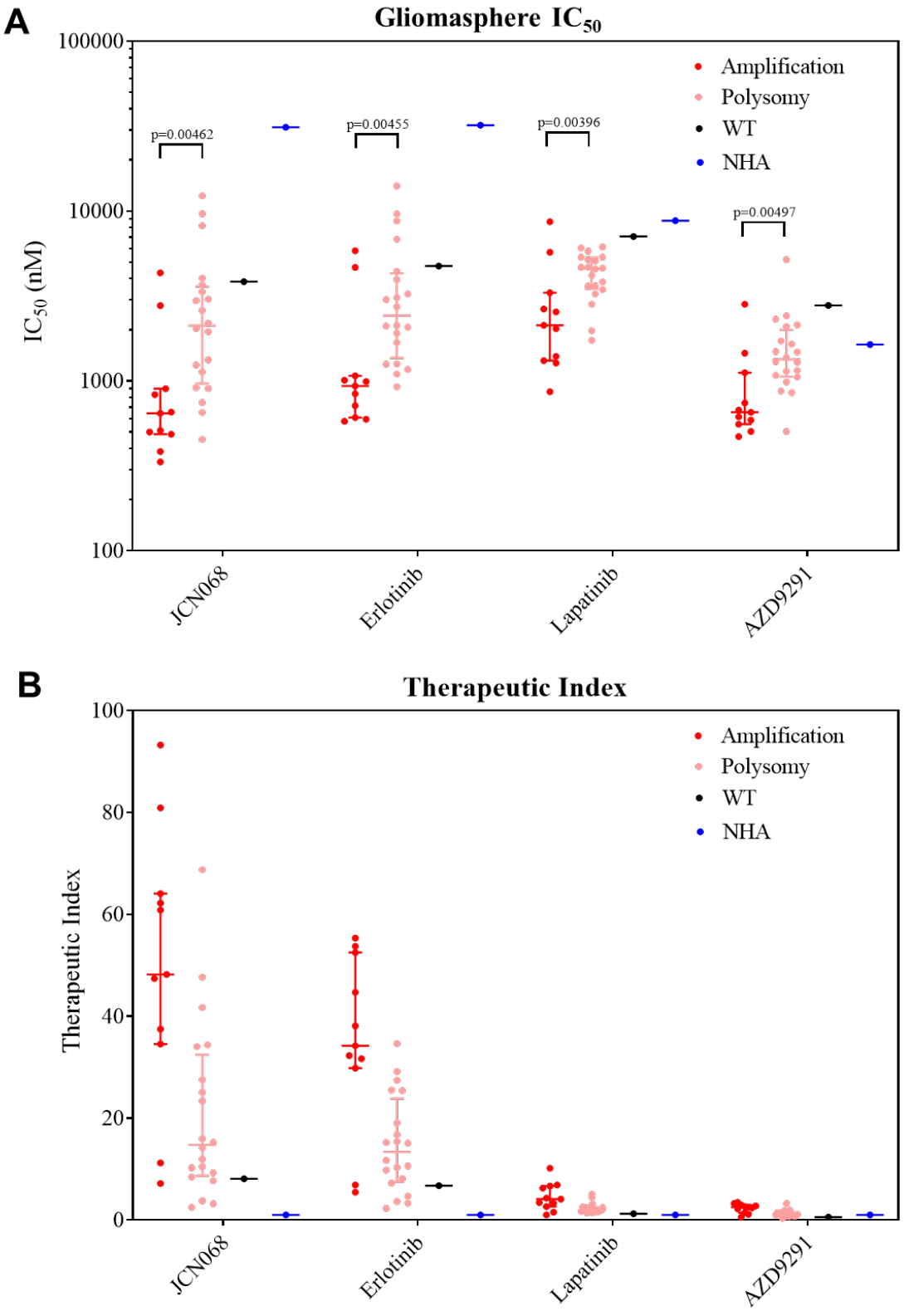

Figure 7. Patient-derived gliomasphere sensitivity to EGFR TKIs. (A) IC_{50} values of a panel of 40 gliomasphere models against JCN068, erlotinib, lapatinib, and osimertinib. Each point represents the average of 3 independent replicates of 1 model from the indicated copy number status. (B) Therapeutic index was calculated by dividing the NHA IC_{50} value by the GBM IC_{50} value to obtain the fold-change range of safe, efficacious concentrations.

Chapter 2- Figure 8

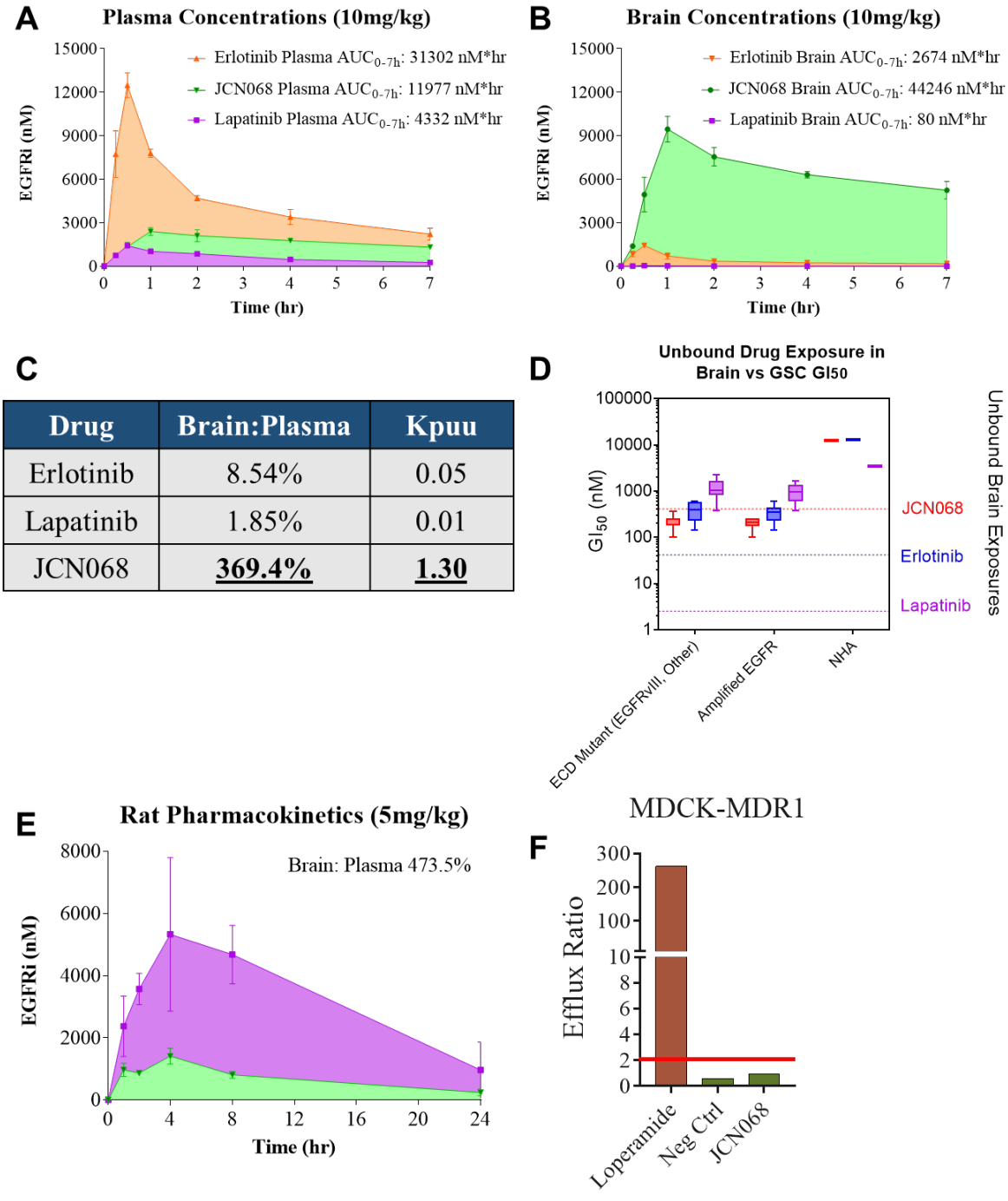

Drug	Brain:Plasma	Kpuu
Erlotinib	8.54%	0.05
Lapatinib	1.85%	0.01
JCN068	**369.4%**	**1.30**

Figure 8. Pharmacokinetics of JCN068. (A) Plasma and (B) brain concentrations of a 10 mg/kg oral dose of erlotinib, lapatinib, or JCN068 in CD-1 male mice. 7-hour exposure levels in each tissue type are noted. (C) Brain to plasma ratios of the EGFR TKIs evalulated and their corresponding Kp_{uu} values. (D) Comparison of the unbound, free drug exposure of the EGFR TKIs in the brain from the pharmacokinetics data with the GI_{50} cell data. JCN068 free drug exposure in the brain is above the GI_{50} concentration while erlotinib and lapatinib free drug exposure in the brain are far below the GI_{50} concentration. (E) Rat pharmacokinetics data performed independently by Charles River. (F) MDCK-MDR1 efflux ratio of JCN068.

Chapter 2 – Figure 9

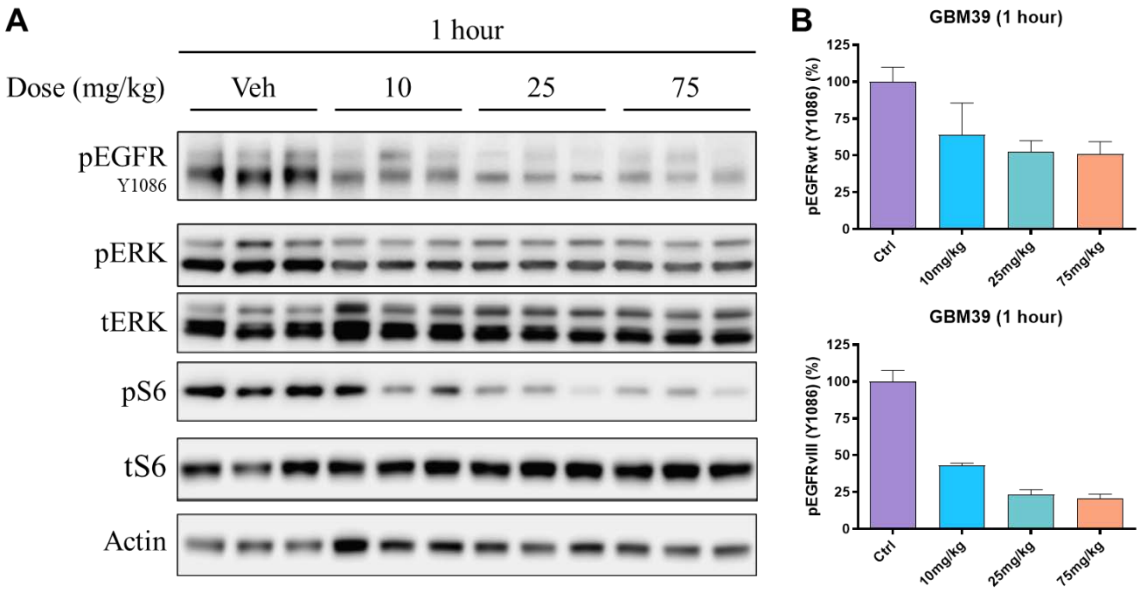

Figure 9. Pharmacodynamic study of JCN068 in GBM39 patient-derived orthotopic xenograft models. (A) Immunoblots at the indicated time point and doses of JCN068 of EGFR and downstream kinases ERK and S6. (B) Quantification of pWTEGFR and pEGFRvIII activity after indicated doses of JCN068.

Chapter 2 – Figure 10

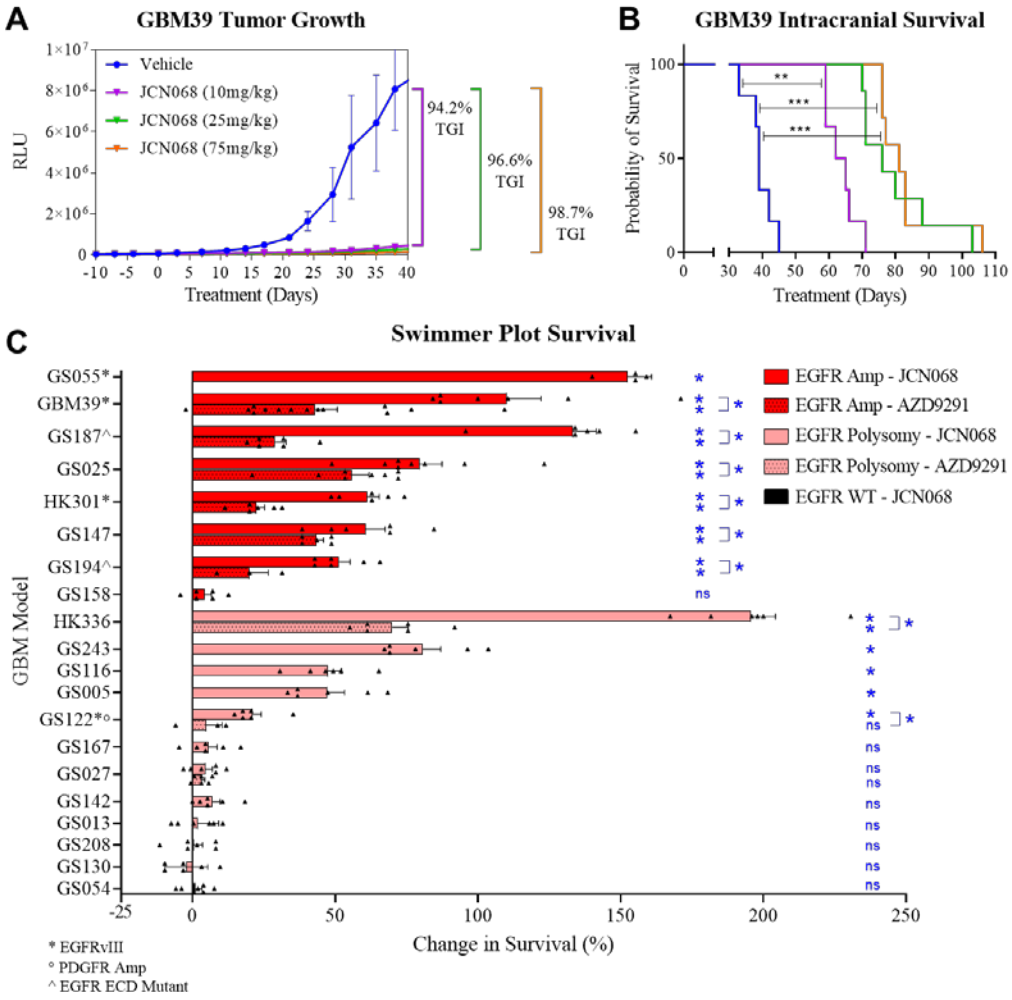

Figure 10. *In vivo* tumor efficacy of JCN068. (A) Tumor growth curves of GBM39 patient-derived orthotopic xenograft models with vehicle, 10 mg/kg, 25 mg/kg, or 75 mg/kg JCN068 treatment. Tumor growth inhibition between the vehicle and each treatment dose is indicated on the right. (n=6 mice per group) (B) Kaplan-Meier curve of GBM39 patient-derived orthotopic xenograft models with their respective treatments. All treatment groups were significantly different from each other except for the 25 mg/kg and 75 mg/kg treatment groups. (C) Swimmer plots of 20 patient-derived orthotopic xenograft models with JCN068 treatment compared against a vehicle control arm (n=6 mice per group). Tumor models were stratified by EGFR copy number status as either amplified, polysomy, or WT. Additional EGFR alterations are noted on at the bottom. 9 different tumor models also had an osimertinib treatment arm (n=6 mice) as comparison with JCN068. Asterisks denote significant survival benefit compared to vehicle treatments and the bracketed asterisk denotes a significant survival difference between JCN068 and osimertinib treatment arms.

Chapter 2 – Figure 11

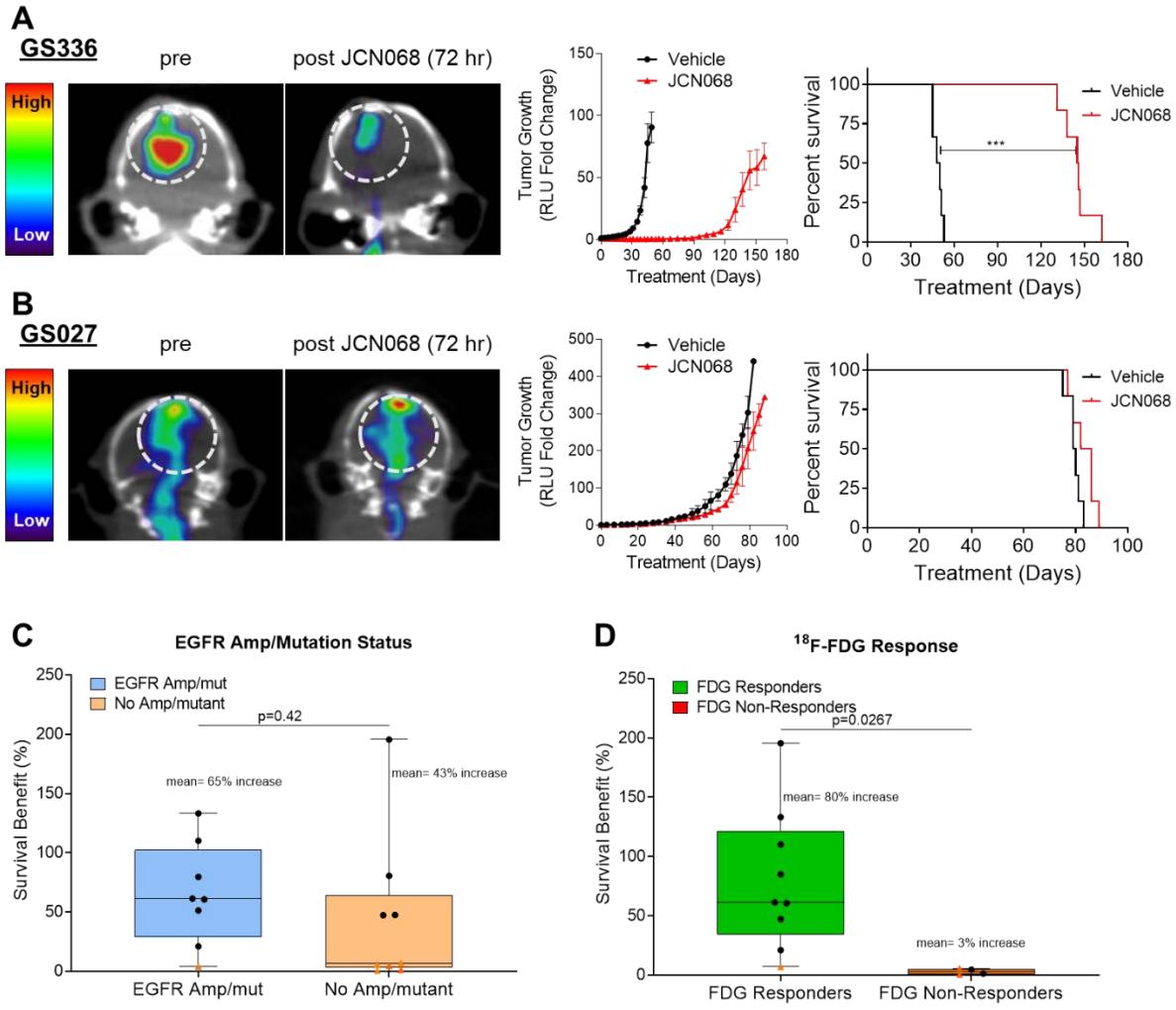

Figure 11. ^{18}F-FDG PET response to JCN068. (A) Representative ^{18}F-FDG PET image of a pre- and post-JCN068 treatment mouse that had a therapeutic response. Scans were visualized by AMIDE and overlaid with CT scans. Coronal slices of the tumor are shown. Images are scaled and normalized to each mouse's individual baseline, pre-treatment scan. Tumor growth (middle) and overall survival outcome (right) are shown for the model. (B) Same as in (A) but for a treatment model that did not have a therapeutic response. (C) Stratification of survival benefit by EGFR alteration status. (D) Stratification of survival benefit by ^{18}F-FDG response status.

SUPPLEMENTARY FIGURES AND TABLES

Chapter 2 – Table S1. Table of kinases tested and their percent kinase inhibition (Thermofisher).

#	Kinase	JCN068 % Kinase Inhibition (10μM)
1	ABL1	49
2	ABL1 E255K	36
3	ABL1 F317I	14
4	ABL1 F317L	30
5	ABL1 G250E	45
6	ABL1 T315I	15
7	ABL1 Y253F	54
8	ABL2 (Arg)	30
9	ACVR1B (ALK4)	-17
10	ADRBK1 (GRK2)	1
11	ADRBK2 (GRK3)	3
12	AKT1 (PKB alpha)	11
13	AKT2 (PKB beta)	10
14	AKT3 (PKB gamma)	-3
15	ALK	26
16	AMPK (A1/B2/G2)	11
17	AMPK (A1/B2/G3)	10
18	AMPK (A2/B1/G2)	3
19	AMPK (A2/B1/G3)	0
20	AMPK (A2/B2/G3)	7
21	AMPK A1/B1/G1	10
22	AMPK A2/B1/G1	12
23	AURKA (Aurora A)	1
24	AURKB (Aurora B)	1
25	AURKC (Aurora C)	2
26	AXL	5
27	BLK	59
28	BMX	13
29	BRAF	13
30	BRAF V599E	20
31	BRSK1 (SAD1)	12
32	BTK	30
33	CAMK1D (CaMKI delta)	16
34	CAMK1G (CAMKI gamma)	2
35	CAMK2A (CaMKII alpha)	9
36	CAMK2B (CaMKII beta)	13
37	CAMK2D (CaMKII delta)	21
38	CAMK4 (CaMKIV)	4
39	CDC42 BPA (MRCKA)	-6
40	CDC42 BPB (MRCKB)	-6
41	CDC42 BPG (MRCKG)	-1
42	CDK1/cyclin B	6
43	CDK17/cyclin Y	1
44	CDK18/cyclin Y	4
45	CDK2/cyclin A	4
46	CDK5/p25	4
47	CDK5/p35	11
48	CDKL5	2
49	CHEK1 (CHK1)	-23
50	CHEK2 (CHK2)	4
51	CLK1	4
52	CLK2	8
53	CLK3	-3
54	CSF1R (FMS)	35
55	CSK	21
56	CSNK1A1 (CK1 alpha 1)	6
57	CSNK1A1L	1
58	CSNK1D (CK1 delta)	6
59	CSNK1E (CK1 epsilon)	9
60	CSNK1E (CK1 epsilon) R178C	11
61	CSNK1G1 (CK1 gamma 1)	5
62	CSNK1G2 (CK1 gamma 2)	7
63	CSNK1G3 (CK1 gamma 3)	3
64	CSNK2A1 (CK2 alpha 1)	1
65	CSNK2A2 (CK2 alpha 2)	8
66	DAPK3 (ZIPK)	2
67	DCAMKL1 (DCLK1)	3
68	DCAMKL2 (DCK2)	8
69	DNA-PK	0
70	DYRK1A	-1
71	DYRK1B	0
72	DYRK3	15
73	DYRK4	-2
74	EEF2K	10
75	EGFR (ErbB1)	88
76	EGFR (ErbB1) C797S	89
77	EGFR (ErbB1) G719C	86
78	EGFR (ErbB1) G719S	85
79	EGFR (ErbB1) L858R	90
80	EGFR (ErbB1) L861Q	91
81	EGFR (ErbB1) T790M	75
82	EGFR (ErbB1) T790M C797S L858R	46
83	EGFR (ErbB1) T790M L858R	76
84	EPHA1	65
85	EPHA2	16
86	EPHA4	43
87	EPHA5	51
88	EPHA8	55
89	EPHB1	52
90	EPHB2	96
91	EPHB3	36
92	EPHB4	79
93	ERBB2 (HER2)	89
94	ERBB4 (HER4)	88
95	FER	9
96	FES (FPS)	11
97	FGFR1	8
98	FGFR2	0
99	FGFR2 N549H	-14
100	FGFR3	6
101	FGFR3 K650E	3
102	FGFR3 V555M	-11
103	FGFR4	-2
104	FGR	87
105	FLT1 (VEGFR1)	-12
106	FLT3	28
107	FLT3 D835Y	52
108	FLT4 (VEGFR3)	-2
109	FRAP1 (mTOR)	-8
110	FRK (PTK5)	47
111	FYN	33
112	GRK4	-1
113	GRK5	-3
114	GRK6	0
115	GRK7	4
116	GSK3A (GSK3 alpha)	5
117	GSK3B (GSK3 beta)	11
118	HCK	44
119	HIPK1 (Myak)	3
120	HIPK2	6
121	HIPK3 (YAK1)	-2
122	HIPK4	5
123	IGF1R	1
124	IKBKB (IKK beta)	6
125	IKBKE (IKK epsilon)	6
126	INSR	-8
127	INSRR (IRR)	-4
128	IRAK4	2
129	ITK	10
130	JAK1	-11
131	JAK2	-16
132	JAK2 JH1 JH2	-7
133	JAK2 JH1 JH2 V617F	-16
134	JAK3	6
135	KDR (VEGFR2)	27
136	KIT	-13
137	KIT T670I	-16
138	KIT V559D	-1
139	KIT V559D V654A	-10
140	KIT V560G	0
141	KSR2	26
142	LCK	79
143	LTK (TYK1)	22
144	LYN A	85
145	LYN B	93
146	MAP2K1 (MEK1)	20
147	MAP2K2 (MEK2)	8
148	MAP2K6 (MKK6)	4
149	MAP3K19 (YSK4)	6
150	MAP3K8 (COT)	3
151	MAP3K9 (MLK1)	-2
152	MAP4K2 (GCK)	14
153	MAP4K4 (HGK)	64
154	MAP4K5 (KHS1)	28
155	MAPK1 (ERK2)	4
156	MAPK10 (JNK3)	17
157	MAPK11 (p38 beta)	10
158	MAPK12 (p38 gamma)	11
159	MAPK13 (p38 delta)	0
160	MAPK14 (p38 alpha)	40
161	MAPK14 (p38 alpha) Direct	25
162	MAPK3 (ERK1)	9
163	MAPK7 (ERK5)	19
164	MAPK8 (JNK1)	11
165	MAPK9 (JNK2)	16
166	MAPKAPK2	25
167	MAPKAPK3	19
168	MAPKAPK5 (PRAK)	16
169	MARK1 (MARK)	4
170	MARK2	3
171	MARK3	9
172	MARK4	0
173	MATK (HYL)	6
174	MELK	32
175	MERTK (cMER)	19
176	MET (cMet)	-4
177	MET (cMet) Y1235D	-2
178	MET M1250T	6
179	MINK1	66
180	MKNK1 (MNK1)	16
181	MST1R (RON)	-1
182	MST4	12
183	MUSK	-3
184	MYLK2 (skMLCK)	8
185	NEK1	18
186	NEK2	-4
187	NEK4	0
188	NEK6	2
189	NEK9	-6
190	NIM1K	-1
191	NTRK1 (TRKA)	26
192	NTRK2 (TRKB)	6
193	NTRK3 (TRKC)	6
194	PAK1	9
195	PAK2 (PAK65)	10
196	PAK3	7
197	PAK4	2
198	PAK6	3
199	PAK7 (KIAA1264)	5
200	PASK	6
201	PDGFRA (PDGFR alpha)	7
202	PDGFRA D842V	14
203	PDGFRA T674I	-4
204	PDGFRA V561D	47
205	PDGFRB (PDGFR beta)	-5
206	PDK1	9
207	PDK1 Direct	-8
208	PEAK1	41
209	PHKG1	48
210	PHKG2	6
211	PIM1	30
212	PIM2	0
213	PIM3	-4
214	PKN1 (PRK1)	-1
215	PLK1	10
216	PLK2	2
217	PLK3	-5
218	PRKACA (PKA)	5
219	PRKCA (PKC alpha)	2
220	PRKCB1 (PKC beta I)	-2
221	PRKCB2 (PKC beta II)	-3
222	PRKCD (PKC delta)	5
223	PRKCE (PKC epsilon)	8
224	PRKCG (PKC gamma)	5
225	PRKCH (PKC eta)	2
226	PRKCI (PKC iota)	-8
227	PRKCN (PKD3)	15
228	PRKCQ (PKC theta)	-6
229	PRKCZ (PKC zeta)	6
230	PRKD1 (PKC mu)	26
231	PRKD2 (PKD2)	21
232	PRKG1	0
233	PRKG2 (PKG2)	6
234	PRKX	3
235	PTK2 (FAK)	8
236	PTK2B (FAK2)	2
237	PTK6 (Brk)	28
238	RAF1 (cRAF) Y340D Y341D	1
239	RET	60
240	RET A883F	29
241	RET S891A	37
242	RET V804E	4

#	Kinase	JCN068 % Kinase Inhibition (10μM)
243	RET V804L	25
244	RET Y791F	76
245	ROCK1	2
246	ROCK2	0
247	ROS1	13
248	RPS6KA1 (RSK1)	12
249	RPS6KA2 (RSK3)	5
250	RPS6KA3 (RSK2)	13
251	RPS6KA4 (MSK2)	-2
252	RPS6KA5 (MSK1)	3
253	RPS6KB1 (p70S6K)	2
254	RPS6KB2 (p70S6Kb)	3
255	SBK1	33
256	SGK (SGK1)	7
257	SGK2	3
258	SGKL (SGK3)	0
259	SNF1LK2	29
260	SRC	28
261	SRC N1	43
262	SRMS (Srm)	8
263	SRPK1	3
264	SRPK2	3
265	STK22B (TSSK2)	3
266	STK22D (TSSK1)	-1
267	STK23 (MSSK1)	1
268	STK24 (MST3)	8
269	STK25 (YSK1)	2
270	STK3 (MST2)	-9
271	STK4 (MST1)	-2
272	SYK	-1
273	TAOK2 (TAO1)	-10
274	TBK1	5
275	TEK (Tie2)	7
276	TEK (TIE2) Y897S	-18
277	TNK1	3
278	TXK	30
279	TYK2	7
280	TYRO3 (RSE)	16
281	YES1	73
282	ZAP70	-1
283	CAMK1 (CaMK1)	6
284	CDK4/cyclin D1	1
285	CDK4/cyclin D3	-3
286	CDK6/cyclin D1	10
287	CDK7/cyclin H/MNAT1	7
288	CDK9/cyclin T1	7
289	CHUK (IKK alpha)	8
290	DAPK1	14
291	GSG2 (Haspin)	5
292	IRAK1	12
293	LRRK2	8
294	LRRK2 FL	23
295	LRRK2 G2019S	16
296	LRRK2 G2019S FL	7
297	LRRK2 I2020T	5
298	LRRK2 R1441C	9
299	NUAK1 (ARK5)	14
300	PI4K2A (PI4K2 alpha)	17
301	PI4K2B (PI4K2 beta)	11
302	PI4KA (PI4K alpha)	-1
303	PI4KB (PI4K beta)	21
304	PIK3C2A (PI3K-C2 alpha)	13
305	PIK3C2B (PI3K-C2 beta)	59
306	PIK3C2G (PI3K-C2 gamma)	33
307	PIK3C3 (hVPS34)	-14
308	PIK3CA E542K/PIK3R1 (p110 alpha E542K/p85 alpha)	-2
309	PIK3CA E545K/PIK3R1 (p110 alpha E545K/p85 alpha)	0
310	PIK3CA/PIK3R1 (p110 alpha/p85 alpha)	3
311	PIK3CA/PIK3R3 (p110 alpha/p55 gamma)	2
312	PIK3CB/PIK3R1 (p110 beta/p85 alpha)	-5
313	PIK3CB/PIK3R2 (p110 beta/p85 beta)	-14
314	PIK3CD/PIK3R1 (p110 delta/p85 alpha)	21
315	PIK3CG (p110 gamma)	2
316	PIP4K2A	-7
317	PIP5K1A	-8
318	PIP5K1B	6
319	PIP5K1C	-11
320	SPHK1	-1
321	SPHK2	-8
322	AAK1	8
323	ABL1 H396P	55

#	Kinase	JCN068 % Kinase Inhibition (10μM)
324	ABL1 M351T	51
325	ABL1 Q252H	63
326	ACVR1 (ALK2)	60
327	ACVR1 (ALK2) R206H	66
328	ACVR2A	9
329	ACVR2B	-2
330	ACVRL1 (ALK1)	33
331	ADCK3	32
332	ALK C1156Y	40
333	ALK F1174L	35
334	ALK L1196M	14
335	ALK R1275Q	39
336	ALK T1151_L1152insT	28
337	AMPK (A1/B1/G2)	11
338	AMPK (A1/B1/G3)	12
339	AMPK (A1/B2/G1)	11
340	AMPK (A2/B2/G1)	6
341	AMPK (A2/B2/G2)	8
342	ANKK1	15
343	AXL R499C	1
344	BMPR1A (ALK3)	10
345	BMPR1B (ALK6)	6
346	BMPR2	4
347	BRAF	3
348	BRAF V599E	7
349	BRSK2	12
350	CAMK2G (CaMKII gamma)	2
351	CAMKK1 (CAMKKA)	0
352	CAMKK2 (CaMKK beta)	3
353	CASK	11
354	CDC7/DBF4	8
355	CDK11 (Inactive)	-2
356	CDK11/cyclin C	6
357	CDK13/cyclin K	8
358	CDK14 (PFTK1)/cyclin Y	7
359	CDK16 (PCTK1)/cyclin Y	8
360	CDK2/cyclin A1	-2
361	CDK2/cyclin E1	9
362	CDK2/cyclin O	-3
363	CDK3/cyclin E1	3
364	CDK5 (Inactive)	9
365	CDK8/cyclin C	4
366	CDK9 (Inactive)	-3
367	CDK9/cyclin K	2
368	CLK4	9
369	DAPK2	27
370	DDR1	57
371	DDR2	18
372	DDR2 N456S	104
373	DDR2 T654M	36
374	DMPK	38
375	DYRK2	15
376	EGFR (ErbB1) d746-750	100
377	EGFR (ErbB1) d747-749 A750P	102
378	EIF2AK2 (PKR)	44
379	EPHA3	18
380	EPHA6	80
381	EPHA7	44
382	ERN1	26
383	ERN2	10
384	FGFR1 V561M	4
385	FGFR3 G697C	-10
386	FGFR3 K650M	27
387	FLT3 ITD	34
388	FYN A	15
389	GAK	85
390	GRK1	-1
391	HUNK	6
392	ICK	2
393	IRAK3	42
394	KIT A829P	30
395	KIT D816H	58
396	KIT D816V	53
397	KIT D820E	8
398	KIT N822K	30
399	KIT T670E	3
400	KIT V559D T670I	17
401	KIT V654A	12
402	KIT Y823D	29
403	LATS2	4
404	LIMK1	-2
405	LIMK2	3
406	MAP2K1 (MEK1)	10
407	MAP2K1 (MEK1) S218D S222D	5
408	MAP2K2 (MEK2)	2
409	MAP2K4 (MEK4)	0

#	Kinase	JCN068 % Kinase Inhibition (10μM)
410	MAP2K5 (MEK5)	11
411	MAP2K6 (MKK6)	9
412	MAP2K6 (MKK6) S207E T211E	3
413	MAP3K10 (MLK2)	1
414	MAP3K11 (MLK3)	3
415	MAP3K14 (NIK)	8
416	MAP3K2 (MEKK2)	10
417	MAP3K3 (MEKK3)	4
418	MAP3K5 (ASK1)	3
419	MAP3K7/MAP3K7IP1 (TAK1-TAB1)	9
420	MAP4K1 (HPK1)	7
421	MAP4K3 (GLK)	13
422	MAPK10 (JNK3)	12
423	MAPK15 (ERK7)	8
424	MAPK8 (JNK1)	6
425	MAPK9 (JNK2)	20
426	MASTL	7
427	MERTK (cMER) A708S	14
428	MET D1228H	16
429	MKNK2 (MNK2)	37
4430	MLCK (MLCK2)	8
431	MLK4	-16
432	MYLK (MLCK)	-4
433	MYLK4	15
434	MYO3A (MYO3 alpha)	3
435	MYO3B (MYO3 beta)	8
436	NEK8	-1
437	NLK	-6
438	NUAK2	0
439	PKMYT1	3
440	PKN2 (PRK2)	8
441	PLK4	15
442	PRKACB (PRKAC beta)	4
443	PRKACG (PRKAC gamma)	3
444	RAF1 (cRAF) Y340D Y341D	6
445	RET G691S	32
446	RET M918T	51
447	RET V804M	10
448	RIPK2	89
449	RIPK3	95
450	SIK1	24
451	SIK3	22
452	SLK	35
453	STK16 (PKL12)	2
454	STK17A (DRAK1)	82
455	STK17B (DRAK2)	49
456	STK32B (YANK2)	11
457	STK32C (YANK3)	3
458	STK33	8
459	STK38 (NDR)	7
460	STK38L (NDR2)	-9
461	STK39 (STLK3)	3
462	TAOK1	13
463	TAOK3 (JIK)	0
464	TEC	12
465	TEK (TIE2) R849W	16
467	TEK (TIE2) Y1108F	10
468	TESK1	2
469	TESK2	-6
470	TGFBR1 (ALK5)	6
471	TGFBR2	31
472	TLK1	-3
473	TLK2	-2
474	TNIK	37
475	TNK2 (ACK)	11
476	TTK	4
477	ULK1	1
478	ULK2	2
479	ULK3	5
480	VRK2	14
481	WEE1	2
482	WNK1	5
483	WNK2	-4
484	WNK3	-2
485	ZAK	6

Chapter 2 – Figure S1

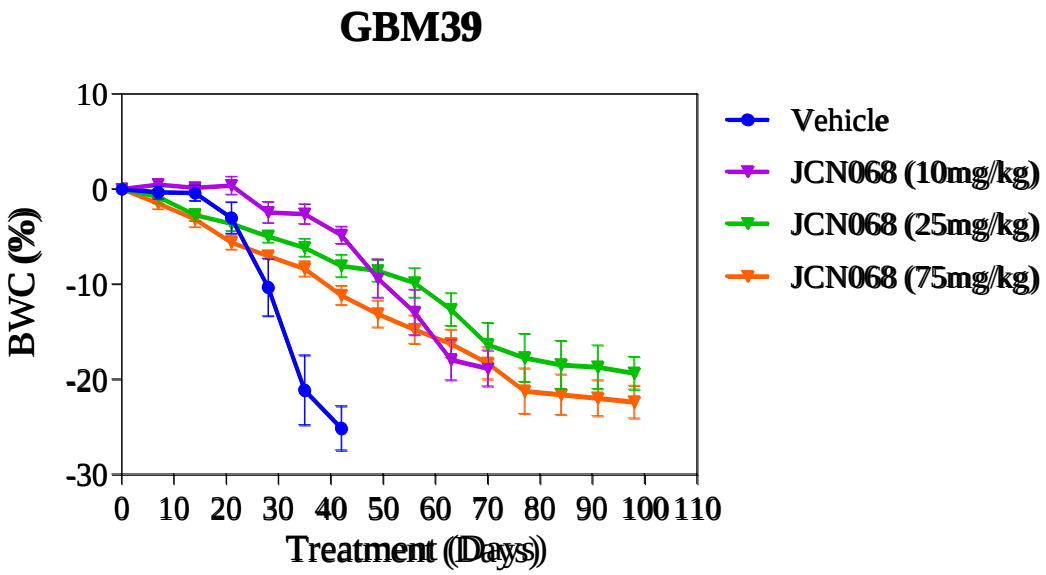

Figure S1. Body weight change of GBM39 tumor bearing NSG mice.

Chapter 2 – Figure S2

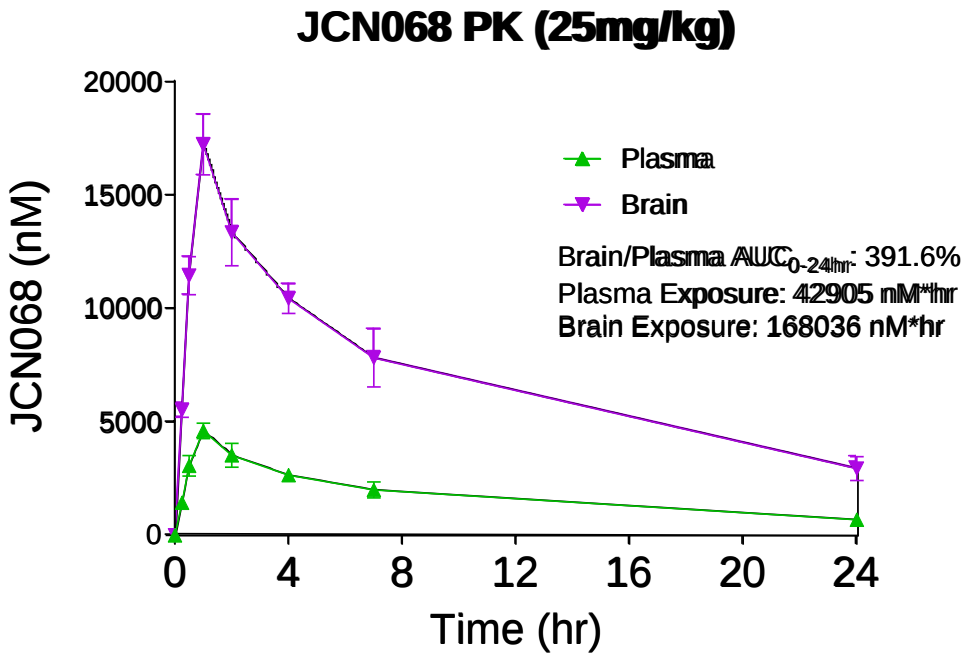

Figure S2. Pharmacokinetics of plasma and brain tissue of JCN068 at 25 mg/kg dose.

EXPERIMENTAL METHODS

Cell culture conditions. Patient-derived GBM cells were cultured in serum-free gliomasphere conditions consisting of DMEM/F12 (Thermofisher), B27 (Thermofisher), Penicillin-Streptomycin (100U/mL penicillin, 100mg/mL streptomycin, Thermofisher), and Glutamax (Thermofisher) supplemented with Heparin (5μg/mL, Sigma), Human EGF (50ng/mL, Thermofisher), and Human FGF-β (20ng/mL, Thermofisher). U87 cells were cultured in DMEM (Thermofisher), FBS (10%, Gemini Bio-Products), Penicillin-Streptomycin, and Glutamax. Cells were dissociated to single cell suspensions with TrypLE (Thermofisher) and resuspended in its respective media. Cell lines were regularly tested for mycoplasma infection using Myco Alert™ Mycoplasma Detection Kit according to the manufacturer's protocol (Lonza).

Reagents and antibodies. The following chemical inhibitors were dissolved in DMSO for all in vitro studies: erlotinib (Chemietek), lapatinib (MedChemExpress), osimertinib (MedChemExpress), AZD3759 (MedChemExpress), JCN068. The following antibodies for immunoblotting were obtained from the listed sources: p-EGFR Y1086 (Thermofisher, 36-9700), t-EGFR (Millipore, 06-847), p-AKT T308 (Cell Signaling, 13038), p-AKT S473 (Cell Signaling, 4060), t-AKT (Cell Signaling, 4685), p-ERK T202/Y204 (Cell Signaling, 4370), t-ERK (Cell Signaling, 4695), p-S6 S235/236 (Cell Signaling, 4858), t-S6 (Cell Signaling, 2217), β-Actin (Cell Signaling, 3700).

Cell based IC_{50}. U87-WTEGFR and U87-EGFRvIII cells were acclimated overnight in standard cell culture conditions. Cells were washed with PBS and cultured overnight in serum-free DMEM (Thermofisher), Penicillin-Streptomycin, and Glutamax. U87-WTEGFR cells were stimulated

with Heparin (5µg/mL, Sigma), Human EGF (50ng/mL, Thermofisher) for 1 hr followed by EGFR TKI treatment for 1 hr before being collected. U87-EGFRvIII cells and U87-EGFR ECD mutant cells were treated with EGFR TKI for 1 hr before being collected.

Immunoblotting. Cells were collected and lysed in RIPA buffer (Boston BioProducts) containing Halt™ Protease and Phosphatase Inhibitor (Thermofisher). Lysates were centrifuged at 14,000g for 15min at 4°C. Protein samples were then boiled in NuPAGE LDS Sample Buffer (Thermofisher) and NuPAGE Sample Reducing Agent (Thermofisher), separated using SDS-PAGE on 4-12% Bis-Tris gels (Thermofisher), and transferred to nitrocellulose membrane (GE Healthcare). Immunoblotting was performed per antibody's manufacturer's specifications. Membranes were developed using the SuperSignal™ system (Thermofisher) and imaged using the Odyssey Fc Imaging System (LI-COR). Signal quantification was performed using the Image Studio™ software (LI-COR).

Kinome profiling. JCN068 was profiled by the SelectScreen Kinase Profiling by Thermofisher. 485 purified wild-type and mutant kinases were profiled at a 10µM concentration of JCN068 at Km [app] ATP in duplicates. Top hits that inhibited >80% of kinase activity in the single point screen at 10µM were selected for a IC_{50} determination with a 10-point titration curve (Thermofisher).

Growth inhibition assays. Growth inhibition assays were performed by incubating 1500 cells per well in 384-well plates for 72 hours with EGFR inhibitor. A 14-point titration curve of each EGFR inhibitor was performed in quadruplicate. All growth inhibition assays were independently

repeated at least 3 times. Cell Titer Glo Luminescent Cell Viability Assay (Promega) was used to measure growth inhibition from control of each EGFR inhibitor. Luminescence (integration time 1 sec) was recorded on a CLARIOstar microplate reader (BMG Labtech).

Permeability assays. Permeability assays were performed by Charles River using a confluent monolayer of Madin Darby Canine Kidney (MDCK) epithelial cells stably transfected with the human *MDR1* gene (gene encoding P-gp). For the apical to basolateral (A→B) permeability, the EGFR inhibitors in the presence or absence of 50 μM verapamil (a P-gp inhibitor) was added to the apical side and permeation was measured from the basolateral side after a 2 hr incubation; the converse was applied for the basolateral to apical (B→A) permeability. The EGFR inhibitors in the supernatant of the apical and basolateral sides were analyzed by LC-MS/MS to determine permeability and efflux ratios.

Pharmacokinetic studies. Male CD-1 mice were treated by oral gavage with 10 mg/kg of EGFR inhibitor. Mice were euthanized and whole blood and brain tissue were collected at 0, 0.25, 0.5, 1, 2, 4, 7, and 24 hrs post treatment (n=2 mice per time point). Whole blood from mice was centrifuged to isolate plasma. EGFR inhibitors were isolated by liquid-liquid extraction from plasma: 50 μL plasma was added to 150 μL acetonitrile and 5 pmol gefitinib internal standard. Mouse brain tissue was washed with 2 mL cold PBS and homogenized using a tissue homogenizer in 2 mL cold water. EGFR inhibitors were then isolated and reconstituted in a similar manner by liquid-liquid extraction: 100 μL brain homogenate was added to 5 pmol gefitinib internal standard and 300 μL acetonitrile. After vortex mixing, the samples were centrifuged. The supernatant was removed and evaporated by a rotary evaporator and reconstituted in 100 μL 50:50:0.1 water:acetonitrile:formic acid.

Protein binding assay. Protein binding was assessed using rapid equilibrium dialysis plates (8K MWCO, Thermofisher). Briefly, homogenized tissue samples or plasma was incubated in the dialysis plates to dialyze with PBS for 6 hours under agitation. Tissue homogenate, plasma, and their corresponding PBS dialysis was then collected and EGFR inhibitors were isolated as specified above.

EGFR inhibitor detection. Chromatographic separations were performed on a 100 x 2.1 mm Phenomenex Kinetex C18 column (Kinetex) using the 1290 Infinity LC system (Agilent). The mobile phase was composed of solvent A: 0.1% formic acid in Milli-Q water, and B: 0.1% formic acid in acetonitrile. Analytes were eluted with a gradient of 5% B (0-4 min), 5-99% B (4-32 min), 99% B (32-36 min), and then returned to 5% B for 12 min to re-equilibrate between injections. Injections of 20 μL into the chromatographic system were used with a solvent flow rate of 0.10 mL/min. Mass spectrometry was performed on the 6460 triple quadrupole LC/MS system (Agilent). Ionization was achieved by using electrospray in the positive mode and data acquisition was made in multiple reactions monitoring (MRM) mode. Analyte signal was normalized to the internal standard and concentrations were determined by extrapolating on to the calibration curve (10, 100, 1000, 4000 nM). EGFR inhibitor brain concentrations were adjusted by 1.4% of the mouse brain weight for the residual blood in the brain vasculature as described previously.[48]

Genetic manipulation. Lentiviruses used for genetic manipulation were produced by transfecting 293-FT cells (ATCC) using lipofectamine 2000 (Thermofisher). Viruses were collected following 48 hr after transfection. Lentiviral vector backbones for the overexpression of WTEGFR, EGFRvIII, and EGFR ECD mutants in U87 cells contained a CMV promoter. U87-WTEGFR,

U87-EGFRvIII, and U87-EGFR ECD mutant cells were generated by transfection with these overexpression vectors. For in vivo tumors, GBM gliomaspheres were infected with a lentiviral vector containing a secreted Gaussia luciferase (sGluc) reporter gene.

Intracranial Gaussia luciferase measurements. To measure the levels of sGluc, 6 µL of blood was collected from the tail vein of the mice and immediately mixed with 50mM EDTA to prevent coagulation. sGluc activity was obtained by measuring chemiluminescence following injection of 100 µL of 100uM coelenterazine (Nanolight) in a 96 well plate as described previously.[35]

Ex vivo immunoblot studies. NSG mice (UCLA Radiation Oncology) were anesthetized by isoflurane before intracranial injections. Briefly, mice were subcutaneously injected with Carprofen and shaved to remove fur around the injection site. The exposed skin was then sterilized by betadine and ethanol. An incision about 2 cm in length was then made using a No. 15 scalpel by pulling the blade diagonally from near the left eye posterior to the right rostral. Using the stereotactic unit, the needle was positioned 1 mm anterior and 2 mm lateral to bregma. The drill was rotated upon contact with the skull and lightly touched for a few seconds and then pulled away to prevent overheating of the skill from friction. The needle was lowered into the skull at a rate of 0.1 mm / 5 seconds until it was 2.5 mm deep, and held for 30 seconds. The needle was then raised at a rate of 0.1 mm / 5 seconds up to 2 mm, leaving behind a small cavity for the injection. 2 µL cell suspensions containing 4 x 10^5 GBM39 tumor cells in DMEM/F12 basal media were then injected at a rate of 0.1 µL / 10 seconds. The needle was drawn up at a rate of 0.1 mm /10 seconds. The skull was then sealed using a small piece of sterile bone wax. Tissue adhesive was then applied to the inside of the skin and the incision was closed. The next day, mice were treated with

Carprofen for pain relief. Animal health was monitored daily after implantation and tumor burden was monitored once a week by measurement of secreted gaussia luciferase in blood from the orthotopically implanted GBM tumors. When the tumors were engrafted and began an exponential growth phase by gaussia luciferase measurement as described above, mice were randomized into treatments arms and were treated by oral gavage with either vehicle, 10 mg/kg, 25 mg/kg, or 75 mg/kg JCN068 for 1 hour. Mice were then euthanized, and tumors were isolated by macro dissection with GFP fluorescence. Tumors were lysed by sonication in RIPA buffer (Boston BioProducts) containing Halt™ Protease and Phosphatase Inhibitor (Thermofisher). The immunoblotting protocol above was then performed on lysates.

Intracranial mouse treatment studies. GBM gliomasphere cells were intracranially injected in NSG mice as described above. Following three consecutive increasing growth measurements and secreted *gaussia* luciferase reaching approximately 30,000 RLU, tumor-bearing mice were randomized into vehicle or treatment groups (n = 6 mice per group). The randomization date was denoted as treatment day 0. Mice were treated for 5 days followed by 2 days of no treatment each week until endpoints were reached. Mice were euthanized when moribund or reached a 25% loss in body weight. All studies were in accordance with UCLA Animal Research Committee protocol guidelines.

18F-FDG PET Imaging. For 18F-FDG PET scans, mice were treated with vehicle, anesthetized with 2% isoflurane, and intravenously injected with 300 μCi of ^{18}F-FDG. Following 1 hr unconscious uptake, mice were taken off anesthesia but kept warm for another 5 hr of uptake. 6 hr after the initial administration of ^{18}F-FDG, mice were imaged using G8 PET/CT scanner (Sofie

Biosciences). Mice were imaged using a 15 min static PET scan followed by a 3 min CT scan. Following the baseline, pre-treatment scan, mice were then dosed with JCN068 (25 mg/kg) for 3 days. The treatment ^{18}F-FDG PET scan was performed under the same conditions. Quantification was performed by drawing a 3D region of interest (ROI) using the AMIDE software over the same location in both baseline and treatment scans to obtain the mean SUV.

Statistical Analyses. Unless otherwise specified, student's t-tests were performed for statistical analyses and p-values <0.05 were considered significant. All statistical analyses were calculated using GraphPad Prism.

REFERENCES

1. SEER*Explorer: An interactive website for SEER cancer statistics [Internet]. Surveillance Research Program, National Cancer Institute. [Cited 2020 Sep 14]. Available from https://seer.cancer.gov/explorer/.

2. Wen, Patrick Y., and Santosh Kesari. "Malignant gliomas in adults." New England Journal of Medicine 359.5 (2008): 492-507.

3. Stupp, Roger, et al. "Effects of radiotherapy with concomitant and adjuvant temozolomide versus radiotherapy alone on survival in glioblastoma in a randomised phase III study: 5-year analysis of the EORTC-NCIC trial." The lancet oncology 10.5 (2009): 459-466.

4. Brennan, Cameron W., et al. "The somatic genomic landscape of glioblastoma." Cell 155.2 (2013): 462-477.

5. Vivanco, Igor, et al. "Differential sensitivity of glioma-versus lung cancer–specific EGFR mutations to EGFR kinase inhibitors." Cancer discovery 2.5 (2012): 458-471.

6. Zhu, Haihao, et al. "Oncogenic EGFR signaling cooperates with loss of tumor suppressor gene functions in gliomagenesis." Proceedings of the National Academy of Sciences 106.8 (2009): 2712-2716.

7. Fan, Qi-Wen, et al. "EGFR phosphorylates tumor-derived EGFRvIII driving STAT3/5 and progression in glioblastoma." Cancer cell 24.4 (2013): 438-449.

8. Babic, Ivan, et al. "EGFR mutation-induced alternative splicing of Max contributes to growth of glycolytic tumors in brain cancer." Cell metabolism 17.6 (2013): 1000-1008.

9. Vogelbaum, M. A., et al. "Phase II trial of the EGFR tyrosine kinase inhibitor erlotinib for single agent therapy of recurrent glioblastoma multiforme: interim results." Journal of Clinical Oncology 22.14_suppl (2004): 01558-1558.

10. Thiessen, Brian, et al. "A phase I/II trial of GW572016 (lapatinib) in recurrent glioblastoma multiforme: clinical outcomes, pharmacokinetics and molecular correlation." Cancer chemotherapy and pharmacology 65.2 (2010): 353-361.

11. Rich, Jeremy N., et al. "Phase II trial of gefitinib in recurrent glioblastoma." Journal of Clinical Oncology 22.1 (2004): 133-142.

12. Reardon, David A., et al. "Phase I/randomized phase II study of afatinib, an irreversible ErbB family blocker, with or without protracted temozolomide in adults with recurrent glioblastoma." Neuro-oncology 17.3 (2015): 430-439.

13. An, Zhenyi, et al. "Epidermal growth factor receptor and EGFRvIII in glioblastoma: signaling pathways and targeted therapies." Oncogene 37.12 (2018): 1561-1575.

14. Furnari, Frank B., et al. "Heterogeneity of epidermal growth factor receptor signalling networks in glioblastoma." Nature Reviews Cancer 15.5 (2015): 302-310.

15. Guo, Gao, et al. "Ligand-independent EGFR signaling." Cancer research 75.17 (2015): 3436-3441.

16. Barkovich, Krister J., et al. "Kinetics of inhibitor cycling underlie therapeutic disparities between EGFR-driven lung and brain cancers." Cancer discovery 2.5 (2012): 450-457.

17. Gabathuler, Reinhard. "Approaches to transport therapeutic drugs across the blood–brain barrier to treat brain diseases." Neurobiology of disease 37.1 (2010): 48-57.

18. Pardridge, William M. "The blood-brain barrier: bottleneck in brain drug development." NeuroRx 2.1 (2005): 3-14.

19. Heffron, T. P. Small molecule kinase inhibitors for the treatment of brain cancer. *J. Med. Chem.* **2016,** *59*, 10030–10066.

20. Ghose, A. K.; Herbertz, T.; Hudkins, R. L.; Dorsey, B. D.; Mallamo, J. P. Knowledge-based, central nervous system (CNS) lead selection and lead optimization for CNS drug discovery. *ACS Chem. Neurosci.* **2012,** *3*, 50–68.

21. Wager, T. T.; Chandrasekaran, R. Y.; Hou, X.; Troutman, M. D.; Verhoest, P. R.; Villalobos, A.; Will, Y. Defining desirable central nervous system drug space through the alignment of molecular properties, in vitro ADME, and safety attributes. *ACS Chem. Neurosci.* **2010,** *1*, 420–434.

22. Bohn, Jan-Paul, et al. "Targeted therapies for the treatment of brain metastases in solid tumors." Targeted oncology 11.3 (2016): 263-275.

23. Lassman, Andrew B., et al. "Molecular study of malignant gliomas treated with epidermal growth factor receptor inhibitors: tissue analysis from North American Brain Tumor Consortium Trials 01-03 and 00-01." Clinical Cancer Research 11.21 (2005): 7841-7850.

24. Zeng, Qingbei, et al. "Discovery and evaluation of clinical candidate AZD3759, a potent, oral active, central nervous system-penetrant, epidermal growth factor receptor tyrosine kinase inhibitor." Journal of medicinal chemistry 58.20 (2015): 8200-8215.

25. Ballard, Peter, et al. "Preclinical comparison of osimertinib with other EGFR-TKIs in EGFR-mutant NSCLC brain metastases models, and early evidence of clinical brain metastases activity." Clinical Cancer Research 22.20 (2016): 5130-5140.

26. Tsang, Jonathan E., et al. "Development of a Potent Brain-Penetrant EGFR Tyrosine Kinase Inhibitor against Malignant Brain Tumors." ACS Medicinal Chemistry Letters 11.10 (2020): 1799-1809.

27. Bosc, Nicolas, Christophe Meyer, and Pascal Bonnet. "The use of novel selectivity metrics in kinase research." BMC bioinformatics 18.1 (2017): 1-12.

28. Liu, Xuejiao, et al. "The third-generation EGFR inhibitor AZD9291 overcomes primary resistance by continuously blocking ERK signaling in glioblastoma." Journal of Experimental & Clinical Cancer Research 38.1 (2019): 1-14.

29. Broniscer, Alberto, et al. "Plasma and cerebrospinal fluid pharmacokinetics of erlotinib and its active metabolite OSI-420." Clinical Cancer Research 13.5 (2007): 1511-1515.

30. Polli, Joseph W., et al. "An unexpected synergist role of P-glycoprotein and breast cancer resistance protein on the central nervous system penetration of the tyrosine kinase inhibitor lapatinib (N-{3-chloro-4-[(3-fluorobenzyl) oxy] phenyl}-6-[5-({[2-(methylsulfonyl) ethyl] amino} methyl)-2-furyl]-4-quinazolinamine; GW572016)." Drug Metabolism and Disposition 37.2 (2009): 439-442.

31. Liu, Xingrong, Cuiping Chen, and Bill J. Smith. "Progress in brain penetration evaluation in drug discovery and development." Journal of Pharmacology and Experimental Therapeutics 325.2 (2008): 349-356.

32. Kim, Minjee, et al. "Barriers to effective drug treatment for brain metastases: a multifactorial problem in the delivery of precision medicine." Pharmaceutical research 35.9 (2018): 1-20.

33. Raub, Thomas J. "P-glycoprotein recognition of substrates and circumvention through rational drug design." Molecular pharmaceutics 3.1 (2006): 3-25.

34. Mai, Wilson X., et al. "Cytoplasmic p53 couples oncogene-driven glucose metabolism to apoptosis and is a therapeutic target in glioblastoma." Nature medicine 23.11 (2017): 1342.

35. Tannous, Bakhos A. "Gaussia luciferase reporter assay for monitoring biological processes in culture and in vivo." Nature protocols 4.4 (2009): 582.

36. Gao, Hui, et al. "High-throughput screening using patient-derived tumor xenografts to predict clinical trial drug response." Nature medicine 21.11 (2015): 1318-1325.

37. Spilker, Mary E., et al. "Found in translation: maximizing the clinical relevance of nonclinical oncology studies." Clinical Cancer Research 23.4 (2017): 1080-1090.

38. Liston, Dane R., and Myrtle Davis. "Clinically relevant concentrations of anticancer drugs: a guide for nonclinical studies." Clinical Cancer Research 23.14 (2017): 3489-3498.

39. Ling, Jie, et al. "Metabolism and excretion of erlotinib, a small molecule inhibitor of epidermal growth factor receptor tyrosine kinase, in healthy male volunteers." Drug metabolism and disposition 34.3 (2006): 420-426.

40. Burris, Howard A., et al. "A phase I and pharmacokinetic study of oral lapatinib administered once or twice daily in patients with solid malignancies." Clinical Cancer Research 15.21 (2009): 6702-6708.

41. Soria, Jean-Charles, et al. "Osimertinib in untreated EGFR-mutated advanced non–small-cell lung cancer." New England journal of medicine 378.2 (2018): 113-125.

42. Makhlin, Igor, et al. "Clinical activity of the EGFR tyrosine kinase inhibitor osimertinib in EGFR-mutant glioblastoma." CNS oncology 8.3 (2019): CNS43.

43. Chagoya, Gustavo, et al. "Efficacy of osimertinib against EGFRvIII+ glioblastoma." Oncotarget 11.22 (2020): 2074.

44. Ghezzi, Chiara, et al. "A high-throughput screen identifies that CDK7 activates glucose consumption in lung cancer cells." Nature communications 10.1 (2019): 1-15.

45. Spence, Alexander M., et al. "18F-FDG PET of gliomas at delayed intervals: improved distinction between tumor and normal gray matter." Journal of Nuclear Medicine 45.10 (2004): 1653-1659.

46. Amin, Shahil, and Oliver F. Bathe. "Response biomarkers: re-envisioning the approach to tailoring drug therapy for cancer." BMC cancer 16.1 (2016): 1-11.

47. Garcia, Jacqueline S., et al. "Increased mitochondrial apoptotic priming with targeted therapy predicts clinical response to re-induction chemotherapy." American journal of hematology 95.3 (2020): 245-250.

48. Dai, HaiQing, et al. "Distribution of STI-571 to the brain is limited by P-glycoprotein-mediated efflux." Journal of Pharmacology and Experimental Therapeutics 304.3 (2003): 1085-1092.